VILNIUS UNIVERSITY
Nature research centre

Laurynas
Šiliauskas

Evolution of the proterozoic magmatic complexes in southern Lithuania: implications for the formation of the Varena iron ore deposit

DOCTORAL DISSERTATION

Natural sciences,
Geology N-005

VILNIUS 2019

This dissertation was written between 2015 and 2019 in Nature Research Centre. The research was supported by Nature research centre and Synthesys project.

Academic supervisor – dr. Gražina Skridlaitė, Nature Research Centre, Natural Sciences, Geology N005.

CONTENTS

INTRODUCTION 5
Aim and tasks of the thesis 5
Importance of the study 6
Major statements to be defended 6
Academic and practical application of the study 7
Material and personal input 8
1. HISTORY OF PRECAMBRIAN GEOLOGY RESEARCH IN LITHUANIA 10
2. GEOLOGICAL SETTING 12
2.1 The LEL 12
2.2. The MLD 13
2.3. The WLG 14
3. METHODS OF INVESTIGATION 17
4. SAMPLE DESCRIPTION 19
4.1. Rocks from the VIOD surroundings 19
4.2. The VIOD rocks and ores 22
4.3. Granitoids crosscutting the VIOD 30
5. RESULTS 32
5.1 Rock chemistry 32
5.1.1 Rocks surrounding the VIOD 32
5.1.2. The VIOD rocks 36
5.1.3. Granites crosscutting the VIOD rocks 37
5.2. P-T estimates 39
5.2.1. Rocks surrounding the VIOD 39
5.2.2. The VIOD rocks 42
5.2.3. The crosscutting granitoids 44
5.3. Magnetite microtextures and chemical compositions 44

5.4. Zircon and monazite dating results 46
5.4.1. The rocks surrounding the VIOD 46
5.4.2. The VIOD rocks and ores 51
5.4.3. The crosscutting granite veins 55
6. DISCUSSION 62
6.1. Origin of rocks surrounding the VIOD 62
6.2. Age and evolution of the rocks surrounding the VIOD 64
6.3. Evolution and timing of the VIOD rocks and ores 64
6.4. Age and emplacement conditions of the granite veins 68
6.5. Regional context 70
6.6. Implications for ore sources for the Varėna Iron Ore deposit 72
7. CONCLUSIONS 73
ACKNOWLEDGMENTS 74
REFERENCES 75
APPENDIX 87
1. Tables 87
PAPERS 97

INTRODUCTION

The Varena Iron Ore deposit (VIOD) is situated in the crystalline basement of south-eastern Lithuania. It was discovered during the 1982-1988 geological and geophysical investigations, when distinct magnetic anomalies were tested by drilling. The first estimates showed that the deposit hosted ca. 1.8 million tons of iron ore (Marfin et al., 1988), but after more detailed investigations in 1990-1992, the resources increased up to 71-219.6 million tons (Marfinas 1998; 1996). The ore hosting rocks are mostly dolomitic marbles, interlayered with various silicate rocks (meta greywackes, para/orthoamphibolites, metaigneous rocks etc) and crosscut by granitic veins. Based on these observations, as well as the typically low trace element and REE contents, a sedimentary origin of the marbles was proposed ([a,b]Skridlaite, 1993; Skridlaite and Motuza, 2001). However, the origin of the carbonate rocks, as well as of the ore itself, are subjects of debate up till now. Different origins have been proposed for the VIOD: a layered mafic complex (Kepežinskas, Šliaupa, 1994), an ultramafic intrusion (Motuza, Kirkliauskaite 2016), an alkaline carbonatitic intrusion (Kirkliauskaite et al., 2016), and skarns of metasomatic origin ([a,b]Skridlaite, 1993). The current research mainly supports the latter theory. First, rock complexes like those hosting the VIOD have a much wider regional distribution but have not yet been studied properly. These rocks often show signs of hydrothermal alteration such as sericitization, K-feldspatization or tourmaline-enrichment, that often precede skarn formation. For example, metarhyolitic and metaandesitic rocks are interlayered with calciphyres in the Lz/13 drillcore (II) farther west from the VIOD. These rocks may be a part of the same basin where the rocks hosting the VIOD were deposited; therefore, their study may provide new information on the VIOD surroundings. Numerous granitic veins crosscut the VIOD (IV) and the surrounding rocks. These igneous rocks of unknown origin crosscut the VIOD rocks, have sharp contacts and display alteration zones a few millimetres thick. They may post-date metasomatic events and ore formation.

Aim and tasks of the thesis

The aim of this thesis is to investigate the igneous and sedimentary complexes hosting the Varena Iron Ore deposit (VIOD) and to put time constraints on its formation and ore mineralization.

In order to achieve this aim, several tasks were undertaken:

1) To infer the origin and evolution of rocks hosting and surrounding the VIOD by means of zircon and monazite dating and P-T-t reconstructions: a case study of the surrounding Lazdijai 13 complex resembling some of the VIOD host rocks (II).

2) To estimate the type, evolution and timing of the magnetite mineralization in the VIOD through detail microtextural and chemical analysis, determination of P-T conditions and in-situ monazite dating (I and III).

3) To determine the age and origin of the granite veins crosscutting the VIOD rocks in order to elucidate the last stages of the iron mineralization (IV).

4) To correlate the results obtained with the evolution of the whole region and to imply a time framework for the ore mineralization.

Importance of the study

The Varėna Iron Ore deposit has been poorly studied, especially considering the tectonic plate paradigm and regional evolution. Previous studies were mainly descriptive, based on rock macro-and micro-investigations, semi-quantitative geochemistry and a few mineral spot analyses (cf. Skridlaite, 1993). No suitable isotopic investigations were carried out, hence no regional implications properly made. New, detailed Scanning Electron Microscopy (SEM), Electron Microprobe analysis (EPMA) of minerals and ores offered the possibility of obtaining information on the rock and ore origins and evolution. This study also provided new insights into the timing of regional metamorphism that manifests itself in the deposit and the surrounding area. The newly obtained isotopic zircon and chemical monazite dates provide implications for the timing of ore formation. The established link between the VIOD ore and AMCG complex formation enhances the economic potential of the region.

Major statements to be defended

1. The 1.83 Ga Lazdijai metavolcanic complex might be contemporaneous with some of metasedimentary-metavolcanic complexes hosting the Varena Iron Ore deposit; thus, they were all likely formed in back-arc settings along the earlier established ca. 1.89-1.84 Ga continental margin

2. The earliest, spinel inclusion-and exsolution-rich magnetite appeared during the regional metamorphism at ca. 1.79 Ga and the subsequent uplift.

Reheating at ca. 1.50 Ga caused ore recrystallization and the formation of late-stage magnetite with abundant serpentine inclusions and no spinel exsolutions.

3. The regional metamorphism, hydrothermal reworking and ore mineralization were post-dated by crosscutting, ca. 1.50 Ga, granitoid veinlets.

4. Major geological events obtained by the study from the VIOD and surrounding rocks correlate well with the regional events: they recorded a ca. 1.79 Ga metamorphism, a ca. 1.73 Ga uplift and hydrothermal reworking, and at 1.50-1. 47 Ga ore remobilizations during fluid influx and hydrothermal overprint.

Academic and practical application of the study

The data obtained allowed us to recognize back-arc basins at 1.83-1.81 Ga in south-central Lithuania. The rocks deposited there host the largest iron ore deposit in Lithuania, which is economically important. The links discovered between the Varėna Iron Ore deposit and the voluminous AMCG Mazury complex to the south, in northern Poland and southern Lithuania, enhances the economic potential of the studied deposit.

The results have been presented and discussed at more than 8 international conferences:

• Siliauskas, L., Skridlaite, G., 2015. C. 1.5 Ga metamorphism of the Lazdijai 13 volcano-sedimentary sequence in southern Lithuania: its origin and implications. Geophysical Research Abstracts Vol. 17, EGU2017, EGU General Assembly, April 12-17, 2018, Vienna, Austria.

• Siliauskas, L. and Skridlaite, G., 2016. The 1.83-1.80 Ga volcano sedimentary sequence in southern Lithuania: origin, evolution and correlation with south-central Sweden. Bulletin of The Geological Society of Finland, Special Volume, Abstracts of 32nd Nordic Geological Winter Meeting, 13th-15th Januray 2016, Helsinki, Finland, p. 168. ISSN 0367-5211. http://www.geologinenseura.fi/winter_meeting/abstracts_newnum_pdf/S5_3_46.pdf

• Skridlaite, G., Wiszniewska, J., Petecki, Z., Siliauskas, L. and Prusinskiene, S., 2016. Fe (Ti, Cu) mineralizations in NE Poland and S-SE Lithuania: their possible links and implications for regional evolution. Abstracts of 35th International Geological Congress, 27 August - 4 September 2016, Cape Town, South Africa.

• Šiliauskas, L., Skridlaitė, G., Prušinskienė, S. 2017. P-T evolution of the Precambrian mafic rocks hosting the Varėna Iron ore deposit in SE Lithuania. 19th EGU General Assembly, EGU2017, proceedings from the conference held 23-28 April 2017 in Vienna, Austria., p.9223

• Skridlaitė, G., Šiliauskas, L., Prušinskienė, S., 2017. Remnants of the Andean Type Continental Margin in the Lithuanian Precambrian: Implications from Geochemical and Isotopic Data. Proceedings at international conference "Be praeities nėra ateities" dedicated to 215th Birth anniversary of Ignacy Domeiko, Lithuanian Academy of Science.

• Siliauskas, L., Skridlaite, G., Whitehouse, M. and Soesoo, A., 2018. A ca.1.89 Ga magmatic complex in eastern Lithuania: a link connecting with the domains in Estonia and the Bergslagen terrane in Sweden. 33rd Nordic Geological Winter Meeting (NGWM), Copenhagen, Denmark, January 10-12, 59 p. https://2dgf.dk/foreningen/33rd-nordic-geological-winter-meeting/ngwm-2018-abstracts/1-igneous-rocks-and-processes/

• Šiliauskas, L., Skridlaitė, G., Whitehouse, M. and Soesoo, A., 2018. A ca.1.89 Ga magmatic complex in eastern Lithuania: a link connecting with the domains in Estonia and the Bergslagen terrane in Sweden. Geophysical Research Abstracts Vol. 20, EGU2018-3050, EGU General Assembly, 8-13 April 2018, Vienna, Austria.

• Šiliauskas, L., Skridlaitė, G., Whitehouse, M., Johansson, A., Bogdanova, S., 2019. Tracking the 1.86-1.84 Ga continental margin in the concealed basement of Lithuania, western East European Craton: implications from U-Pb, Sm-Nd and Rb-Sr isotopic investigations. Geophysical Research Abstract Vol. 21, EGU2019-947, EGU General Assembly, April 2019, Viena, Austria.

• Skridlaite, G., Siliauskas, L., Rimsa, A., Whitehouse, M., Johansson, A. and Bogdanova, S. 2018. 1.86-1.79 Ga magmatic events in the western East European Craton: from subduction to back-arc settings. 33rd Nordic Geological Winter Meeting (NGWM), Copenhagen, Denmark, January 10-12, 55 p. https://2dgf.dk/foreningen/33rd-nordic-geological-winter-meeting/ngwm-2018-abstracts/1-igneous-rocks-and-processes/

Material and personal input

The study was conducted using modern approaches and considering the most up-to-date scientific results obtained in Lithuania and neighbouring

countries. Samples were taken from the Vievis drillcore storage. More than 20 drillcore sections were thoroughly examined, more than 60 samples collected for polished thin sections, 30 for whole rock chemical analysis and 12 for U-Pb SIMS analysis. The author himself conducted SEM and partly EPMA analyses, examined thin sections, analysed zircons by the SIMS approach, co-authored articles based on the data obtained. The study was partly supported by the Nature Research Centre study funds. The author was granted SYNTHESYS 3 project support (project SE-TAF-7040).

The thesis comprises an Introduction, History of Precambrian geology research in Lithuania, Geological setting, Methods of investigation, Sample description, Results, Discussion and Conclusions). Some of the data are presented in the appendix (Tables A1-10). The thesis is 100 page long, supplemented with 21 figure and contains 8 tables.

1. HISTORY OF PRECAMBRIAN GEOLOGY RESEARCH IN LITHUANIA

The first few deep wells in Lithuania were drilled in 1947-1952 (Gailius et al., 1994). In 1958-1978 geological mapping of the Republic was conducted (Gailius et al., 1994). During this period deep wells (up to 2330 m) were used to map the Phanerozoic rocks in Lithuania. Most of the drillings reached the crystalline basement. No dating was available at that time, so correlations between the wells were made based on the chemical composition, general appearance and metamorphic grade. Metamorphic grade was mostly implied based on the appearance of indicative minerals, such as garnet, and assemblages they are in. An example of that was Balninikai complex, composed of fine grained basic volcanic rocks (Vasiliejavas et al., 1976; Stripeika, 1987) and occupying most of central and eastern Lithuania. Geological maps of the crystalline basement based on rock descriptions and chemical composition were made (Motuza et al., 1986;) as well as first P-T estimations (Клейн и др., 1990).

Magnetic field anomalies in Lithuania were first discovered quite early in 1936-1938, but it was not until a geological mapping project in 1973-1976 that some of the anomalies were tested near the township of Varėna (Gailius et al., 1994). The first drillings of the Varėna Iron ore deposit showed that most of the ore is hosted in serpentinites, where magnetite comprises 20-78 % by volume (Motuza et al., 1976). Geological mapping and investigations estimated that 1.8 million tons of iron were present (Marfin et al., 1988). After more detailed examinations, estimates increased to 71-219.6 million tons (Marfinas 1998; 1996). In the early stages of well drilling it was noted that some parts of the ore host substantial amounts of sulphides: pyrite and chalcopyrite. Chalcopyrite and molybdenite mineralization were discovered in the Marcinkonys granites (southern Lithuania) too (Motuza and Skripkina, 1981; Gailius, 1985). Later researchers proposed different models for the genesis of the Varėna Iron Ore deposit: a layered mafic complex (Kepežinskas, Šliaupa, 1994); an ultramafic intrusion (Motuza, Kirkliauskaite 2016), an alkaline carbonatitic intrusion (Kirkliauskaite et al., 2016), and a metasomatic origin ([a,b]Skridlaite, 1993).

In Soviet times, until Lithuania regained its independence, an Archean age of the crystalline basement was implied (Gailius et al., 1994). The first up-to-date isotopic age measurements were obtained from the Marcinkonys granite

in southern Lithuania (Sundblad et al., 1994), where a Mesoproterozoic age was obtained instead of the anticipated Archean.

2. GEOLOGICAL SETTING

The Earth's crust in Lithuania is part of the East European Craton (EEC) and is buried beneath 200-2000 m thick sediments. Based on magnetic and gravity surveys, EUROBRIDGE seismic profiling results and new age data, several major tectonic units were revealed in the crystalline crust of Lithuania: West Lithuanian Granulite domain (WLG), East Lithuanian (EL) Belt, Mid-Lithuanian Suture Zone (MLSZ) and Belarus-Podlasie Granulite (BPG) Belt (Skridlaite, Motuza, 2001; Bogdanova et al., 2006 and references therein). The WLG was considered to be juxtaposed with the EL by the MLSZ which was distinguished from the WLG by uplift of the Moho, a thinner lower crust (WLG 10-12 km, MLSZ 10-5 km) and the whole crust in general (WLG 45-50 km, MLSZ 40 km) (Bogdanova et al., 2006 and references therein). The WLG was correlated with domains in Poland and comprised the Polish-Lithuanian terrane; the MLSZ was considered to continue into Latvia, while the EL belonged to the Lithuanian-Belarus terrane (Bogdanova et al., 2006).

A new, revised model was proposed by Bogdanova et al. (2015) based on the numerous isotopic studies, P-T-t reconstructions and newly revised geophysical maps (Fig. 1). New structural units were introduced, and older boundaries were corrected. The newly outlined WLG together with northern domains in Poland comprise the 1.83-1.76 Ga Amberland, the newly distinguished 1.86-1.84 Ga Mid-Lithuanian domain (MLD) comprising southern part of the former MLSZ and N, NW parts of the former WLG belongs to the Mid-Baltic belt. The former East Lithuanian (EL) domain was merged with similar units in Latvia into LEL (Latvian-East Lithuanian domain) which, in turn, adjoined the larger Bergslagen/Livonia terrane (Fig. 1). The easternmost Belarus-Podlasie Granulite (BPG) belt is no longer considered to be part of Fennoscandia but rather belongs to Sarmatia (Bogdanova et al., 2015).

2.1 The LEL

The LEL in Latvia is dominated by mafic, intermediate and felsic metavolcanics, metamorphosed Fe-Mg-rich quartzites and other metasediments (Bogdanova et al., 2015). The T_{DM} in range of 2.3-1.88 Ga and εNd of +3-4 at 1.90 Ga point to a predominantly mantle source for the volcanics (Mansfeld, 2001). The Staicele1 metavolcanic rock from northern Latvia yielded an age of 1870±13 Ma (Mansfeld, 2001) and experienced

granulite facies metamorphism at 1810±2 Ma (Mansfeld, 2001). In southern Lithuania, the LEL is dominated by felsic and mafic metavolcanics and sedimentary rocks, particularly metagreywackes and marbles with minor intrusives (Skridlaite and Motuza, 2001; Motuza, 2005). Mg- and Fe-rich skarns are associated mostly with dolomite-rich marbles (Skridlaite and Motuza, 2001). While the metagreywackes in the southern LEL contain some Archaean detrital zircon, Palaeoproterozoic zircon is dominant and Sm–Nd isotopic modelling indicates Palaeoproterozoic ages of deposition (Mansfeld, 2001). A segment of the LEL metadiorite (Lz8 drilling) uplifted by the ca. 1.50 Ga AMCG rocks farther west and dated at 1887±9 Ma (Bogdanova et al, 2015) was the only dated LEL rock in Lithuania so far. However, during a recent study (Šiliauskas et al., 2018) several similar ages were obtained from the metaigneous VIOD: 1892±6 Ma (D8) and 1894±7 Ma (D9), and the surrounding rocks:1876±5 Ma (Lz27) and 1898±8 Ma (Lz13). Charnockite of similar age have been reported in northern Poland, dated to 1881±16 Ma (Krzeminska et al., 2019), suggesting LEL extension further south. Metasediments in the southern LEL were metamorphosed in the upper amphibolite facies conditions (700˚ C; 6 kbar; Bogdanova et al., 2006). Amphibole $^{40}Ar/^{39}Ar$ dating of various rocks in LEL showed two main cooling events at 1.66 Ga (Bogdanova et al., 2001) and 1.55-1.45 Ga (Bogdanova et al., 2001; Skridlaite et al., 2006). The first followed shearing and metamorphism caused by the final amalgamation of Fennoscandia and Sarmatia, whereas the second is related to the ca. 1.50 Ga Anorthosite-Mangerite-Charnockite-Granite (AMCG) emplacement (Bogdanova et al., 2001). This domain hosts several iron ore deposits, recognised by magnetic field anomalies and drillings, the Varena Iron Ore Deposit (VIOD) being the largest among them.

2.2. The MLD

The MLD is an eastwards-convex belt, composed mainly of intrusive rocks and their volcanic counterparts (Bogdanova et al., 2015). These rocks were emplaced between 1.86 and 1.84 Ga (Bogdanova et al., 2015; Motuza, 2005; Motuza et al., 2008; Rimsa et al., 2001; Skridlaite et al., 2011, 2012, 2014, Vejelyte, 2011). Granitic rocks comprise the northern and western part of MLD, whereas a granite, granodiorite, diorite and gabbro suite with a TTG signature dominates in the south (Rimsa et al., 2001). Granite gneisses from northern Poland (Lanowicze PIG-1) have been dated to ca. 1.84-1.85 Ga and

reworked at ca. 1.79 Ga and 1.51 Ga (Krzeminska et al., 2019). The Frigsarve granites on the Gotland Island in Sweden which are interpreted to be a part of the Transscandinavian Igneous Belt-0 (TIB-O, 1855-1845 Ma) were dated at 1845 Ma (Salin et al., 2019), possibly confirming the continuation of the MLD into south-central Sweden. Sm-Nd isotopic compositions indicate crustal rock assimilation in the west (Vidmantai1 T_{DM} 2.4 Ga, εNd-2.4 at 1.9 Ga; Mansfeld 1995) and juvenile sources in the south (Lz13 T_{DM} 2.08 Ga, εNd+1.8 at 1.9 Ga; Claesson et al., 2001). A granulite facies metamorphic overprint has been dated in the western MLD at 1809±9 Ma (Skridlaite et al., 2014) in Gl99 mafic granulite and 1822±8 Ma and a 1727±30 Ma reworking in 7Gr S-type granite (Bogdanova et al., 2015; Skridlaite et al., 2014).

2.3. The WLG

The WLD domain is composed mainly of sedimentary and felsic to intermediate metaigneous rocks and is intruded by granitic and charnockitic rocks. A granite from drilling Rusne-1 was dated at 1810 Ma (Claesson, 1996), while the Siupariai 3 charnockite intruded at ca. 1.83-1.82 Ga (Skridlaite et al., 2014 and references therein). Similar ages of 1.83-1.80 Ga were obtained from the igneous rocks of basic to felsic composition with island arc affinity in the Mazowsze domain, Poland (Krzeminska et al., 2005, 2007; Wiszniewska et al., 2007). Zircon detritus from the WLG metasediments contain zircons populations of 2.02, 1.98, 1.94 and 1.90-1.87 Ga (Bogdanowa et al., 2015; Krzeminska et al., 2009), a deposition age being later than 1.87 Ga. The Sm-Nd isotopic data indicate a presence of major crustal components (T_{DM} 2.37-2.31 Ga, εNd-3.1 -2.31 at 1.9 Ga; Mansfeld, 2001). Four metamorphic events have been recorded in the western WLG at 1.81-1.79, 1.73-1.68, 1.62-1.58 and 1.52-1.50 Ga, reaching up to 900 ˚C and 10 kbar (Skridlaite et al., 2014). The rocks were intruded by the ca. 1.47-1.45 Ga AMCG rocks (Motuza et al., 2006; Skridlaite et al., 2007). The Mazury AMCG complex was emplaced along the E-W trending shear zones in northern Poland and southern Lithuania in a time span of 1.56-1.48 Ga (Morgan et al., 2000; Dörr et al., 2002; Ruszkowski et al., 2018; Skridlaitė et al., 2003; Skridlaitė et al., 2008; Sundblad et al., 1994). The ca. 1.50 Ga Kabeliai granites (Sundblad et al., 1994) farther east are the continuation of this complex, as well as several granite bodies in neighbouring Belarus. Their emplacement caused deformation and metamorphism of the country rocks (Bogdanova et al., 2001; Skridlaite et al., 2006, 2008, 2014), recorded by

zircon, monazite and hornblende $^{40}Ar/^{39}Ar$ dates. Their emplacement is related to intracratonic extension and accretionary events further west (Bogdanova et al., 2008; Brander and Söderlund, 2007; Brander et al., 2012).

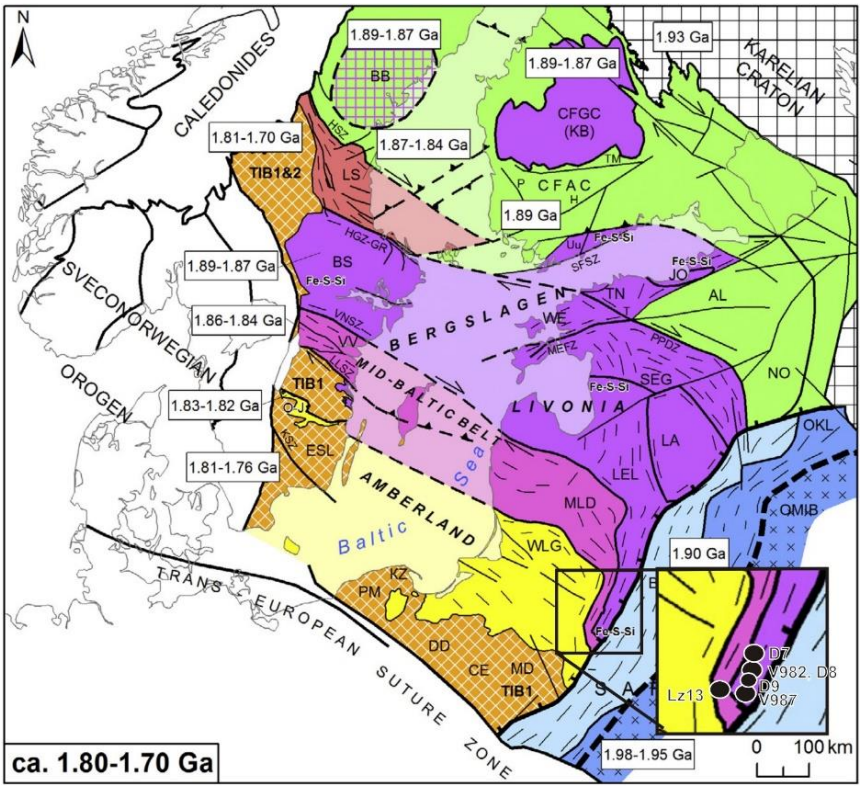

Fig. 1. Tectonic units in the central and southern parts of the Svecofennian orogen as extrapolated across the Baltic Sea (Bogdanova et al., 2015). Principal ages of accretionary events are presented in the boxes. The abbreviations for tectonic domains are: AL – Alutaguse; BB – Bothnian (Bothnian microcontinent); BS – Bergslagen (Bergslagen microcontinent); BPG – Belarus-Podlasie granulite belt; CE – Ciechanow; CFAS – Central Finland Arc Complex; CFGC – Central Finland Granitoid Complex (Keitele microcontinent); DO – Dobrzyn; ESL – East Småland; JO – Jõhvi; KB – Keitele microcontinent; KZ – Kaszuby; LA – Latgalia; LEL – Latvian-East Lithuanian; LGB – Lapland Granulite Belt; LKO – Lapland-Kola orogen; LS – Ljusdal; MD – Mazowsze; MLD – Mid-Lithuanian domain; NB – Norrbotten; NO – Novgorod; OKL – Okolovo; OMIB – Osnitsk-Mikashevichi Igneous Belt; PM – Pomorze; SEG – South Estonian granulite

domain; T – Tapa; TIB – Transscandinavian Igneous Belt; TN – Tallinn; Uu – Uusimaa; VV – Västervik; WE – West Estonian domain; WLG – West Lithuanian granulite domain. The abbreviations for deformation zones are: HGZ-GR – Hagsta-Gävle-Rättvik Zone; HSZ – Hassela shear zone; KSZ – Karlskrona Shear Zone; LLSZ – Linköping-Loftahammar Shear Zone; MEFZ – Middle Estonian Fault Zone; PPDZ – Paldiski-Pskov Deformation Zone; SFSZ – South Finland Shear Zone; VNSZ – Vingäker-Nyköping Shear Zone. Abbreviations for volcanic belts and sedimentary basins: H – Häme; O-J – Oskarshamn-Jönköping; P – Pirkanmaa; TM – Tampere. The investigated area is presented in an enlargement and drillings investigated in the study are marked by black dots.

3. METHODS OF INVESTIGATION

More than fifty polished thin sections were prepared from representative samples of the VIOD rocks and ores, and from the surrounding rocks (Lz13 drillcore) and crosscutting granites (Fig. 1). They were studied using a polarizing optic microscope Nicon 50iPol and Scanning Electron Microscope (SEM) Quanta 250 at the Nature Research Centre, Vilnius, Lithuania. Detailed descriptions of rock compositions and textures are presented in papers I, II, III and IV. Mineral analyses were carried out using the SEM with the X-Max (20 mm^2) silicon drift (SDD) energy dispersive spectrometer (EDS). Beam current of 1.1-1.2 nA and accelerating voltage of 10-20 kV were used.

Major and trace element abundances in the D9-1083 and V987-387 granitoids and sample D9-473 were measured by ICP-ES and ICP-MS techniques at the ACME laboratory in Canada. Samples from the Lz13 drill core were analysed at Luleå Technical University in Sweden. Sample powder of 0.125 g was melted with 0.375 g of $LiBO_2$ and dissolved in HNO_3 acid. Major and some of the trace elements were measured by Inductively Coupled Plasma Atomic Emission Spectroscopy. Concentration of the remaining trace elements and rare earths were determined using Inductively Coupled Plasma Mass-Spectroscopy. Major element concentrations in three additional samples from Lz13 drill core were determined by wet chemical analysis at the Geological Survey of Lithuania.

P-T estimations were carried out for Lz13 gedrite-bearing and gedrite-free metavolcanics. The plagioclase-biotite-garnet geothermobarometer (Holdaway, 2000) and garnet-chlorite thermometer (Grambling, 1990) were used to estimate temperature and pressure conditions in sample Lz13/521.8. Since gedrite and anthophyllite coexist in sample Lz13/512, the gedrite-anthophyllite solvus thermometer of Spear (1980) was used. Spear suggested that the solvus is defined by edenite and tschermakite substitutions, that can be expressed in Fe/(Fe+Mg) ratios with the crest of the solvus at 600±25 °C. The CNKFMASH system was used in constructing pseudosections, using TheriakDomino software (de Capitani and Brown 1987; de Capitani and Petrakakis 2010) and the Thermocalc database (Powell et al., 1998) with the Nowember 2004 (ds55) update of Holland and Powell's (1998) internally consistent data base. The applied a-x models and mineral phases are as follows: feldspar (Holland & Powell 2003), garnet, biotite, orthopyroxene and silicate melt (White et al. 2007), chlorite (Holland et al. 1998), amphibole,

staurolite and cordierite (Holland & Powell 1998). Quartz, H_2O and Al_2O_5 polymorphs were treated as pure phases.

Calcite-dolomite thermometry (Anovitz and Essene, 1987) with a correction for Fe content and monazite dating were carried out for the skarn 982-4 (418.7 m). Zircon saturation temperatures (T_{Zr}, Watson and Harrison, 1983) were calculated for the dated granitoid rocks (D9-1083 and V987-387). Unpublished results are presented in the RESULTS chapter.

Monazite (Lz13/540, 982-4 samples) and magnetite spot analysis (D8-1,2,7, 982-9,10 samples) was carried out using the EPMA Cameca SX100 at the Warsaw University, Faculty of Geology, Poland. Natural and synthetic materials were used as standards. The monazite analyses were carried out at an accelerating voltage of 20 kV and a beam current of 60 nA. Element contents were quantified at the following lines: Kα lines of P, La, Ca, S, Si; Lα lines of Ce, Er, Yb and Y; Lβ lines of Pr, Nd, Sm, Gd, Tb, Dy and Ho; Mβ lines of Pb and U; Mα line of Th. Data reduction as proposed by Montel et al. (1996) was carried out. The weighted averages were calculated using Isoplot 3.75 software (Ludwig, 2012) and are presented in Fig. 15 and tables 6 and 7. Magnetite grains were analysed using 15 nA current and accelerating voltage of 20 kV. The following lines were used for element quantification: Kα lines for Na, Mg, Al, Si, Fe, Mn, Cr, Ti, V, Ca, Ni, Cu, Zn, P, K and Lα line for Nb. The results are presented in Tables A7-10.

Hand-picked zircon samples from the D9-1083 and V987-387 granitoids were prepared at the Nature Research Centre, Vilnius. They and Lz13/521.8 sample were dated by the NORDSIM facility at Swedish Museum of Natural History in Stockholm, using the CAMECA imsl280 high resolution secondary ion mass spectrometer (ISMS). The analytical procedure was described by Whitehouse et al. (1999) and Whitehouse and Kamber (2005). A 1065 Ma reference zircon (Geostandards 91500; Wiedenbeck et al., 1995) was used for U/Pb ratio calibration. The reference zircon was calibrated repeatedly during the session. A software, developed at NORDSIM facility, was used for data reduction. The likely presence of common lead, as indicated by ^{204}Pb content (thrice as high as the average background on the ion counting electron multiplier), was corrected using the common lead present-day composition proposed by Stacey and Kramers (1975), assuming surface contamination during the polishing procedure. Further data reduction and age determinations were made using Isoplot 3.75 software developed by Ludwig (2012). The results are presented in Fig. 14 and 18 (at 95% confidence level) and in Tables 5 and 8.

4. SAMPLE DESCRIPTION

4.1. Rocks from the VIOD surroundings

The studied volcanic rocks from the Lz13 drillcore (485.5-540.8 m interval) overlies the older, ca 1.89 metavolcanic rocks (Šiliauskas et al., 2018). They were metamorphosed into fine grained, strongly foliated rocks, composed of quartz, biotite, garnet, orthorhombic amphiboles, K-feldspar, plagioclase, minor cordierite and chlorite in some parts and of quartz, biotite, garnet, cordierite, staurolite, plagioclase, K-feldspar and chlorite elsewhere. Thus, assemblages with orthorhombic amphibole (Lz13/512 and Lz13/521.8) and without it (Lz13/509.6 and Lz13/540) can be distinguished.

Orthorhombic amphibole bearing schists (Lz13/512 and Lz13/521.8) contain gedrite replacing large elongated anthophyllite grains often surrounded by plagioclase (Fig. 2a). Amphibole compositions were recalculated on a 23 oxygen atom basis and presented in Table A3 (II). In Lz13/521.8 sample gedrite is very abundant. Its Mg# varies from 0.37 to 0.43 and is highest in the cores and small grains enclosed in quartz. The Al^{VI} is almost constant: 1.10-1.40 apfu (II). A few grains of anthophyllite enclosed in quartz were found. They have higher Mg# (0.50-0.52) and lower Al^{VI} (0.25-0.35). In sample Lz13/512 Mg-rich anthophyllite (Mg# 0.53-0.55) is being replaced by gedrite (II). Gedrite has a strict chemical composition: Mg# 0.42-0.44 and Al^{VI} 0.77-0.90 (II). In domains where anthophyllite is completely replaced, gedrite is slightly richer in Fe (Mg# 0.39-0.44), and cordierite (Mg# 0.65-0.67) is present there (Fig. 2b; table A3; II). According to the classification of Leake et al. (1997), the orthorhombic amphiboles are ferrogedrites and Mg-rich anthophyllites. Garnet porphyroblasts in some places indicate rotation during growth (Fig. 2c). Garnet compositions, formula units (calculated for 12 oxygen units) and endmembers are presented in Table A1. The largest garnet (2-3 mm in diameter) cores have higher Ca content (grossular 6.9- 9.6) and are surrounded by small chlorites (Fig. 2c). The rims are Ca-poor (grossular content 5.0-6.1) and often host small inclusions of ilmenite. Garnet rich in pyrope (Mg# 0.19-0.18, whereas in larger porphyroblasts M# is 0.14-0.15) with grossular content similar to the garnet rims forms lenses with biotite and chlorite (Fig. 2d; II). Biotite is found as clots of small grains surrounded by quartz in the matrix, as inclusions in cordierite and as porphyroblasts (Fig. 2d and e). Their chemical composition has been recalculated for 22 oxygen atoms and presented in Table A2. Sample

Lz13/521.8 matrix biotite has higher Ti content (0.15-0.20 apfu) and lower Al^{VI} (0.32-0.47) than the porhpyroblasts (0.07-0.09 apfu Ti; Al^{VI} 0.66-0.75; II). The Fe/(Fe+Mg) ratio is similar in both groups: 0.49-0.53 and 0.49-0.51, respectively. Sample Lz13/512 biotite composition is similar to that of LZ13/521.8 porphyroblasts. Ti here is in a range of 0.09 to 0.14 apfu, Al^{VI} is 0.60-0.84 and the Fe/(Fe+Mg) ratio is 0.45-0.49 (II). The rock contains minute amounts of plagioclase. Plagioclase formulas were recalculated on an 8 oxygen atoms basis and presented in Table A4. Small 50-10 μm inclusions of plagioclase (An_{22-49}) were found in quartz next to biotite-gedrite intergrowths (II). Larger plagioclase grains (An_{77-87}) surround gedrite (Sample Lz13/512). Chlorite forms porphyroblasts (Fe/(Fe+Mg) ratio of 0.44-0.46) in lenses with biotite and replaces Fe-Mg silicates (chlorite Fe/(Fe+Mg) ratio 0.46-0.52; II).

Orthorhombic amphibole-free rocks (Lz13/509.6 and Lz13/540) are spotted, finely foliated schists. The spots are composed of garnet, magnetite, staurolite and locally present large biotite porphyroblasts. The finely foliated matrix is composed of quartz, K-feldspar, staurolite, cordierite and well - aligned biotite and chlorite (Fe/(Fe+Mg) ratio 0.49-0.59; II). Garnet and cordierite (Mg# 0.56-0.58) display skeletal growth (Fig. 2f; II). Garnets are homogeneous and have low grossular contents (3.7-2.8) and Mg# of 0.13-0.11. Biotite in the matrix is slightly richer in Ti (0.22-0.20 apfu) than biotite porphyroblasts (0.17-0.19 apfu; II). The matrix biotite tends to be slightly more Mg-rich, but generally, Fe/(Fe+Mg) ratio in orthorhombic amphibole-free samples is in a range of 0.59-0.62 (II). Large staurolite grains are found in intergrowths with garnet magnetite and quartz (Fig. 2f). In the matrix it is smaller and found together with Mg-rich cordierite (Mg# up to 0.62; Fig. 2g; table A5; II). Staurolite found as inclusions or intergrowths with garnet are richer in Mg (Mg# 0.15-0.16 within garnet and Mg# 0.17-0.20 at the garnet rim; table A6), compared to staurolite found elsewhere (Mg# 0.13-0.17; II). Plagioclase (An_{30-33}) is found only as small inclusions in quartz, next to cordierit

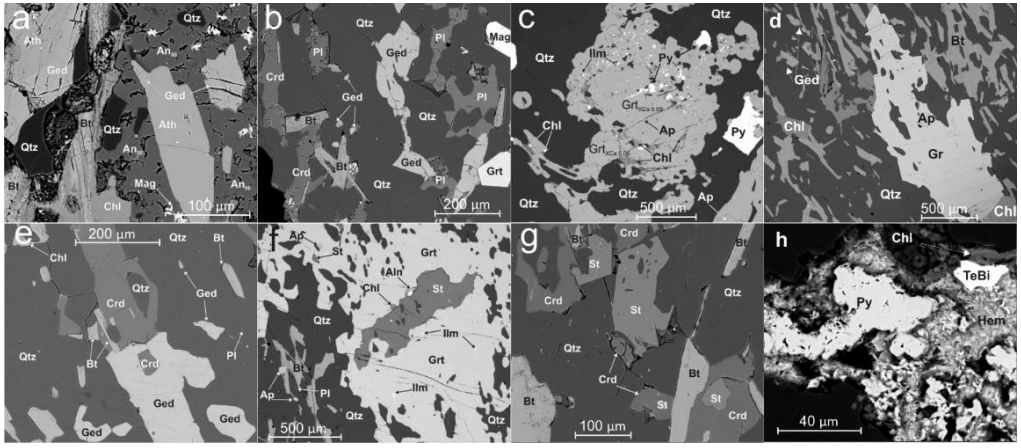

Fig. 2. BSE images of the Lz13 rocks. a. Gedrite and-anthophyllite in sample Lz13/512 are often surrounded by Ca-rich plagioclase. b. In sample Lz13/521.8 cordierite and garnet together can be found only in domains with no orthorhombic amphibole. c. Ca-rich garnet cores (sample Lz13/521.8), surrounded by ilmenite, pyrite and quartz inclusion trails. The rim has abundant chlorite inclusions. d. Simultaneous garnet and chlorite growth in sample Lz13/521.8. e. Gedrite formation at the expense of cordierite. Small plagioclase inclusions are found in quartz next to the orthorhombic amphibole. Cordierite engulfed biotite grains, preserving their primary orientation. f. Skeletal garnet growth in sample Lz13/540, at the expense of staurolite. Garnet hosts inclusions of staurolite, ilmenite, chlorite, quartz and allanite. g. In the lower right, partly consumed staurolite trapped in cordierite (sample Lz13/540). New staurolite, in equilibrium with cordierite growth in matrix. h. Fragment of deformed and partly oxidised pyrite veinlets hosting tellurobismuthite (sample Lz13/512). Mineral abbreviations are as follows: Aln: allanite; An: anorthite; Ap: apatite; Ath: anthophyllite; Bt: biotite; Chl: chlorite; Crd: cordierite; Ged: gedrite; Grt: garnet; Hem: hematite; Ilm: ilmenite; Mag: magnetite; Pl: plagioclase; Py: pyrite; Qtz: quartz; St: staurolite; TeBi: tellurobismuthite.

Accessory minerals in Lz13 rocks are ilmenite, pyrite, chalcopyrite, zircon, apatite, xenotime and allanite. Monazite was found only in sample Lz13/540. Pyritic veinlets in sample Lz13/512 often host small grains of tellurobismuthite (Fig. 2h). Some intervals are rich in Fe-Cu sulphides and magnetite (up to 10% in sample Lz13/509.6).

4.2. The VIOD rocks and ores

Detailed descriptions of the rocks from 982, D7, D8 and D9 drillcores can be found in papers I, III and IV. Only some rocks studied in more detail are described below. The 982-4 (418.7 m) skarn used for a calcite-dolomite thermometry (Anovitz and Essene, 1987) and monazite dating consists mainly of calcite, replaced by dolomite along the edges. The carbonates host large rounded grains replaced by asbestiform serpentine, formed after olivine. Small calcite grains can also be found in those rounded serpentine grains. Fractures in the carbonate matrix are filled by lizardite with variable iron content (FeO 5-14 wt%) and chrysotile of constant composition (FeO 2-3.3 wt%; III). Matrix calcite has lower X_{Mg} content (0.10-0.04) than calcite found in olivine pseudomorphs (X_{Mg} 0.15-0.08; III). Fractures in the carbonates are often filled with serpentine. Minute magnetite grains can be seen in the serpentine and porous calcite and dolomite. Scarce monazite grains of varying size occur at triple junctions with carbonates. The largest grains are rounded and often have dark cores and lighter rims in back-scattered electron (BSE) images, whereas the smaller grains are irregularly shaped and homogeneous.

Sample D9-473 is a fine-grained biotite, K-feldspar, plagioclase and quartz gneiss with minor muscovite. K-feldspar forms larger aggregates supported by matrix. It is comprised mainly of biotite, plagioclase and quartz. Minor muscovite can be seen in some places. Accessory minerals are zircon, monazite, xenotime, apatite and rutile (or anatase). A zircon separate of this sample was prepared for dating.

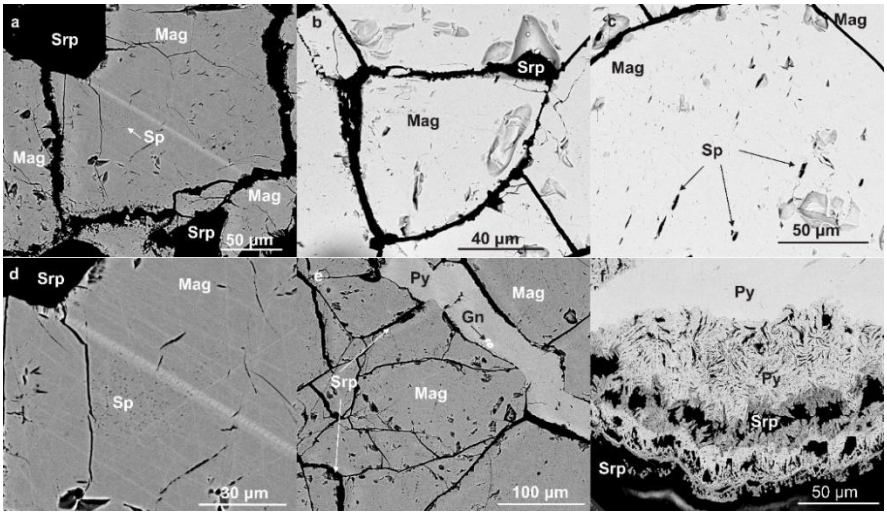

Fig. 3. BSE images of ores from sample D8-1. a. Magnetite grains closely follow boundaries of serpentine, replacing olivine. Magnetite boundaries often display dissolution along the rims. b. Magnetite grains in largest clusters attained textural equilibrium and meet at triple junctions. c. Most grains have trails of Mg-spinel exsolutions. d. Close-up of the magnetite grain showing that the core has very fine spinel exsolutions and exsolution-free rim. e. Magnetite in sample D8-1 crosscut by pyrite veinlet. f. Continuation of the same veinlet in serpentine rock show dendrite-like pattern of growth in pyrite. At the reaction front, pyrite is partly oxidized. Abbreviations are as in the previous figure. Others are: Gn: galena; Sp: spinel; Srp: serpentine.

Magnetite grains from samples D8-1 (488 m), D8-2 (491 m), D8-7 (714 m), 982-9 (604 m) and 982-10 (740 m) were analysed in more detail. Samples D8-1 is a serpentinite that hosts rounded olivine aggregates. Olivine is preserved only in places. Most of it is replaced either by antigorite or by iddingsite. A lizardite meshwork surrounds antigorite grains. Some chrysotile veinlets were also observed. The chemical composition of serpentines is variable. Phlogopite flakes are either scattered throughout the sample as single grains or form somewhat-aligned clusters in a serpentine matrix. They are partly replaced by magnesium-rich chlorite. Where phlogopite is being replaced, clusters of magnetite surround them. The ore forms larger aggregates in some places, but the majority is scattered throughout the rock. Magnetite mostly follows serpentine replacing olivine boundaries (Fig. 3a). Small

magnetite flakes are very common in the serpentine mesh. The grains in the largest magnetite clusters meet at triple junctions (Fig. 3b). These magnetites often host orderly rows of magnesium spinel exsolutions (Fig. 3 c and d). Carbonate veinlets with sulphides crosscut the rocks (Fig. 3e). Pyrite often forms dendrites in serpentine (Fig. 3f).

D8-2 is a serpentinite that hosts large clusters of magnetite aggregates. Oval-shaped olivine grains have been entirely replaced by serpentine and iddingsite. In some places iddingsite forms saw-tooth structures. Phlogopite flakes are scattered throughout the thin section. Larger magnetite grains follow olivine pseudomorph and phlogopite boundaries and are distributed perpendicular to the serpentine meshwork (Fig. 4a). They often host inclusions of phlogopite (Fig. 4b). Upon closer inspection, large magnetite grains have distinct cores and rims (Fig. 4c). The cores have small magnesium spinel exsolutions, distributed in rows. At the core-rim boundary, a thin row of inclusions resembling stylolite can be seen. The rim itself has no spinel exsolutions and has only inclusions of serpentine and chlorite. Grains meet at triple junctions (Fig. 4d). A few hematite grains have been found in calcite veinlets. Phlogopite is partly, or completely, replaced by Mg-rich chlorite. Small magnetite grains are distributed along the mica cleavage and sometimes join into larger grains, forming the rim described above (Fig. 4e). Carbonate and pyrite-filled veinlets, rimmed by serpentine, crosscut the sample. In some places the veinlets are fragmented by phlogopite, forming boudinage (Fig. 4f). A meshwork of late-stage serpentine (lizardite) fills the interstitial spaces and brecciates magnetite grains.

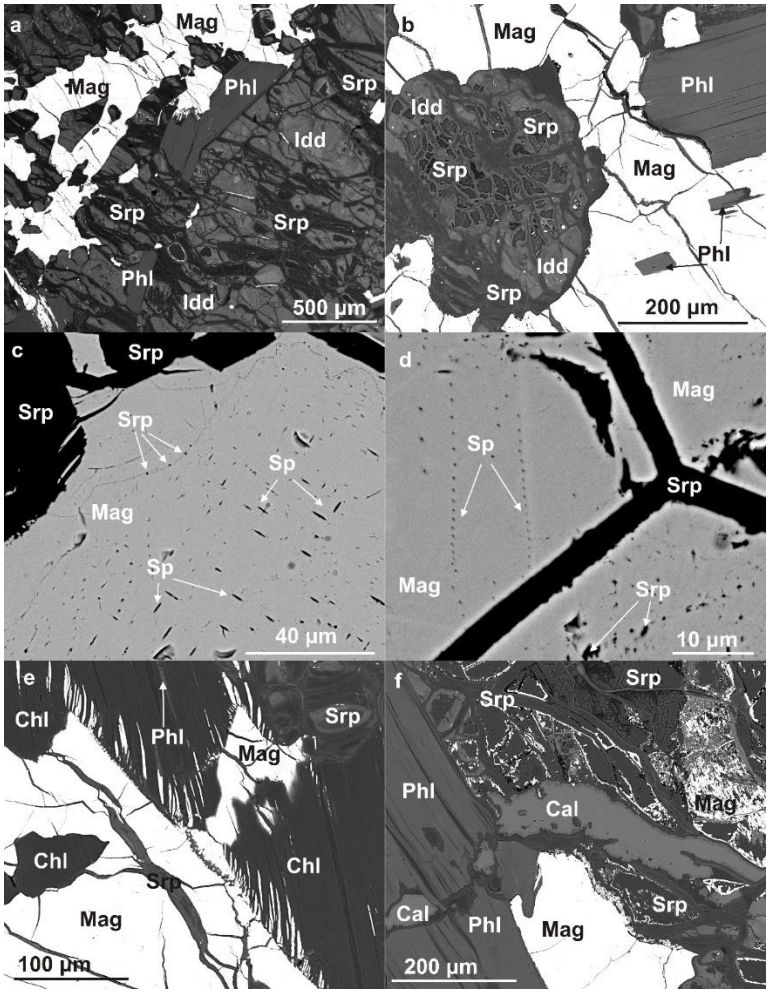

Fig. 4. BSE images of magnetite in sample D8-2. a. Cluster of magnetite distributed perpendicular to the late-stage serpentine meshwork. Note similar position of phlogopite flakes. b. Most grains follow boundaries of phlogopite and serpentine, replacing olivine. Small inclusions of phlogopite, partly altered to chlorite can be found in magnetite. c. A close-up of a magnetite grain shows distinct core and rim patterns. The core hosts orderly rows of spinel exsolutions, whilst the rim is dotted with small serpentine inclusions. The boundary is marked by a line of serpentine inclusions. d. Grains in the largest clusters meet at triple junctions. e. Phlogopite alteration to chlorite. As a result, small flakes of Fe in the form of magnetite are expelled. f. Calcite veinlet truncated by phlogopite. Note flakes of magnetite in

serpentine surrounding the veinlet. Abbreviations are as in the previous figures. Others are: Cal: calcite; Idd: iddingsite; Phl: phlogopite.

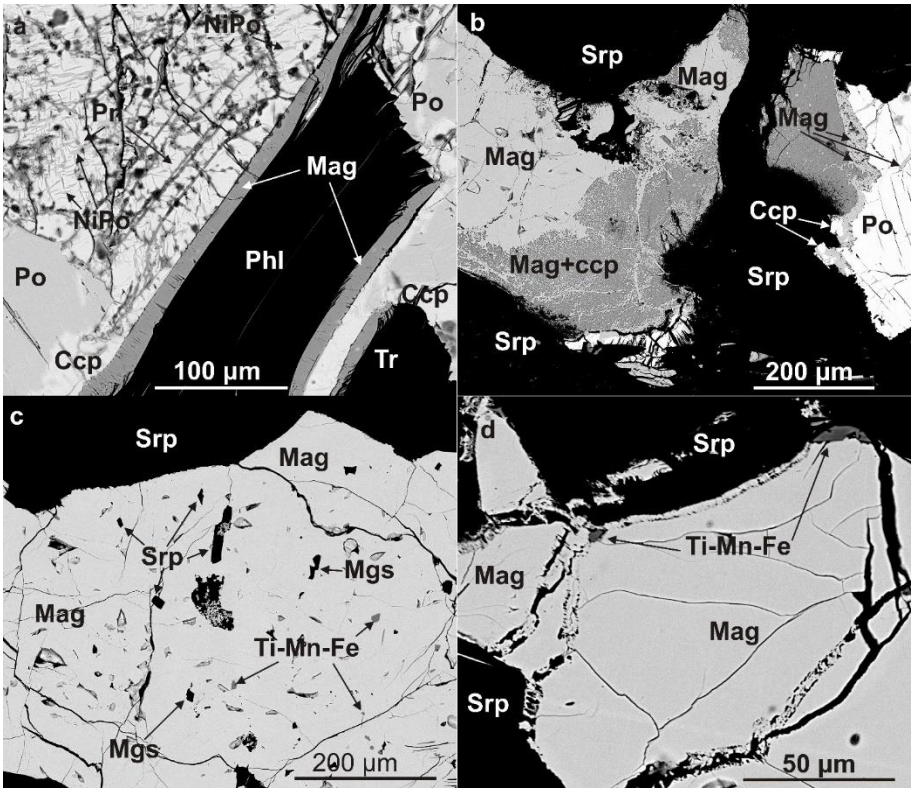

Fig. 5. BSE images of ores found in sample D8-7. a. Grains of pyrrhotite at the contact with phlogopite and tremolite, surrounded by magnetite. Most pyrrhotite has small exsolutions of chalcopyrite. The latter replaces pyrrhotite at the edges. Pyrrhotite rich in nickel has abundant exsolutions of pentlandite. b. Oxidation of pyrrhotite results in formation of magnetite and chalcopyrite. A mixture of the two host small grains of magnetite. This reaction is observed only in places affected by serpentinization. c. Magnetite cluster at the tremolitic rock-olivine lenses. The grains here are misshaped and does not meet at triple junction. d. Magnetite found in large clusters often show signs of dissolution. Small Ti-Mn-Fe oxide grains can be found next to magnetite or as inclusions. Abbreviations are as in the previous figures. Others are: Ccp: chalcopyrite; Mgs: magnesite; Pn: pentlandite; Po: pyrrhotite; Tr: tremolite.

Sample D8-7 is a phlogopite-bearing tremolite rock with lenses of olivine rock. Olivine is preserved only in some places, most of it is replaced by iddingsite and antigorite. Tremolite forms large grains engulfing olivine rock lenses. The rock is brecciated by serpentine veinlets, impregnated with fine grained magnetite. A few grains of phlogopite and chlorite can be found near the contact with olivine rock. Phlogopite is being replaced by magnesium-rich chlorite and small magnetites form as a result. Larger magnetites are intergrown with sulphides in the tremolitic rock. Pyrrhotite is the main sulphides found in the sample. The sulphide does not retain its primary composition due to the formation of exsolutions. Pyrrhotite rims are altered to chalcopyrite (Fig. 5a). Small chalcopyrite lamellae can be seen in the grains. Some parts of the pyrrhotite have an exsolution network of cobalt-enriched pentlandite (Fig. 5a). In some parts inclusions of olivine, partly altered to serpentine, can be seen in pyrrhotite. The sulphides overgrow phlogopite, surrounded by a film of fine-grained magnetite (Fig. 5a). Fine magnetite is distributed perpendicular to the sulphide grain boundary. Sulphide and magnetite aggregates found in tremolite rock affected by serpentinization show clear disequilibrium (Fig. 5b). Fine grained magnetite is distributed between pyrrhotite and a Cu-sulphide-Mg-Fe-silicate mixture that hosts small grains of magnetite. Olivine rock lenses are composed mostly of serpentine and iddingsite with islands of olivine. Flakes of magnetite are common in the serpentines. Larger magnetite aggregates are found at tremolitic rock and olivine lens contacts. Sulphides are scarce here. Magnetite grains vary in size. The largest are about 600 μm in length. No triple junction has been observed (Fig. 5c). Magnetites follow olivine relic boundaries and host small inclusions of Mn-rich ilmenite, magnesite and serpentine (Fig. 5c and d). The serpentine inclusions are rectangular. Grains of Mn-rich ilmenite often are found close to magnetite, or ingrown into magnetite at the contact with serpentine or olivine.

Sample 982-9 is a tremolite rock with minor phlogopite and serpentine replacing olivine. Tremolite here forms almost an monomineralic rock, brecciated by serpentine. A network of serpentine fractures becomes denser with depth. A few serpentine pseudomorphs, presumably formed after olivine, are present. Small chlorite flakes can be found next to olivine pseudomorphs. Magnetite is found as large grain clusters in the most brecciated part. Grains in some of the clusters are rounded and engulfed by an Fe-rich mineral, presumed to be iddingsite (Fig. 6a). The coarse-grained ore aggregates are surrounded with thin chlorite rims (Fig. 6b). Magnetite aggregates are formed of varying size grains. The largest grains are in distal positions from tremolite

(Fig. 6c). Grain size becomes smaller closer to the contact with tremolitic rock and magnetite grains there meet at triple junctions (Fig. 6c). Numerous monomineralic and composite inclusions are hosted by magnetite (Fig. 6d). The monomineralic inclusions are mostly composed of serpentine. Magnesite inclusions are very small and very rare. The composite inclusions are made up of either calcite, quartz and chlorite, or diopside and tremolite (Fig. 6e). Composite and monomineralic inclusions are distributed in rows within magnetite grains. Most magnetite grains are brecciated by a fine network of fractures. They are filled by chlorite-like mineral. Tiny grains of quartz and calcite can be seen in some of the larger cracks (Fig. 6f).

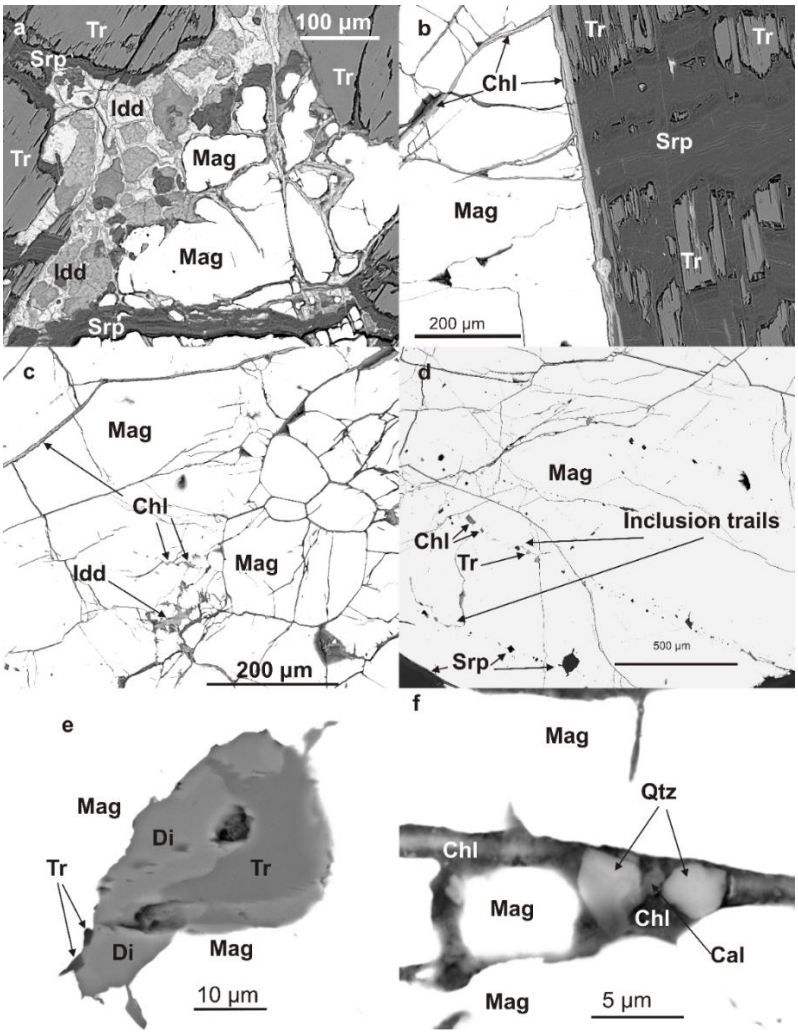

Fig. 6. BSE images of magnetite from sample 982-9. a. Slightly rounded magnetite grains surrounded by iddingsite. b. Magnetite cluster and tremolitic rock contact. Tremolite here is almost entirely replaced by serpentine. Magnetite is 'coated' by chlorite. The latter fills fractures in magnetite as well. c. Magnetite grain size decreases closer to the contact with tremolitic rock. Magnetite there is recrystallized and meets at triple junctions. d. Trails of inclusions trapped in magnetite during its growth. e. A close-up of a composite inclusion, composed of diopside, partly replaced to tremolite. f. A close-up of a fracture in magnetite. They are mostly filled by chlorite, but small quartz and calcite grains can also be found. Abbreviations are as in the previous figures. Others are: Di: diopside.

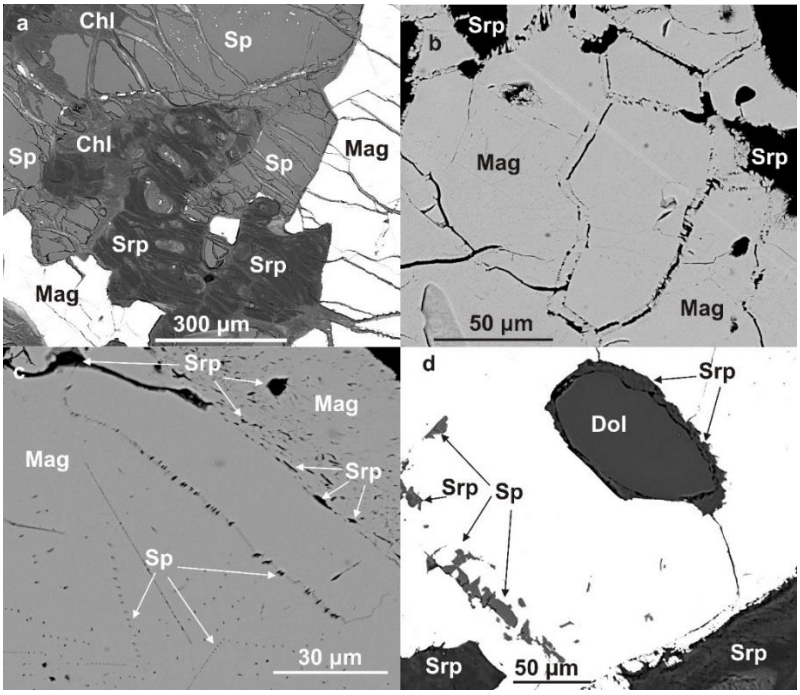

Fig. 7.BSE images of magnetite from sample 982-10. a. Magnetite grains nucleating along spinel boundary. Spinel is being replaced by chlorite. b. Magnetite grains in large clusters meet at triple junctions and often have a distinct rim. c. Close-up of magnetite grain. The core has abundant spinel exsolutions, whereas the rim is filled with serpentine inclusions. d. At the cores of some of the magneittes, inclusions of dolomite and spinel can be found. Dolomite is surrounded by serpentine. Abbreviations are as in the previous figures. Others are: Dol: dolomite.

Sample 982-10 is a spinel and olivine, phlogopite-bearing serpentinite. Antigorite serpentine and iddingsite replace olivine grains. Coarse spinel grains are rounded and being replaced by chlorite. A thick rim of chlorite often surrounds it. Phlogopite is abundant in the interstices between olivine, spinel and magnetite grains. It is partly or entirely replaced by chlorite. Magnetite nucleates along phlogopite replacement by chlorite. Magnetite in places is intergrown with spinel (Fig. 7a). Spinel often hosts small magnetite grains. The serpentine network filling the fractures is impregnated with smaller magnetite grains. Larger grains form euhedral crystals and larger crystal aggregates. Most of the grains in aggregates meet at triple junctions (Fig. 7b). Close examination shows that magnetite grains here have distinct cores, dotted by orderly rows of numerous spinel exsolutions (Fig. 7c). In a few cases, inclusions of spinel and dolomite were preserved in the core (Fig. 7d). Dolomite is surrounded by serpentine. The inclusion has fractures radiating from it. Magnetite rims are marked by a sharp boundary. It hosts abundant inclusions of serpentine, but no spinel was found in the rim (Fig. 7c).

4.3. Granitoids crosscutting the VIOD

Numerous granitoid veins crosscut the VIOD rocks, but their age and origin have not been studied until now. One of the studied samples, the D9/1083 albite leucogranite, has intruded the ca. 1.89 Ga (Šiliauskas et al., 2018) granodiorite. The granite has a sharp contact and is mainly composed of albitic plagioclase, quartz, K-feldspar and minor chlorite. Plagioclase is fine grained (1-0.5 mm and smaller) and often have albite twinning. Most grains are irregularly shaped and meet at triple junctions. Quartz is distributed around coarser plagioclase grains. Domains with sparse quartz often contain interstitial K-feldspar. Chlorite is the only mafic mineral found in larger amounts. If situated next to K-feldspar, it often contains small inclusions of titanite along the cleavage planes and probably has formed after biotite. A few unaltered biotite grains have been found surrounded by quartz. Accessory minerals are titanite, zircon, apatite and thorite. Coarser titanites host small thorite, allanite, calcite and yttrium-columbite-(Y) inclusions.

The V987/387 syenitic granite intruded clinopyroxene-amphibole-magnetite rocks. Contacts with the country rocks are sharp. The granite consists of K-feldspar, quartz, plagioclase and mafic minerals (less than 3%

of the rock). They are clinopyroxene, amphiboles and opaques. K-feldspar are small, up to 1.5 mm in some places. Quartz and plagioclase are of similar size and surround K-feldspar. The grain boundaries are more regular and meet at the triple junction in most cases. Clinopyroxene might come from the host rock, while amphibole is of igneous origin. Accessory minerals are titanite, zircon, apatite, epidote and ore minerals.

5. RESULTS

5.1 Rock chemistry

5.1.1 Rocks surrounding the VIOD

The rocks of the Lz13 drilling are generally rich in silica (SiO_2 62.02-70.30 wt %) and magnesium (MgO 3.03-4.34 wt%), but very poor in calcium (CaO 0.58-1.23 wt%) and alkalis (Na_2O 0.10-1.38 wt% and K_2O 0.21-1.60 wt%), indicating hydrothermal alteration prior to metamorphism (Table 1; II). This is very common for cordierite-orthorhombic amphibole schists (Hajash and Chandler, 1981; Shiraki et al., 1987 etc.). The alteration index of Lentz (1999) was used (Fig. 8) and illustrates plagioclase dissolution and the formation of secondary minerals like chlorite. The alteration index varies from 4.34 to 25.6 (II).

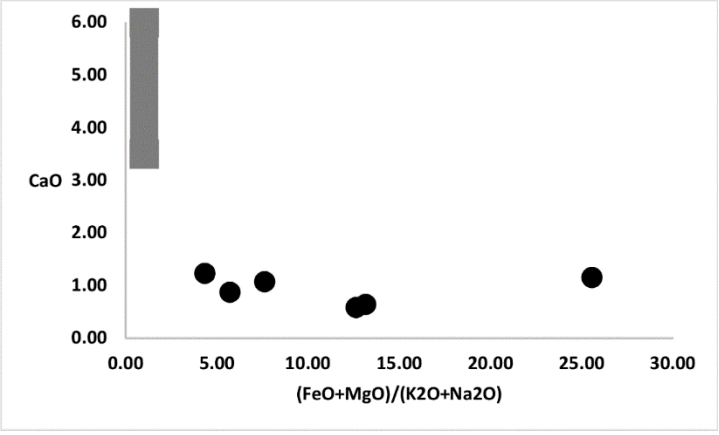

Fig. 8. Alteration index (Lentz, 1999) vs. CaO diagram for rocks from the Lz13 drilling. The grey area is andesites from Gill (1981).

Sample	SiO2	TiO2	Al2O3	Fe_2O_3	MnO	MgO	CaO	Na2O	K2O	P2O5	loi	Sum	Alteration ndex
Lz13/509.6	70,30	0,22	7,38	13,70	0,08	3,57	0,58	0,10	1,27	0,21	2,70	100,11	12,63
Lz13/515.9	64,85	0,27	9,78	16,20	0,15	3,90	1,15	0,36	0,21	0,09	1,48	98,44	25,56
Lz13/521.8	64,40	0,35	10,30	16,70	0,37	4,34	0,64	0,20	1,40	0,26	0,70	99,65	13,16
Lz13/528.1	62,02	0,31	11,86	15,65	0,08	3,45	1,07	0,36	1,42	0,21	2,14	98,57	7,62
Lz13/539.4	67,37	0,25	11,86	11,51	0,06	3,03	0,87	0,30	1,60	0,14	2,43	99,42	5,72
D9/4473	74.74	0.45	12.15	0.81	0.01	3.23	0.36	5.06	1.69	0.06	0.61	99.16	
D9/1083	76,57	0,10	13,52	0,20	0,01	0,23	1,57	6,04	1,08	0,02	0,60	99,93	
V987-387	62,11	0,20	17,38	1,55	0,04	0,71	2,09	1,91	11,09	0,07	1,04	98,20	

Table 1. Major element composition of the studied rocks.

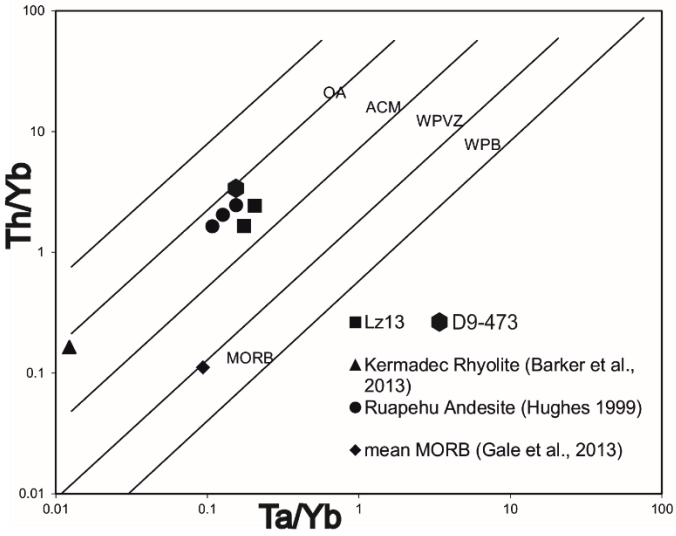

Fig. 8. Ta/Yb vs. Th/Yb tectonic discrimination diagram (Pearce, 1983) for felsic and intermediate rocks, modified by Gorton and Schandl (2000): OA: oceanic arc; ACM: active continental margins; WPVZ: within-plate volcanic zone; WPB: within plate basalts; MORB: Mid-ocean ridge basalts. Rhyolites from Kermadec (Barker et al., 2013), andesites from Ruapehu (Hughes, 1999) and mean MORB (Gales et al., 2013) compositions have been plotted for comparison.

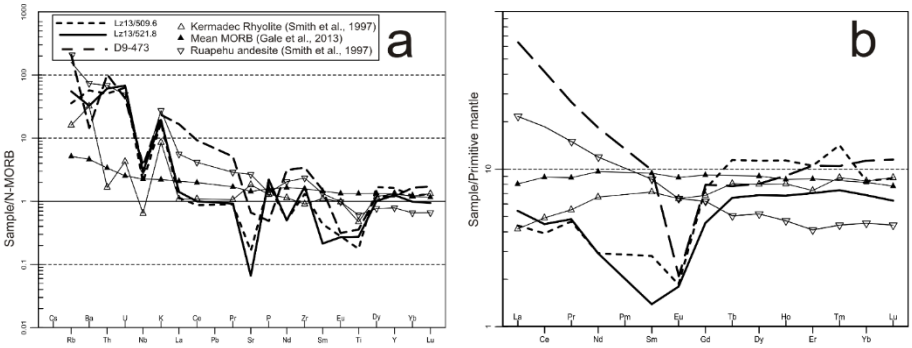

Fig. 9. Trace and REE element compositions of the studied volcanic rocks. a. Trace elements, normalized to N-MORB (Sun and McDonough, 1989). b. REE normalized to primitive mantle (McDonough and Sun, 1995). Compositions of volcanic rocks from primitive volcanic arcs (Smith et al., 1997) and mean MORB (Gales et al., 2013) have been plotted for comparison.

Sample	Lz13/509.6	Lz13/521.8	D9-473	D9/1083	V987-387
Be	359,00	205,00	6	85,00	1,00
Ba	1,18	1,22	91	145,00	2510,00
Co	n.d.	n.d.	3	0,30	1,80
Cs	n.d.	n.d.	1,2	0,10	0,40
Ga	15,40	25,10	13,9	18,00	17,20
Hf	2,99	2,87	7,9	4,00	6,30
Nb	4,72	6,84	8,6	26,00	35,70
Rb	20,00	30,90	116	33,00	289,95
Sn	2,96	3,71	1	1,00	3,00
Sr	14,80	5,96	60	174,00	146,84
Ta	0,65	0,62	0,6	3,30	1,70
Th	6,08	7,31	12,2	44,00	8,00
U	2,96	3,19	2	18,00	9,40
V	23,50	33,30	9	8,00	8,00
W	n.d.	n.d.	0,8	n.d.	0,50
Zr	97,00	126,00	252	83,00	179,08
Y	45,50	35,10	33	27,00	22,03
Mo	3,54	4,10	n.d.	2,00	n.d.
Cu	175,00	38,30	n.d.	5,00	n.d.
Pb	n.d.	n.d.	n.d.	6,00	n.d.
Zn	152,00	88,30	n.d.	11,00	49,95
Ni	9,04	8,76	n.d.	3,00	n.d.
As	n.d.	n.d.	n.d.	3,00	n.d.
Bi	n.d.	n.d.	n.d.	3,00	n.d.
Ge	n.d.	n.d.	n.d.	0,50	n.d.
La	2,84	3,52	41,5	37,00	7,70
Ce	6,54	7,49	69,3	74,60	15,60
Pr	1,18	1,22	6,74	7,48	2,27
Nd	3,65	3,65	22,8	24,20	10,40
Sm	1,14	0,56	3,98	4,09	2,95
Eu	0,29	0,28	0,32	0,54	0,58
Gd	4,06	2,47	4,32	3,54	3,10
Tb	1,13	0,65	0,77	0,59	0,54
Dy	7,62	4,60	5,43	3,65	3,29
Ho	1,69	1,01	1,35	0,82	0,77
Er	4,59	3,08	4,6	2,86	2,57
Tm	0,96	0,50	0,71	0,46	0,42
Yb	3,70	3,01	4,98	3,11	2,81
Lu	0,59	0,43	0,78	0,52	0,44

Table 2. Trace and RE element composition of the studied rocks.

Trace element composition of the studied rocks is presented in table 2. The Ta/Yb vs. Th/Yb tectonic discrimination diagram of Pearce (1983), modified by Gorton and Schandl (2000), was applied to the rocks. The Lz13 rocks plot in within the subduction-related, active continental margin field (Fig. 8; II). In a spider diagram (Fig. 9a), normalized to N-MORB (Sun and McDonough, 1989), compatible element concentrations are close to N-MORB. Incompatible elements are generally enriched, except for the light rare earths, which display substantial depletion. A pronounced negative Nb and Sr anomaly can be seen. Compared to the primitive mantle (McDonough and Sun, 1995; Fig. 9b), the samples are enriched in REE with a negative Eu anomaly. A characteristic feature of the REE spectra is the HREE enrichment over LREE. Compared to the composition of modern volcanic rocks from different tectonic settings, depletion in LREE and especially in MREE is higher than in MORB (Gale et al., 2013). However, the distribution of incompatible elements and HREE is similar to unaltered primitive volcanic arc rocks (Barker et al., 2013; Hughes, 1999; Smith et al., 1997; II).

5.1.2. The VIOD rocks

The D9-473 gneiss is rich in silica (74.74 wt% SiO_2) and has high magnesium and low calcium contents (3.23 wt% MgO and 0.36 wt% CaO), much like the rocks from Lz13 drilling. The D9-473 sample, however, contains higher amounts of alkalis. It is richer in sodium (5.06 wt% Na_2O) than potassium (1.69 wt% K_2O). For comparison, the alteration index of Lentz (1999) was calculated for this sample. It reaches a value of 0.48, indicating only minor alteration.

In the Ta/Yb vs. Th/Yb tectonic setting discrimination diagram (Pearce, 1983, Gorton and Schandl. 2000), D9-473 sample plots within the active continental margin field (Fig. 8). In the N-MORB (Sun and McDonough, 1989) normalized trace element diagram (Fig. 9a) large-ion lithophile element (LILE) enrichment over high-field strength elements (HFSE) is prominent. Nb, Sr, P, Eu and Ti negative anomalies can be seen, indicating a subduction-related tectonic setting and fractionation of plagioclase and phosphates. REEs in the primitive mantle normalized diagram (McDonough and Sun, 1995) show LREE enrichment over the HREE (Fig. 9b). A prominent negative Eu anomaly is observed.

5.1.3. Granites crosscutting the VIOD rocks

The studied granitoids differ in their major element content (table 1). These rocks are metaluminous, rich in alkalis and have low TiO_2, MgO and FeO contents. The D9/1083 leucogranite is richer in silica (SiO_2 76.57 wt%) and is more sodic (Na_2O 6.04 wt% and K_2O 1.08 wt%). The V987/387 syenitic granite has 62.11 wt% of SiO_2, very little sodium (Na_2O 0.191 wt%) and high amount of potassium (K_2O 11.09 wt%; IV).

Trace and REE element compositions of these rocks are presented in table2. Both granitoids share A-type granite affinities. In the tectonic discrimination diagram (Pearce et al., 1984) they plot in within-plate tectonic setting, based on their Y, Nb and Rb contents (IV). Low Zr/Hf ratios (20.75 for D9/1083 and 28.43 for V987/387) indicate that both rocks can be regarded as extremely fractionated (Breiter et al., 2014; IV).

In the N-MORB-normalised (Sun and McDonough, 1989) spider diagram (Fig. 11a), trace elements show incompatible element enrichment over the compatible ones and Sr, P and Ti negative anomalies (IV). This indicates fractionation of such minerals as apatite and monazite in the case of phosphorus and titanite or ilmenite for titanium. There are no negative Nb anomalies. The enrichment in compatible elements is not as high in D9/1083 leucogranite and its spectrum also contains a positive Th anomaly, as well as a slightly negative Ba anomaly. The low amounts of Sr, K and Ba indicate fractionation of plagioclase and K-feldspar, that depleted the magma in these elements.

The REE content is low: Σ_{REE}=163 (D9/1083) and Σ_{REE}=53 (V987/387; IV). The REE spectra (Fig. 11b), normalised to chondrite of Nakamura (1974), of both samples are similar in their HREE distribution, but the syenitic granite has a higher LREE content: La_N/Yb_N is 5.56 and 1.61, in D9-1083 and V987-387, respectively (IV). Both samples show a negative Eu anomaly, indicative of plagioclase fractionation.

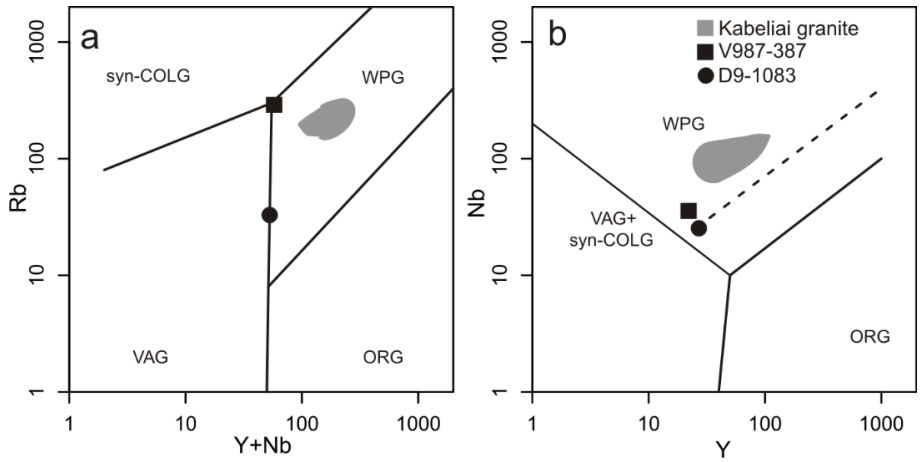

Fig. 10. Tectonic setting discrimination diagrams based on Y+Nb vs. Rb (a) and Y vs. Nb (b) ratios (Pearce et al., 1984). Chemical composition of the Kabeliai granites has been plotted for comparison. The abbreviations used are as follows: syn-COLG – syncollisional granites, VAG – volcanic arc granite, WPG – within-plate granite, ORG – ocean ridge granite.

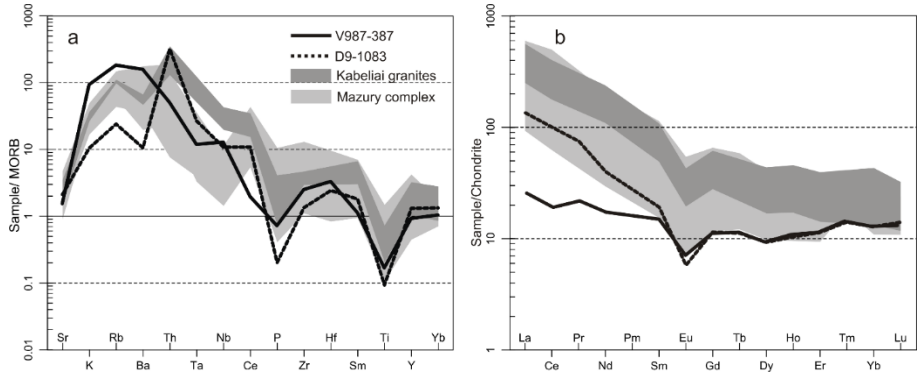

Fig. 11. The N-MORB (Sun and McDonough, 1989) normalized trace element patterns (a) and (b) chondrite (Nakamura,1974) normalized REE element patterns (b). Compositions of rocks from the Kabeliai granites and the Mazury (Skridlaite et al., 2003) complex are plotted for comparison.

5.2. P-T estimates

5.2.1. Rocks surrounding the VIOD

In the gedrite-bearing metavolcanic (Lz13/521.8), an assemblage of (Grt_{core}+Bt_{matrix}+$Pl_{An\ 39-35}$) recorded peak conditions of 620-630 ˚C at 5-6 kbar, while isopleths of the same garnet showed a slightly higher pressure: 610-620˚ C and 7 kbar (Fig. 12; II). Lower pressure estimates obtained using the geothermobarometer of Holdaway (2000) can be explained by the absence of plagioclase in equilibrium with garnet cores. According to the pseudosection, the amount of plagioclase at peak conditions is minute and it could have been consumed during later metamorphism. The local absence of staurolite in the sample can be explained by staurolite-consuming, garnet-producing reaction at the temperature maximum. A drop of pressure to 4 kbar and temperature of 580-600 °C was obtained from a garnet rim, porphyroblastic biotite and plagioclase (An_{40-49}) inclusions in quartz (II). Garnet rim isopleths recorded temperature of 610-620° C and 5-6 kbar pressure (II). Similar results were obtained from garnet rim and chlorite thermobarometry (575-620˚ C at 5-6 kbar, within the chlorite stability field; Grambling, 1990; II). The first appearance of anthophyllite can be attributed to uplift, at 610° C and 4.5 kbar (II). The gedrite-anthophyllite solvus (Spear, 1980) yielded a minimum temperature of 545±23° C. During the retrogression anthophyllite was replaced by gedrite via the reaction: anthophyllite + albite in plagioclase + cordierite = gedrite (Schneiderman and Tracy, 1991). This reaction explains why orthoamphiboles are often surrounded by anorthitic plagioclase and anthophyllite is never found with cordierite. Plagioclase has been continuously consumed by the gedrite-producing reaction. The reaction was terminated when the anthophyllite was consumed, leaving behind anorthitic plagioclase.

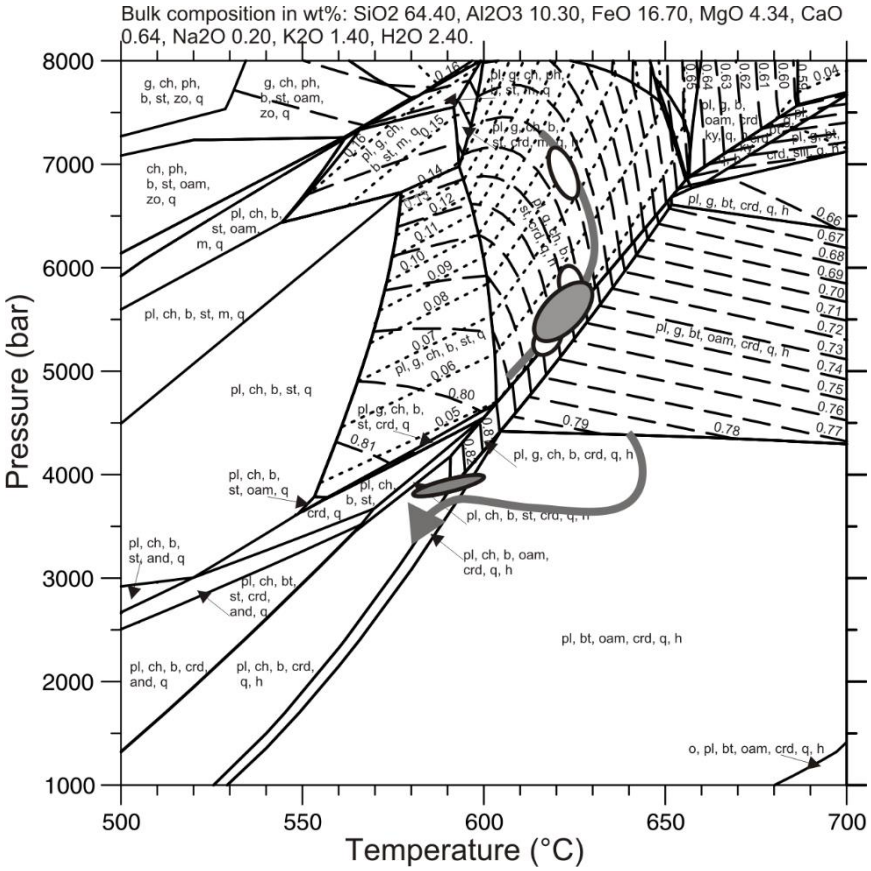

Fig. 12. Sample Lz13/521.8 pseudosection for CNKFMASH system and garnet composition isopleths. Thermobarometry results are shown by grey ellipses, while white ellipses represent garnet compositions as measured in the thin section. Mineral abbreviations used are: pl: plagioclase; b: biotite, oam: orthoamphibole; crd; cordierite; o: olivine; q: quartz; g: garnet; sill: sillimanite; st: staurolite; ky: kyanite; ch: chlorite; ph: phengite; m: margarite; zo; zoisite; and: andalusite; h: water. The grossular and almandine contents are shown by dotted and dashed lines, respectively.

In the orthorhombic amphibole-free sample (Lz13/540) an assemblage of plagioclase, chlorite, biotite, staurolite and quartz was stable at the peak conditions (620° C and 7 kbar). Staurolite in the matrix and cordierite and garnet porphyroblasts suggest that garnet grew at the expense of staurolite. Subsequent uplift caused garnet decomposition to cordierite and chlorite via reaction: garnet = chlorite + cordierite + quartz. New skeletal garnet growth

at the expense of cordierite and staurolite was recorded by garnet isopleths. Temperatures of 630-640˚ C at a pressure of 3.5-4.5 kbar was recorded in a gedrite-free assemblage (Lz13/540; Fig. 13; II). The pressure did not drop below 3.5 kbar, where the orthorhombic amphibole stability field begins, therefore it is absent in sample Lz13/540. According to the pseudosection of sample Lz13/521.8, gedrite-bearing rocks at those conditions were outside the garnet stability field (Fig. 12). Formation of new staurolite in the matrix may have occurred at the expense of garnet during the retrogression stage. A summary of the PT estimates is presented in table 3.

	Sample	Assemblage	Thermometer	Barometer	T, °C	P, kbar	Grt isopleths T, °C	Grt isopleths P, kbar
Burial	521.8	Grt(core)+Bt(matrix)+Pl(An_{39-35})	Holdaway 2000	Holdaway 2000	630-620	6-5	610-620	7
Retrograde	521.8	Grt(rim)+Bt+Pl(An_{40-49})	Holdaway 2000	Holdaway 2000	600-583	4.0	620	6-5
	521.8	Grt(rim)+Chl	Grambling 1990		575-618		610-620	6-5
Reheating	540	Pl+Grt+Bt+Crd					630-640	3.5-4.5

Table 3. PT estimations in Lz13 rocks. Abbreviations used here as follows: An: anorthite; Bt: biotite; Chl: chlorite; Crd: cordierite: Grt: garnet: Pl: plagioclase.

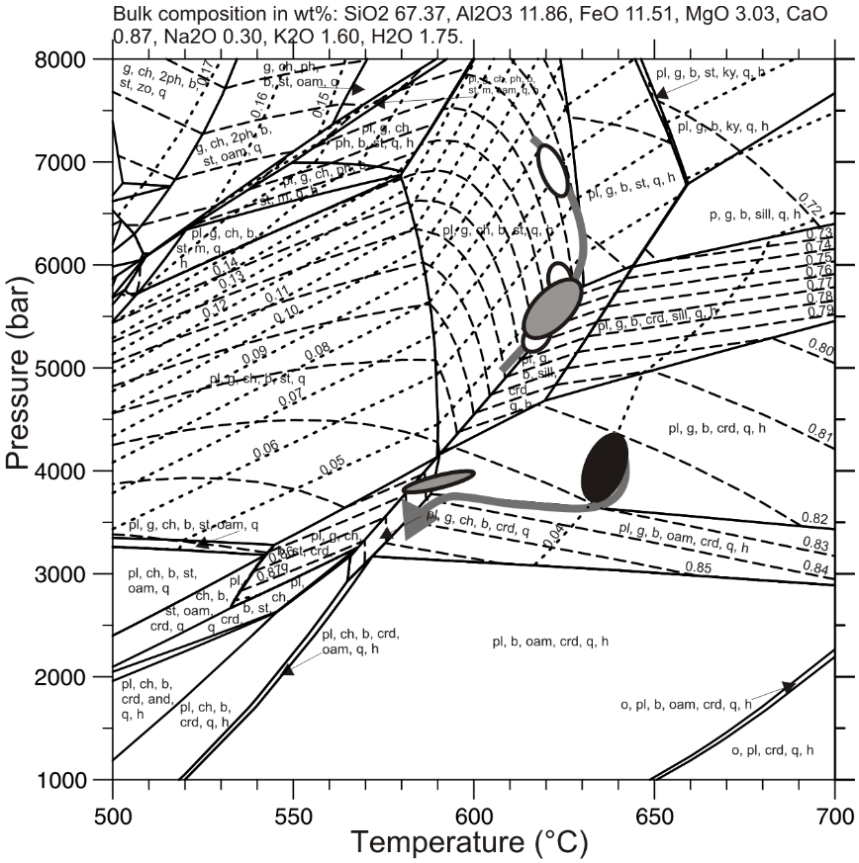

Fig. 13. Sample Lz13/540 pseudosection for CNKFMASH system and garnet composition isopleths. Black ellipse represents garnet composition as measured in the thin section, while grey and white ellipses are those obtained in sample Lz13/521.8. Mineral abbreviations used are as used in fig. 2. The grossular and almandine content is presented by dotted and dashed lines, respectively.

5.2.2. The VIOD rocks

An empirical equation fitted on calcite-dolomite solvus limbs (Anovitz and Essene, 1987) was used to evaluate calcite crystallization temperatures in sample 982-4 (Table 4). A correction for iron present in the carbonates has been applied (Anovitz and Essene, 1987). The thermometer is not dependent on fluid compositions but can be reset during retrograde stages (Essene, 1983),

thus is considered to represent a minimum temperature. Core compositions (X_{MgCO3} 0.11-0.04) of the largest calcite grains from the matrix were used for the calculations. The Mg content decreases rapidly towards the contact with dolomite. A few larger grains (X_{MgCO3} 0.19-0.09) from the serpentine replacements after olivine were also taken for calculations. The average temperature calculated from the cores of matrix calcite is 590˚ C, while the calcite within olivine grains recorded a higher temperature of 680˚ C.

Location	Calcite in Olivine			Matrix		
ID	2_13	4_21	6_7	1_6	2_19	5_4
CaO	49,72	47,88	47,9	47,84	48,41	48,55
MgO	3,83	4,58	4,98	2,48	2,88	2,88
MnO	0,28	0,7	0,26	1,02	0,97	0,48
FeO	0,88	1,13	0,94	0,42	0,36	1,52
Total	54,71	54,29	54,08	51,76	52,62	53,43
	No of catons, based on 6 oxygen atoms					
Ca	1,777	1,720	1,718	1,825	1,811	1,794
Mg	0,190	0,229	0,248	0,132	0,150	0,148
Mn	0,008	0,020	0,007	0,031	0,029	0,014
Fe	0,025	0,032	0,026	0,013	0,011	0,044
C	2,000	2,000	2,000	2,000	2,000	2,000
X_{Mg}	0,10	0,11	0,12	0,07	0,07	0,07
X_{Fe}	0,01	0,02	0,01	0,01	0,01	0,02
T (°C)	643	677	691	574	598	596
T_{Fe} (°C)	639	667	680	576	599	601

Table 4. Representative analyses of calcite and results of calcite-dolomite thermometry (Anovitz and Essene, 1987). T_{Fe} are temperatures corrected for iron content in calcite.

5.2.3. The crosscutting granitoids

Zircon saturation temperatures (T_{Zr}, Watson and Harrison, 1983) were calculated for the dated granitic rocks (D9/1083 and V987/387). Temperature of 728˚ C (M 1.45) and 763˚ C (M 1.85; M – cation ratio (Na + K + 2Ca) / (Al * Si)) were recorded by samples D9/1083 and V987/387, respectively. The rocks are metaluminous, cold (T_{Zr}<800˚ C) granites of late stage, therefore the T_{Zr} approximates the temperature of melt segregation, providing a minimum temperature of the initial magma emplacement (Miller et al., 2003). In sample D9/1083 CPWI, a normative composition was used to estimate the pressure of emplacement, as proposed by Yang (2017). The calculated pressure is ca. 1.0-0.9 kbar. Similar calculations were performed for the syenitic granite V987/387, but the obtained pressure was unrealistically high due to the high K-feldspar content.

5.3. Magnetite microtextures and chemical compositions

Chemical analyses of Sample D8-1 magnetites that form larger aggregates are presented in table A7. They are rich in magnesium (0.32-0.4 wt% Mg) and aluminium (0.14-0.28 wt% Al) and have low amounts of titanium (0.20-0.27 wt% Ti) and vanadium (up to 0.14 wt% V; I). The vanadium content decreases at the grain edges.

Chemical analyses of magnetite from the largest clusters in sample D8-2 are presented in table A8. They have somewhat lower amounts of magnesium (0.15-0.25 wt% Mg) and very low content of aluminium (0.07-0.08 wt% Al), compared to sample D8-1 (I). Titanium concentration, however, is very similar (0.19-0.24 wt% Ti; I). Vanadium content in this sample is below the detection limit of EPMA (~700 ppm). A few grains of hematite found in calcite veinlets and close to them were also studied. Their chemical composition, presented in table A8, is very pure. Only traces of silica (up to 0.12 wt% Si) and rather high concentration of Zn (up to 1.08 wt% Zn) were detected (I). Other measured elements were below the detection limit of EPMA.

Chemical analyses of D8-7 magnetite at the contact of tremolite rock and olivine lenses are presented in table A9. These grains have no triple junctions and small rims. The core composition differs from that of the rim. Cores have variable amounts of magnesium (0.23-0.47 wt%; I). Titanium and silica were detected in some analyses, varying from 0 to 0.26 wt% and 0 to 0.20 wt%,

respectively (I). The rims and magnetite formed as a result of phlogopite alteration to chlorite, on the other hand, have strict chemical composition: magnesium 0.19-0.24 wt% (Mg), aluminium 0.03-0.05 wt% (Al) and titanium 0.18-0.25 wt% (Ti; I).

Magnetite in sample 982-9 is presented in table A10. The analyses showed that large grains further away from the contact with tremolitic rock are chemically indistinguishable from those at the contact. As in other samples, the magnetites are enriched in magnesium (0.03-0.22 wt% Mg; III). They are very poor in aluminium (up to 0.09 wt% Al, average 0.04 wt%; III). In several spots it was below the detection limit of EPMA (300 ppm). Unlike the previous samples, 982-9 magnetites contain substantial amounts of manganese (0.04-0.20 wt% Mn, 0.12 wt% on average; III). The lowest values of Mn were detected close to the cracks and grain edges. Concentrations of titanium and vanadium are generally low, only a few analyses yielded concentrations above the detection limit of EPMA (400 and 700 ppm, respectively).

Most of the analyses carried out on sample 982-10 are from large magnetite clusters, surrounding the olivine pseudomorphs and spinel grains. Chemical analyses are presented in table A10. Three analyses were taken from the larger grain overgrowths. Large magnetite grains are rich in magnesium (0.26-0.76 wt% Mg, 0.34 wt% on average; III). They are richer in aluminium than other samples (0.11-0.92 wt% Al, 0.23 wt% on average; III). In some grain parts traces of nickel (up to 0.15 wt% Ni) were detected. These values are just above the detection limit of EPMA. Titanium was detected in all samples, except sample no 3. Concentration of titanium varies from 0.03 to 0.07 wt% Ti. The chemical composition of the overgrowths differs from the cores (III). They are slightly lower in magnesium (0.05-0.27 wt% Mg), but richer in silica (0.08-0.45 wt% Si in rims and up to 0.03 wt% Si in the cores; III). The titanium content of the overgrowths is below the detection limit of EPMA (~400 ppm).

To sum up, magnetites in Varėna Iron ore deposit are generally rich in magnesium and have very low concentrations of other elements. Magnetite that forms overgrowths around olivine replacement and contain spinel exsolutions tend to have higher amounts of aluminium. All the magnetites are low in titanium. Ores in tremolite rock have higher amounts of manganese. The late-stage magnetite overgrowths are generally richer in silica than the cores that they surround.

5.4. Zircon and monazite dating results

5.4.1. The rocks surrounding the VIOD

In the Lz13/521.8 gedrite-bearing metavolcanic, zircons are situated in the fine-grained matrix or as inclusions in biotite and garnet. The dating results are presented in table 5. They are oval-shaped and small (60-80 μm in average). In CL images, only thin lighter and darker zones can be seen. The light and dark domains have distinct U contents, with U up to 263 in white parts of the grain and 1863 in the dark parts (II). The ages obtained in the light parts is slightly older than those from dark domains. The youngest $^{207}Pb/^{206}Pb$ age obtained from the most U-enriched domain (2167 ppm) is 1730±5 Ma (Fig. 14a; II). The best estimate of the crystallization age was obtained from three concordant and near-concordant grains at ca. 1830±27 Ma with a mean square weighted deviation (MSWD) of 2.8 and a probability of 0.06 (Fig. 14b; II). Most of the data scatter along two trends on the Concordia diagram, indicating ancient (along the Concordia with maximum age of ca. 1730 Ma) and present-day lead loss (sub-horizontal trend) episodes (Fig. 14; II). Scattering to the right of the trend along the Concordia can be regarded as recent lead loss superimposed on an ancient one. $^{207}Pb/^{206}Pb$ weighted average age of six oldest grains gives estimate of 1831±14 Ma with MSWD of 2.7 and probability of 0.02 (Fig. 14c; II). The data show that crystallization of zircons from the melt took place at ca. 1830 Ma, followed by resetting at ca. 1730 Ma (or lower).

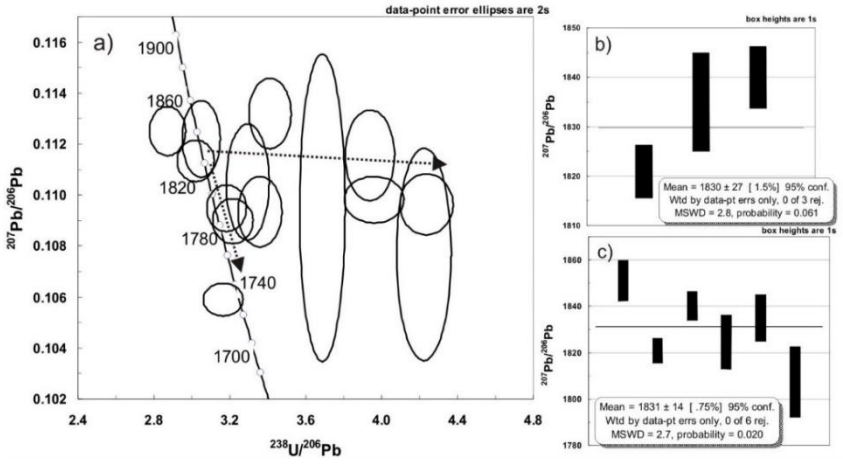

Fig. 14. a) Tera-Wasserburg Concordia for the Lz13/521.8 zircons. $^{207}Pb/^{206}Pb$ average ages for the same sample are presented in b) and c). Analyses with the greatest errors (>25%) and discordance of more than ±10% were excluded. The younger ages were obtained from the dark CL domains in zircons. These data scatter along the Concordia and represent ancient lead loss, whereas the rest of the analyses represent recent lead loss.

Monazites in gedrite-free sample Lz13/540 are very small. They are located either as inclusions in magnetite and cordierite, or at biotite-cordierite boundaries in the matrix. The grains are anhedral. Back-scattered electron (BSE) imaging showed that the monazites are homogeneous. In general, they are rich in ThO_2, with an average of 10 wt% and low in heavy rare earth elements (Table 6; II). Grains included in cordierite and at cordierite-biotite junctions are richer in Y (Y_2O_3 1.7-1.3 wt%) and Th. The average Y_2O_3 in other grains is 0.63 wt% (II). The single spot ages overlap with each other within the errors. The weighted average age was calculated at 1473±30 Ma (n=12) with MSWD of 2.6 and probability of 0.002 (Fig. 15a; II).

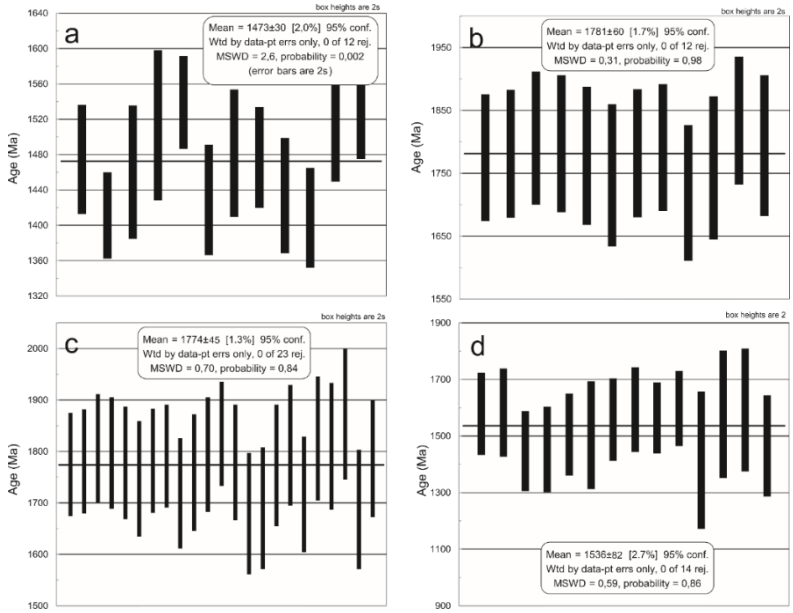

Fig. 15. Weighted average ages of monazites from samples Lz13/540 a) and 982-4 b-d). Core age of the best-preserved grain b) is within the error of dark BSE cores found in the sample c). Brighter BSE rims and smallest monazites age d) is much younger.

Sample/session/spot#	[U] (ppm)	[Th] (ppm)	[Pb] (ppm)	Th/U (calc)	Th/U (meas)	f_{206} %[a]	$^{206}Pb/^{238}U$	±s (%)	$^{206}Pb/^{238}U$	± s	$^{207}Pb/^{206}Pb$	± s (%)	$^{207}Pb/^{206}Pb$	± s	Disc. % 2s lim.
n3229-9a	279,9	215,2	97,3	0,69	0,77	{0.02}	0,25386	1,34554	1458,4	1 7,6	0,111530	0 ,65	1824,5	1 1,8	-18,7
n3229-9b	1213,3	207,9	358,2	0,16	0,17	0,16	0,25252	1,63089	1451,5	2 1,2	0,109785	0 ,34	1795,8	6 ,1	-18,4
n3229-12a	263,3	99,0	93,6	0,30	0,38	0,07	0,29316	1,33754	1657,3	1 9,6	0,113666	0 ,48	1851,0	8 ,9	-8,6
n3229-12b	1357,8	198,6	484,9	0,14	0,15	0,11	0,31080	1,35734	1744,6	2 0,8	0,109758	0 ,32	1781,8	6 ,0	
n3229-14	1055,0	201,6	380,3	0,25	0,19	1,64	0,30331	1,40571	1707,7	2 1,1	0,122372	0 ,32	1807,4	1 5,2	-1,6
n3229-16b	1863,4	128,2	660,9	0,07	0,07	0,02	0,31411	1,32813	1760,9	2 0,5	0,109630	0 ,33	1790,4	6 ,1	
n3229-16a	398,5	178,7	132,2	0,76	0,45	6,07	0,23676	1,40675	1369,8	1 7,4	0,107653	1 ,58	1760,1	2 8,6	-16,9
n3229-20b	431,1	348,9	171,2	0,72	0,81	0,47	0,29771	1,40609	1679,9	2 0,8	0,112773	0 ,40	1788,4	9 ,4	-3,3
n3229-20a	2167,4	35,7	760,0	0,02	0,02	0,01	0,31574	1,33069	1768,9	2 0,6	0,105926	0 ,25	1729,7	4 ,5	
n3229-18_1b	1230,1	144,0	465,9	0,11	0,12	0,02	0,33116	1,32330	1844,0	2 1,3	0,111422	0 ,30	1820,9	5 ,4	
n3229-18_1a	483,0	206,9	207,2	0,44	0,43	{0.01}	0,34821	1,31926	1926,1	2 3,0	0,112487	0 ,35	1840,0	6 ,3	2,1
n3229-18_2	422,1	325,0	136,0	0,65	0,77	0,04	0,23604	1,34836	1366,1	1 6,6	0,109620	0 ,45	1793,1	8 ,2	-23,5
n3229-21	163,2	86,9	63,4	0,95	0,53	5,97	0,27111	1,33200	1546,4	1 8,3	0,152791	1 ,13	1790,6	4 0,4	-4,7
n3229-22_2	208,9	132,3	88,8	0,63	0,63	0,04	0,32791	1,35344	1828,3	2 1,6	0,112500	0 ,54	1835,0	1 0,0	
D9-473-1	4277 0,1	8876 8,5	2243 9,0	1,51	5,08	0,01	0,33884	1,04554	1881,1	9 ,9	0,112673	0 ,48	1843,0	8 ,8	

Table 5. Lz13/521.8 zircon dating results. Dating results of single zircon from sample D9-473 has been added

Analysis	P	La	Ce	Pr	Nd	Sm	Gd	Tb	Dy	Ho	Er	Yb	Pb	U	Th
#2	12.37	10.50	20.61	2.13	8.71	1.85	1.43	0.00	0.49	0.00	0.10	0.00	0.67	0.35	8.90
#3	12.34	9.89	19.75	2.23	8.60	1.79	1.24	0.00	0.18	0.00	0.00	0.00	0.85	0.39	12.08
#4	12.66	11.07	22.29	2.43	9.77	1.88	1.37	0.00	0.22	0.00	0.00	0.00	0.52	0.19	7.27
#5	13.55	12.24	23.33	2.38	9.21	1.71	1.03	0.00	0.24	0.00	0.00	0.00	0.49	0.52	5.44
#7	12.92	9.55	18.91	1.99	8.33	1.75	1.46	0.00	0.36	0.00	0.00	0.00	0.88	0.32	11.52
#8	13.44	11.39	21.68	2.23	8.98	1.56	0.98	0.00	0.17	0.00	0.00	0.00	0.64	0.55	8.22
#9	13.68	11.33	21.62	2.25	8.75	1.66	1.37	0.00	0.33	0.00	0.00	0.00	0.57	0.25	7.77
#10	12.29	10.65	20.92	2.27	8.74	1.69	1.19	0.00	0.25	0.00	0.00	0.00	0.73	0.54	9.21
#27	12.91	10.65	20.43	2.26	9.08	1.97	1.58	0.00	0.48	0.00	0.00	0.00	0.62	0.31	8.51
#28	12.55	9.88	20.21	2.21	8.90	1.97	1.45	0.00	0.50	0.00	0.00	0.00	0.71	0.42	9.77
#30	12.66	10.17	19.76	2.16	8.88	1.76	1.39	0.00	0.40	0.00	0.11	0.00	0.74	0.32	9.77
#36	12.57	9.57	18.11	2.07	7.94	1.53	1.01	0.00	0.22	0.00	0.00	0.00	1.02	0.59	12.95
det.lim.	0.01	0.05	0.04	0.07	0.10	0.14	0.12	0.13	0.16	0.13	0.07	0.08	0.02	0.02	0.04

Table 6. Monazite chemical analyses and single point ages from sample Lz13/540.

Ca	S	Y	Si	O	Total	Age (Ma)	1σ
1.38	0.00	1.19	0.32	26.36	97.63	1474.90	30.65
1.90	0.00	0.42	0.45	26.52	98.71	1411.60	24.13
1.29	0.00	0.63	0.25	26.73	98.71	1460.58	37.47
1.00	0.00	0.53	0.25	27.72	99.72	1513.53	42.18
1.71	0.00	1.04	0.43	27.06	98.53	1539.32	25.97
1.43	0.00	0.52	0.26	27.64	99.89	1429.28	31.06
1.22	0.00	0.91	0.30	27.95	100.23	1481.91	35.76
1.56	0.00	0.59	0.33	26.22	97.37	1477.18	28.29
1.26	0.00	1.09	0.30	27.01	98.89	1434.11	32.36
1.58	0.00	1.34	0.32	26.72	98.84	1409.09	27.99
1.30	0.00	1.10	0.54	26.83	98.15	1509.01	29.32
2.04	0.00	0.75	0.31	26.45	97.35	1520.80	22.43
0.01	0.01	0.02	0.01				

Continuation of Table 6. Monazite chemical analyses and single point ages from sample Lz13/540.

5.4.2. The VIOD rocks and ores

Zircon grains were separated from sample D9-473 at the Nature Research Centre for age determination. Zircons are small (about 40 μm in length), slightly rounded prisms. The width/length ratio is 1:2. Brighter CL cores and dark CL rims can be seen. Due to technical difficulties, insufficient data were gathered to construct a Concordia diagram. Most data are discordant. A single point plots on the Concordia diagram. It has a Th/U ratio of 2.08. The $^{207}Pb/^{206}Pb$ age is 1843±9 Ma, giving a rough estimate of the volcanism (Table 5).

Monazites are found in a narrow zone in the 982-4 calciphyre. They are in a carbonate matrix, often in contact with or close to serpentinized olivine grains. Monazites are partly surrounded by serpentine that hosts small flakes of magnetite. Calcite is often replaced by dolomite at the edges. Monazite contacts calcite and olivine at triple junction. Grain size varies from 20 μm to 250 μm in length (Fig. 16). The largest monazite grains from sample 982-4 are euhedral or subhedral. These grains are often fractured. Fractures are filled with serpentine. Monazites have dark cores, richer in Th and Y and slightly lighter irregular rims in BSE images. The Th content at the core is generally above 2 wt%, except for the darkest domains, while in the rim it varies from 0.95 wt% to 2.13 wt% (table 7; III). The rim also has slightly higher LREE content. The smallest monazite grains are anhedral and unfractured. In BSE images they are homogeneous. Their chemical composition is very similar to the composition of larger grain rims. All monazites found in sample 982-4 have a U content below the detection limit of the Cameca EPMA (95 ppm; III).

Based on the chemical composition and location in the grain, dating results were subdivided into two groups. The results showed that the age of cores is much older than that of the rims and the smallest grains. Single-spot ages in the core range from 4.3 to 1.68 Ga. The spots with oldest ages have very low Th content and very high errors, thus were dismissed from further calculations. The remaining single-spot ages from the cores range from 1.87 to 1.68 Ga. The core of the best-preserved grain yielded an average age of 1781±60 Ma (Fig. 15b; n=12, MSWD=0.77), which is similar within error to the average age of all cores, 1774±45 Ma (Fig. 15c; n=23; MSWD=0.17; III). The remaining single-spot analyses from the rims and smallest grains range in

age from 1.59 to 1.41 Ga and overlap within their errors (III). The average age was calculated at 1536±82 Ma (Fig. 51d; n=14, MSWD=0.15; III).

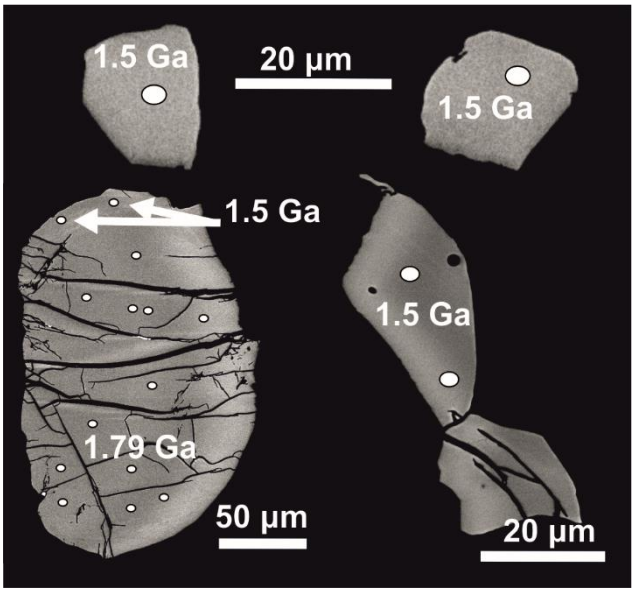

Fig. 16. BSE images of monazites from sample 982-4.

Based on the chemical composition and location in the grain, dating results were subdivided into two groups. The results showed that the age of cores is much older than that of the rims and the smallest grains. Single-spot ages in the core range from 4.3 to 1.68 Ga. The spots with oldest ages have very low Th content and very high errors, thus were dismissed from further calculations. The remaining single-spot ages from the cores range from 1.87 to 1.68 Ga. The core of the best-preserved grain yielded an average age of 1781±60 Ma (Fig. 15b; n=12, MSWD=0.77), which is similar within error to the average age of all cores, 1774±45 Ma (Fig. 15c; n=23; MSWD=0.17; III). The remaining single-spot analyses from the rims and smallest grains range in age from 1.59 to 1.41 Ga and overlap within their errors (III). The average age was calculated at 1536±82 Ma (Fig. 51d; n=14, MSWD=0.15; III).

No	P	Y	Si	Sm	La	Pr	Pb	Ce	Nd	Ca	Th	U	Eu	Gd	Dy	Er	S	As	Fe	O	Total	Age (Ma)	Age err
1.0	13,24	1,57	0,19	1,66	12	2,34	0,24	25,73	11,46	0,41	2,94	b.d.l	0,13	1,44	0,55	b.d.l	0,01	b.d.l	b.d.l	27,73	101.7	1775	100
2.0	13,2	1,54	0,19	1,65	12,04	2,31	0,24	25,7	11,44	0,42	2,9	b.d.l	0,11	1,41	0,53	b.d.l	0,01	b.d.l	b.d.l	27,64	101.38	1781	101
3.0	13,17	1,53	0,18	1,68	11,99	2,36	0,23	25,79	11,42	0,39	2,75	b.d.l	0,13	1,44	0,56	0,05	0,01	b.d.l	b.d.l	27,58	101.276	1806	105
1.1	13,18	1,57	0,18	1,73	12,06	2,43	0,22	25,96	11,61	0,41	2,69	b.d.l	0,12	1,43	0,54	0,08	0,02	b.d.l	b.d.l	27,71	101.969	1797	108
2.1	13,22	1,52	0,18	1,74	11,92	2,36	0,22	25,84	11,46	0,37	2,61	b.d.l	0,13	1,47	0,53	0	b.d.l9	b.d.l	b.d.l	27,62	101.234	1778	109
3.1	13,22	1,51	0,17	1,71	12,07	2,32	0,2	25,88	11,52	0,35	2,53	b.d.l	0,14	1,44	0,54	0,04	0,01	b.d.l	b.d.l	27,63	101.334	1747	112
1.2	13,19	1,54	0,19	1,67	12,01	2,29	0,24	25,78	11,5	0,41	2,9	b.d.l	0,12	1,4	0,55	0,05	0,01	b.d.l	b.d.l	27,64	101.499	1782	101
2.2	13,15	1,53	0,19	1,67	11,92	2,38	0,25	25,68	11,41	0,43	2,95	b.d.l	0,12	1,42	0,55	0,05	0,01	b.d.l	b.d.l	27,58	101.285	1791	100
3.2	13,16	1,52	0,18	1,7	12	2,31	0,21	25,85	11,49	0,37	2,64	b.d.l	0,13	1,44	0,58	b.d.l	0,01	b.d.l	b.d.l	27,56	101.202	1719	107
1.3	13,23	1,53	0,17	1,73	11,91	2,22	0,2	25,87	11,57	0,36	2,49	b.d.l	0,17	1,51	0,56	b.d.l	0,01	b.d.l	b.d.l	27,62	101.185	1759	113
2.3	13,14	1,56	0,17	1,73	12,07	2,51	0,22	25,99	11,59	0,36	2,58	b.d.l	0,11	1,45	0,59	0,05	0	b.d.l	b.d.l	27,61	101.732	1794	111
3.3	13,15	1,54	0,2	1,68	12,01	2,37	0,25	25,84	11,5	0,41	2,92	b.d.l	0,13	1,42	0,61	b.d.l	0,01	0,03	b.d.l	27,64	101.752	1834	101
1.4	13,27	1,74	0,18	1,77	11,85	2,27	0,21	25,66	11,39	0,35	2,52	b.d.l	0,17	1,58	0,67	0,06	0,02	b.d.l	b.d.l	27,72	101.429	1779	112
2.4	13,18	1,78	0,16	1,79	11,83	2,31	0,18	25,71	11,57	0,38	2,31	b.d.l	0,15	1,58	0,65	0,05	0,01	0,02	b.d.l	27,62	101.32	1680	118
3.4	13,22	1,75	0,17	1,76	11,87	2,34	0,18	25,69	11,51	0,39	2,31	b.d.l	0,14	1,55	0,6	b.d.l	0,02	0,02	b.d.l	27,65	101.203	1690	118
1.5	13,26	1,49	0,16	1,68	12,24	2,27	0,19	26,14	11,6	0,36	2,36	b.d.l	0,15	1,44	0,54	b.d.l	0,01	b.d.l	b.d.l	27,71	101.654	1773	118
2.5	13,2	1,49	0,16	1,68	12,19	2,23	0,2	26,05	11,55	0,41	2,4	b.d.l	0,14	1,47	0,58	b.d.l	b.d.l9	b.d.l	0,13	27,66	101.599	1812	117
3.5	13,24	1,53	0,16	1,69	12,13	2,28	0,2	26	11,53	0,36	2,49	b.d.l	0,14	1,48	0,56	b.d.l	0,01	b.d.l	b.d.l	27,67	101.527	1717	112
1.6	13,26	1,56	0,15	1,72	12,15	2,26	0,2	26,02	11,6	0,35	2,31	b.d.l	0,12	1,54	0,58	0,04	0	b.d.l	b.d.l	27,7	101.576	1825	120
2.6	13,28	1,56	0,15	1,7	12,15	2,23	0,19	26,08	11,55	0,33	2,24	b.d.l	0,15	1,48	0,57	0,05	0,01	b.d.l	b.d.l	27,69	101.431	1810	123
3.6	13,18	1,54	0,15	1,77	12,01	2,25	0,19	25,87	11,5	0,37	2,17	b.d.l	0,16	1,55	0,59	b.d.l	b.d.l9	0,02	b.d.l	27,52	100.867	1873	127

1.7	13,35	1,44	0,17	1,65	12,19	2,19	0,19	26,09	11,39	0,49	2,37	b.d.l	0,15	1,41	0,5	b.d.l	0,01	b.d.l	b.d.l	27,8	101.427	1688	116
2.7	13,24	1,52	0,18	1,67	12,11	2,25	0,21	25,91	11,48	0,46	2,51	b.d.l	0,12	1,46	0,54	b.d.l	0,02	0,04	b.d.l	27,7	101.411	1786	113
3.7	13,01	1,59	0,24	1,79	11,96	2,28	0,13	26,03	11,89	0,59	1,74	b.d.l	0,13	1,52	0,56	b.d.l	0,12	0,03	b.d.l	27,63	101.268	1558	144
1.8	13,11	1,62	0,22	1,79	11,89	2,33	0,12	26,13	11,95	0,55	1,68	b.d.l	0,13	1,5	0,55	b.d.l	0,13	b.d.l	b.d.l	27,76	101.546	1593	148
2.8	12,7	1,37	0,34	1,69	12,23	2,39	0,13	26,34	11,75	0,43	1,77	b.d.l	0,12	1,32	0,45	b.d.l	0,2	0,03	0,46	27,46	101.189	1578	143
3.8	12,88	1,39	0,24	1,77	12,05	2,33	0,12	26,28	12,03	0,42	1,62	b.d.l	0,14	1,4	0,46	b.d.l	0,16	b.d.l	0,11	27,45	100.897	1583	154
1.9	12,88	1,4	0,4	1,71	12	2,24	0,15	26,29	11,84	0,37	2,13	b.d.l	0,17	1,36	0,47	b.d.l	0,24	0,03	b.d.l	27,68	101.407	1564	124
2.9	12,94	1,22	0,38	1,74	12,21	2,27	0,15	26,67	11,88	0,36	2	b.d.l	0,18	1,31	0,43	b.d.l	0,21	0,03	b.d.l	27,72	101.684	1597	131
3.9	13,26	0,97	0,21	1,7	12,46	2,33	0,09	27,12	12,08	0,23	1,36	b.d.l	0,15	1,31	0,35	b.d.l	0,02	b.d.l	b.d.l	27,69	101.374	1465	177
1.10	13,12	0,87	0,14	1,79	12,39	2,29	0,06	27,1	12,13	0,2	0,95	b.d.l	0,14	1,46	0,35	b.d.l	0,03	0,04	0,13	27,41	100.598	1415	241
2.10	13,17	0,88	0,15	1,76	12,51	2,26	0,08	27,09	12,05	0,23	1,06	b.d.l	0,15	1,4	0,33	b.d.l	0,03	b.d.l	b.d.l	27,44	100.615	1577	223
3.10	12,99	0,93	0,15	1,78	12,3	2,27	0,08	26,86	11,99	0,44	1,11	b.d.l	0,16	1,46	0,43	b.d.l	0,03	0,03	b.d.l	27,28	100.313	1592	215
1.11	12,91	1,24	0,33	1,75	12,04	2,42	0,12	26,63	12,17	0,18	1,77	b.d.l	0,13	1,38	0,43	b.d.l	0,15	0,04	0,44	27,66	101.81	1505	143
2.11	13,33	1,01	0,15	1,83	12,39	2,35	0,09	26,94	12,19	0,16	1,27	b.d.l	0,15	1,51	0,43	b.d.l	0,03	0,04	b.d.l	27,73	101.596	1503	189
3.11	13,1	1,55	0,23	1,72	11,98	2,31	0,12	26,08	11,83	0,39	1,77	b.d.l	0,14	1,45	0,52	b.d.l	0,13	0,03	0,05	27,65	101.076	1447	140
1.12	13,02	1,3	0,25	1,76	12,13	2,42	0,11	26,45	11,99	0,41	1,65	b.d.l	0,12	1,41	0,49	b.d.l	0,13	0,03	0,16	27,65	101.464	1453	149

Table 7. Sample 982-4 chemical analyses and calculated single point ages.

5.4.3. The crosscutting granite veins

Zircons in the D9/1083 albitic leucogranite are euhedral and prismatic. Their size varies from 110 to 200 μm in length (Fig. 17). Larger grains have 1:3 width/length ratios whereas it is 1:2 in the smaller grains. In CL imaging, domains of remnant oscillatory zoning (domain 1) can be seen in a darker patchy domain (domain 2). Domain 2 is often fractured. A dark CL domain (domain 3) forms islands of altered zircon in domain 2 along cracks and zircon growth planes. Oscillatory zoning in BSE imaging is observed as slightly brighter regions in domain 2. Domain 3 is much darker and are characterised by a low totals and considerable amounts of non-formula elements (Ca, Al, Fe etc. Table 9).

In order to determine the age of granite crystallization, eight SIMS analyses with the smallest discordance (-0.9 % to 2.2 %) were used (IV). Zircons of sample D9/1083, except for two analyses, have U and Th contents of 928-1735 ppm and 37-170 ppm, respectively, and a Th/U ratio of 0.04-0.14 (IV). The two exceptions have higher thorium (Th 295 and 415 ppm) and lower uranium contents (U 540 and 405 ppm), and Th/U ratios of 0.73 and 0.96 (IV). The dating yielded a concordant age of 1497±7 Ma (Fig. 18a; MSWD=1.8), while an average $^{207}Pb/^{206}Pb$ age of the concordant points is 1495±6 Ma (Fig. 18b; n=8, MSWD=2.4), which is regarded as the magma emplacement age (IV).

The V987/387 zircons are smaller (50-120 μm long) and slightly rounded. They have a width/length ratio of 1:2. Zircons often contain radial cracks and small inclusions of apatite, thorite and quartz (Fig. 19a-c; IV). They appear very dark in CL imaging. None of the studied grains retained primary zoning patterns (Fig. 19). Cores of most of the grains appear very dark in both CL and BSE images (domain 3; Fig. 19d-e; IV). EDS analysis showed that domain 3 has low analytical totals and high concentrations of non-formula elements, as in sample D9/1083. These domains host all the inclusions mentioned earlier (Fig. 19a-c, table 9). The rims are patchy in CL and homogeneous in BSE images (domain 2).

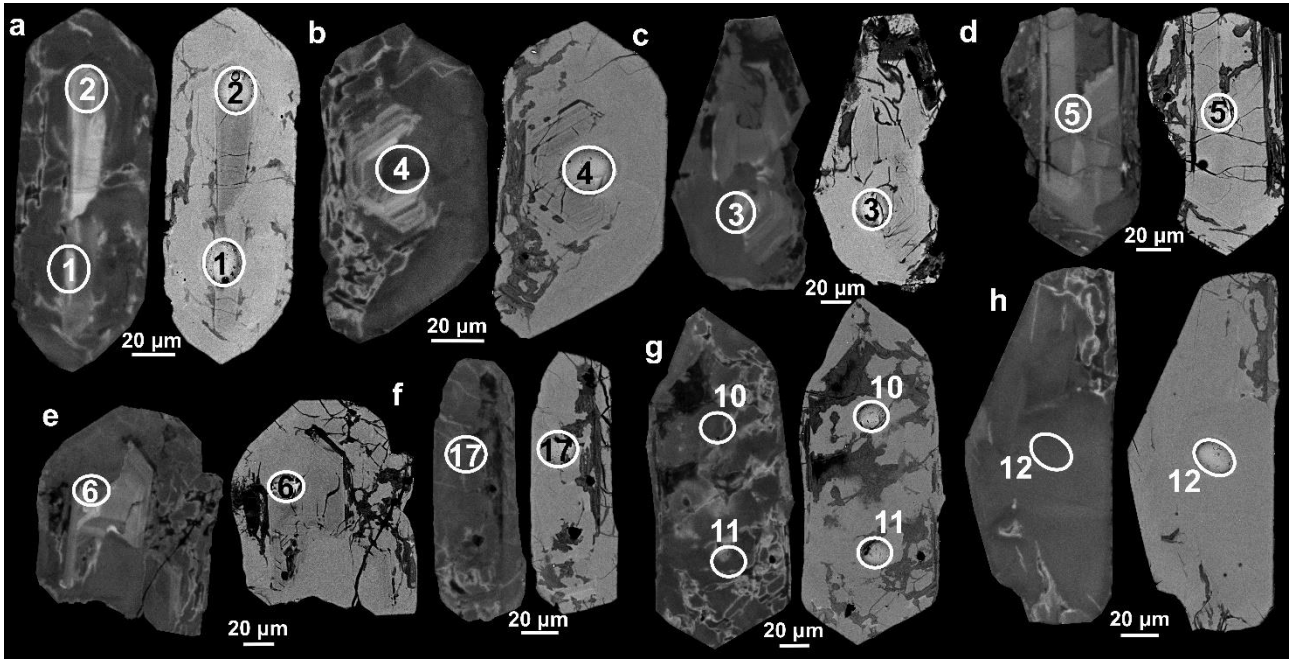

Fig. 17. CL (left) and BSE (right) images of zircons from sample D9/1083. a-e. Zircons with preserved oscillatory zoning. f-h. Zircons with no oscillatory zoning. Note that the domain 3 mainly follow zircon growth zones, where oscillatory zoning is visible and is more random where primary zoning is not preserved.

ID/	[U]	[Th]	[Pb]	Th/U	f_{206}%		±s	Age	±s		±s	Age	±s	Disc.	Disc. %	D_α
	ppm	ppm	ppm	meas		$^{206}Pb/^{238}U$	%	$^{206}Pb/^{238}U$		$^{207}Pb/^{206}Pb$	%	$^{207}Pb/^{206}Pb$		conv.	2s lim.	X 10^{16}
D9-6	1254,0	72,3	380,1	0,06	0,10	0,26687	1,10053	1524,9	15,0	0,093379	0,28	1495,6	5,4	2,2		0,72
D9-3	927,7	81,5	278,2	0,09	0,10	0,26466	0,74040	1513,7	10,0	0,093266	0,24	1493,3	4,5	1,5		0,54
D9-12	1015,8	37,2	295,6	0,04	{0.01}	0,26343	0,75507	1507,4	10,2	0,093777	0,19	1503,6	3,6	0,3		0,58
D9-4	1118,7	170,8	334,1	0,15	{0.01}	0,26207	0,79412	1500,4	10,6	0,093111	0,19	1490,1	3,6	0,8		0,66
D9-5	503,6	294,8	171,5	0,59	0,47	0,26060	0,85130	1492,9	11,4	0,092626	0,36	1480,3	6,9	1,0		0,32
D9-10	1574,5	55,5	452,9	0,04	0,01	0,26051	0,77173	1492,5	10,3	0,093564	0,16	1499,3	3,0	-0,5		0,90
D9-17	1735,3	81,3	502,6	0,05	0,04	0,25955	0,86438	1487,5	11,5	0,092953	0,28	1486,9	5,4	0,0		0,99
D9-2	405,3	414,7	144,4	1,02	0,04	0,25892	0,76348	1484,3	10,1	0,093441	0,31	1496,9	5,8	-0,9		0,24
V-8	1679,1	56,6	452,2	0,03	0,02	0,24406	0,94155	1407,8	11,9	0,092836	0,20	1484,5	3,7	-5,8	-3,7	0,97
V-22	1336,0	57,6	419,2	0,04	0,05	0,28213	3,05588	1602,1	43,5	0,093948	0,64	1507,1	12,1	7,1		0,77
V-2	3433,9	417,7	672,3	0,12	0,13	0,17341	1,35730	1030,9	12,9	0,085398	0,59	1324,6	11,4	-24,0	-20,1	2,02
V-20	5695,1	2177,1	739,3	0,38	0,18	0,11027	1,78550	674,3	11,4	0,068679	1,81	889,1	37,4	-25,4	-12,0	3,54
V-13	7798,4	2019,2	1078,3	0,26	0,98	0,11646	1,11473	710,2	7,5	0,071502	0,66	971,8	13,4	-28,4	-23,6	4,73
V-10	6872,7	3179,3	1177,8	0,46	0,23	0,14225	1,60545	857,4	12,9	0,078718	0,65	1165,0	12,8	-28,2	-23,6	4,33
V-21	2417,0	358,4	467,7	0,15	0,46	0,17381	1,64016	1033,0	15,7	0,086340	0,77	1345,8	14,8	-25,1	-20,3	1,43
V-17	2912,4	944,6	662,2	0,32	0,22	0,19158	2,10997	1129,9	21,9	0,086072	0,78	1339,8	15,0	-17,1	-11,6	1,79

Table 8. Samples D9-1083 and 987-387 (V) zircon dating results and calculated Dα decay events/mg x10^{16} values, calculated according to Murakami et al (1991). Only data used in Terra-Waserburg diagrams are presented.

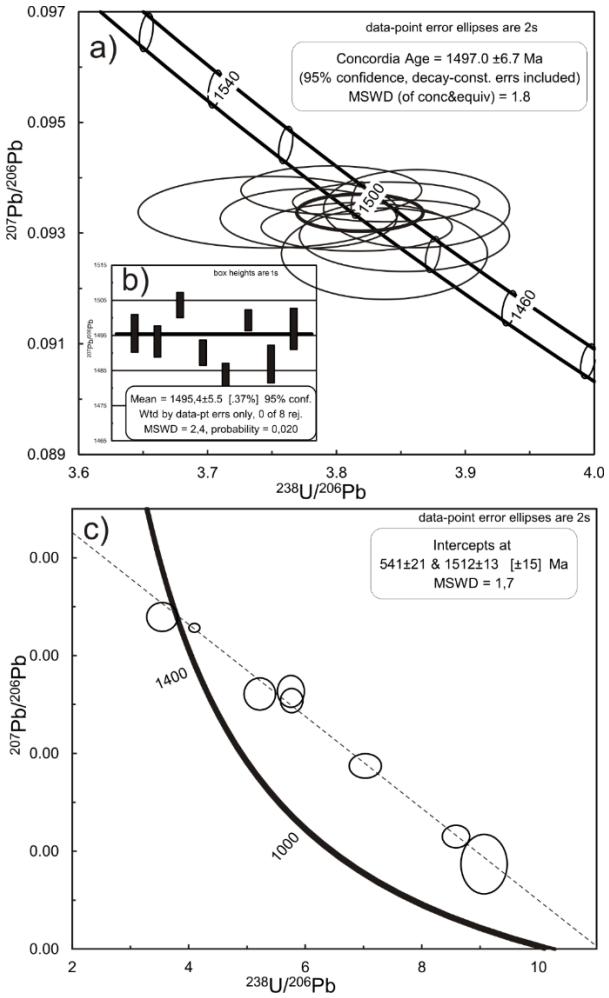

Fig. 18. Zircon dating results of samples D9-1083 a-b) and V987-387 c). a) Tera-Wasserburg diagram of sample D9-1083 showing a concordant age of 1497±7 Ma (MSWD 1.8). b) Pb^{207}/Pb^{206} average age of the same sample yielded 1495±6 Ma (MSWD 2.4). c) Tera-Wasserburg diagram of sample V987-387 intercepting the Concordia at 1512 ±13 Ma (MSWD 2.0) and 541 ±21 Ma.

Twelve analyses were not used in age calculation. Nine analysis have high common lead content (measured Pb^{206}/Pb^{204} 302-1683 and f_{206} 1.11-6.20) and Th/U ratios of 0.19-1.82 (IV). The remaining three analyses have very high U and Th contents (11529-65376 ppm and 36315-166564 ppm, respectively) and high errors (IV). These were discarded on the suspicion that a U and Th-

rich phase was analysed simultaneously. Eight analyses used in age determination are highly discordant (-32.3 % to 7.1 %, average -20.9 %; Table 8; IV). Their Th/U ratio varies from 0.04 to 0.41 (IV). Six of them come from domain 3 and are most discordant. The remaining two analyses are from domain 2 and are inversely discordant and near-concordant (Fig. 19f-g). A Discordia diagram was constructed with the upper intercept at 1512 ±13 Ma (MSWD 2.0) and the lower intercept at 541 ±21 Ma (Fig. 18c). The Pb^{207}/Pb^{206} ages of near-concordant and inversely discordant analyses from domain 2 are 1507±12 Ma and 1484±4 Ma, respectively (IV). The age of the upper intercept is regarded as the age of granitic melt emplacement, whereas the lower intercept age is geologically meaningless.

Time-integrated alpha dose-radiation damage D_α of Murakami et al (1991) was used to evaluate the maximum damage to the crystalline lattice that accumulates with time. U and Th content was used as obtained from the SIMS analyses. The system closure time was used as obtained from the Concordia for D9/1083 sample and the age of the upper intercept for sample V987/387. Nasdala et al (2001) showed that the actual damage in the grain is usually smaller due to the annealing processes. The annealed damage depends on the thermal history of the rock (Nasdala et al., 2001). The D_α of zircons from sample D9/1083 are in the range of 0.24-0.998$\times 10^{16}$ α-decay events /mg. The lowest D_α values are from domain 1, where oscillatory zoning is preserved (spots 2 and 5). Zircone here has the lowest U content (405 and 503, respectively; IV). Sample V987/387 zircons have been damaged more extensively D_α values are in a range of 387 0.775-5.45 $\times 10^{16}$ α-decay events /mg. Highest values were obtained from domain 3 (IV). The two lowest values (spots 8 and 22) are located in the bright CL domain 2, where the Th content is much lower (57 and 58 ppm, respectively; IV). D_α values here are lower by an order of magnitude.

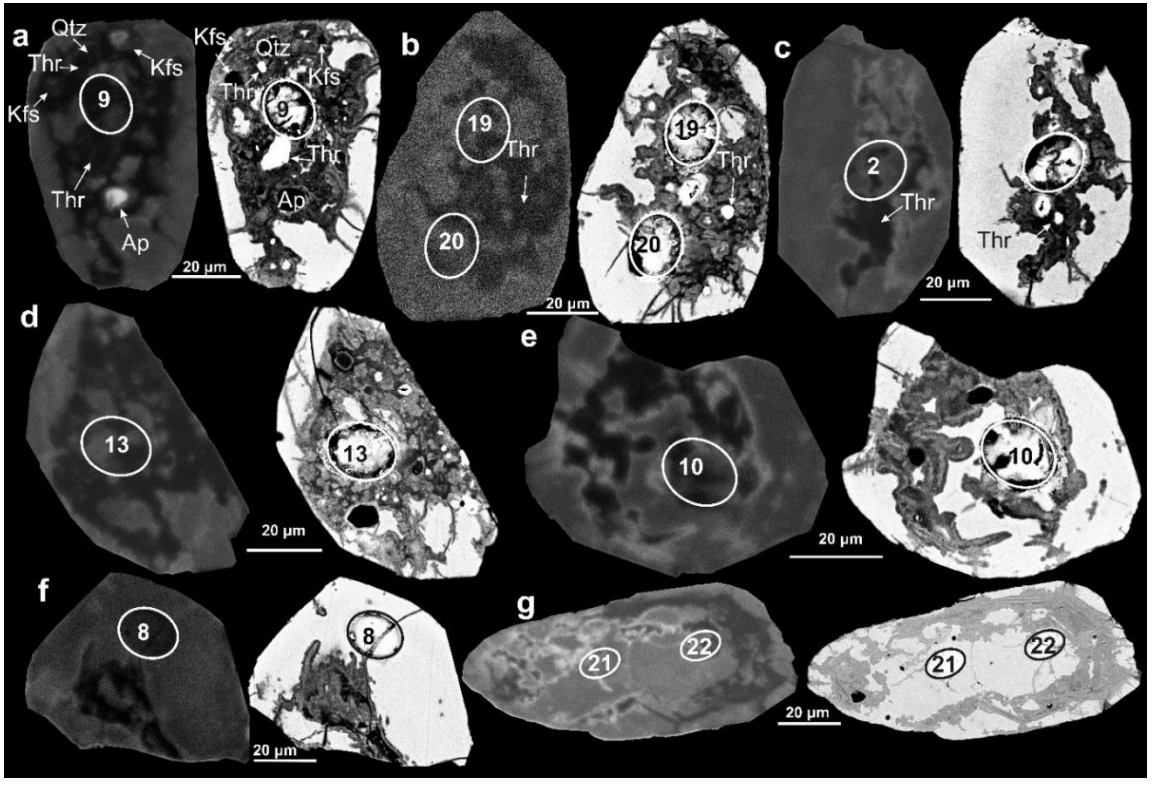

Fig. 19. CL (left) and BSE (right) images of zircons from sample 987/387. a-c. Zircons hosting inclusions of thorite (Thr), quartz (Qtz), K-feldspar (Kfs) and apatite (Ap). d-e. Zircon grains with domain 3 comprising most of the core. f-g. Grains where domain 2 was analysed.

ID	D9-5		V987-20	
	Unaltered	Altered	Unaltered	Altered
ZrO_2	65,66	51,98	65,29	53,45
SiO_2	31,94	27,86	32,12	27,63
HfO_2	1,66	2,59	1,73	1,27
UO_2	0,00	0,81	0,00	0,68
FeO	0,00	0,21	0,00	1,91
MnO	0,00	0,22	0,00	0,63
CaO	0,00	4,82	0,00	2,89
Na_2O	0,00	0,76	0,00	0,74
Total	99,26	89,25	99,14	89,20

Table 9. Representative EDS analyses of D9-1083 and 987-387 zircon unaltered and altered domains

6. DISCUSSION

6.1. Origin of rocks surrounding the VIOD

The trace element patterns of the fine-grained thin layered orthoamphibole-bearing and orthoamphibole-free schists are very similar to those in the primitive lavas of Smith et al (1997). The light rare earth element content, however, is much lower in rocks from the Lz13 drillcore. The Sm-Nd isotopic composition (TDM: 2.08 Ga, ε_{Nd} (1.9 Ga): +0.2; Mansfeld, 1995) shows no or very little crustal component. Sparse and small zircons with no oscillatory zoning patterns yielded an age of 1831±14 Ma. It is interpreted as the age of volcanic activity in the region and formation time of the volcanic precursor. The rocks are enriched in Th and in the Ta/Yb vs. Th/Yb tectonic setting discrimination diagram (Gorton and Schandl, 2000; Pearce, 1983) plot in a subduction-related field. Hence, these rocks probably represent volcanic or volcanoclastic rocks of felsic to intermediate composition, formed in a subduction-related tectonic setting.

The studied rocks have very low alkali content. The calculated alteration index (Lentz 1999) values are comparable to the compositional range of unaltered andesites of Gill (1981). The Lz13 rocks show a clear alteration trend. Hydrothermal seafloor alteration often causes plagioclase dissolution and replacement of primary igneous minerals and glass by chlorite (Peck and Smith, 2005). Another peculiar feature is the low light rare earth element content. Hikov (2013) suggested that LREEs can be extracted from rocks by low pH fluids. If no secondary mineral, incorporating LREE, forms during this process, a significant LREE depletion can occur. It is possible that allanite or another LREE accumulating mineral was destroyed during hydrothermal alteration prior to metamorphism, leading to leaching of the LREEs. A simple mass-balance calculation was performed, adding small amounts of allanite to the bulk chemical composition. A small fraction of allanite (0.03-0.04 %) is sufficient to account for the LREE depletion observed in our samples. The modelled trace element and REE patterns are very similar to those found in primitive island arc lavas (Smith et al., 1997) and sample D9-473. Alteration by infiltration of sea water prior to the regional metamorphism was suspected for tourmaline-bearing gneiss formation further east.

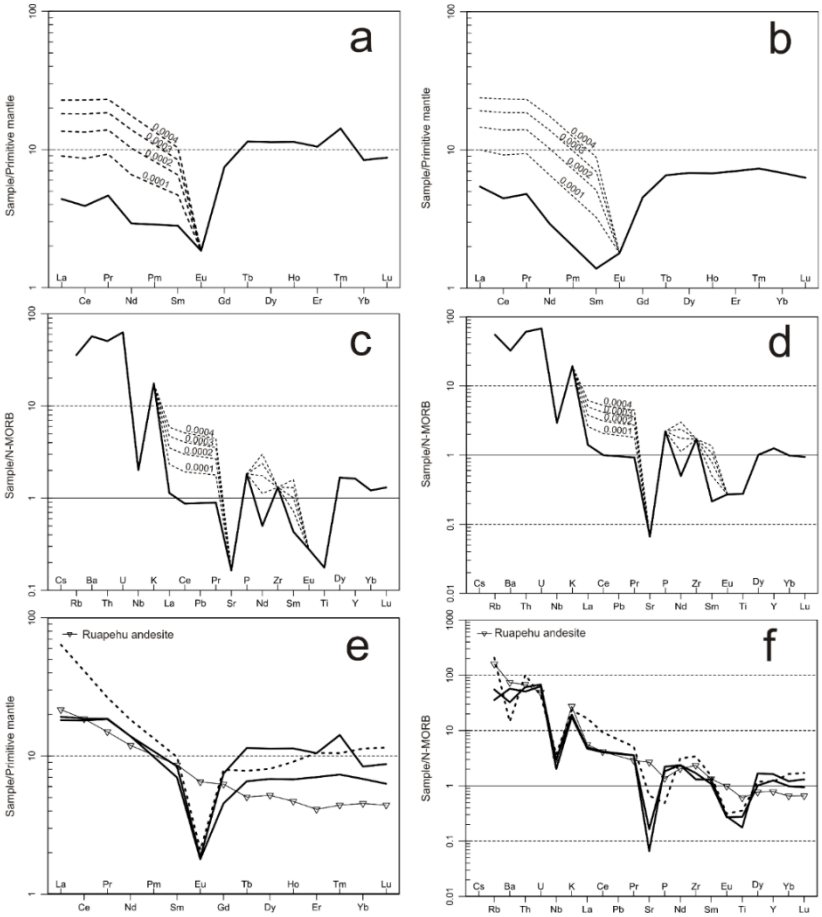

Fig. 20. REE modelling by adding different fractions of allanite to the bulk composition. Dotted lines in a-d show different allanite fractions. Allanite composition used in calculation was taken from unaltered volcanic rocks (Genna et al., 2014). a and b. REE patterns for samples Lz13/509.6 and LZ13/521.8, respectively, normalized to primitive mantle of McDonough and Sun (1995). c-d. Trace element patterns in samples Lz13/509.6 and LZ13/521.8, respectively, normalized to N-MORB (Sun and McDonough, 1989). e-f. REE and trace element patterns in same samples with 0.0003 allanite added. Andesite composition for primitive island arc (Smith et al., 1997) and composition of volcanic rock from sample D9-473 (dashed line) were plotted for comparison.

6.2. Age and evolution of the rocks surrounding the VIOD

The 1.83 Ga Lz13 volcanic rocks were buried to at least 25 km depth (7 kbar), as recorded by garnet core isopleths. The maximum temperature reached at this stage is about 630˚ C. Uplift to 15 km followed the pressure maximum, as recorded by garnet rims at 6-5 kbar and 640˚ C. The decompression may have caused lead loss in zircon that culminated at ca. 1.73 Ga (II). A reheating stage up to 630-640˚ C at 3.5-4.5 kbar was recorded in the Lz13/540 sample skeletal garnet. The small monazite grains found in the cordierite, biotite and quartz matrix, close to the skeletal garnet of the same rock are rich in Th and depleted in HREE and probably grew simultaneously with garnet (Pyle and Spear, 1999; Williams et al., 2007; Zhu and O'Nions, 1999). The LREEs released by major silicate breakdown might result in formation of new monazite grains, while the HREE are largely incorporated in garnet (Kohn and Malloy, 2003). These monazites were dated at ca. 1.50 Ga. The reheating probably was caused by intrusion of granitic melts in the upper crust. A pegmatitic granite vein of unknown age crosscuts the country rocks in this drilling and is assumed to be a part of the ca. 1.5 Ga AMCG complex.

6.3. Evolution and timing of the VIOD rocks and ores

Temperature of 700˚ C at 5-6 kbar pressure (19-22 km depth) can be implied for VIOD rocks, based on appearance of forsterite and spinel (III). In sample 982-9 olivine pseudomorphs are found in a tremolite matrix. Magnetite here hosts inclusions of diopside and tremolite, suggesting that the forsterite forming reaction Di+Do = Cal+Fo took place, giving minimum temperature estimates of 500-600° C, depending on the pressure and X_{CO2} condition at the time (Tracy and Frost, 1991). The upper amphibolite facies conditions (700˚ C; 6 kbar) were implied for the rocks comprising LEL by Bogdanova et al (2006). The maximum temperature did not exceed 700-750˚ C, as obtained from fluid inclusion studies by [a]Skridlaite (1993). This stage took place at 1781±60 Ma, as recorded by the cores of monazite in the same sample (III). A similar temperature of 680˚ C was obtained from calcite in olivine. Calcite is easily reset and probably records a cooling stage after the peak conditions. A drop of pressure and temperature is marked by the appearance of anthophyllite and other amphiboles like tremolite (III). Slightly lower temperatures of 500-600˚ C can be implied from the appearance of

spinel exsolutions in magnetite (Sack and Ghioso, 1991). Local reheating of at least ~550˚ C is indicated by the foam structure of magnetite in some parts of VIOD (Ciobanu and Cook, 2004). Temperature of 590˚ C was recorded by calcite-dolomite thermometry of matrix calcite (982-4). During the reheating, carbonates found in the matrix recrystallized to a polygonal structure. Small monazites and monazite rims of the largest grains in this sample were dated at ca. 1.50 Ga. They probably grew during the emplacement of the granitic melt.

Magnetite in sample D8-1 is in close association with hydrous minerals such as serpentine, iddingsite and phlogopite. Grains in the largest clusters meet at triple junctions, indicating that annealing had occurred (Ciobanu and Cook, 2004). The edges often show signs of dissolution-reprecipitation (Hu et al., 2014). The chemical analyses showed that magnetite has similar amounts of titanium, magnesium and aluminium at the core and rim. However, the vanadium content decreases at the rim. Triple junctions and dissolution-reprecipitation indicate that magnetite has experienced re-equilibration processes at ~550˚ C (Ciobanu and Cook, 2004; Hu et al., 2015). It has been widely accepted that vanadium is relatively immobile (Hu et al., 2015) and can be used as a tracer element (Mathieu, 2019). Another feature observed in D8-1 sample is the formation of oxy-exsolutions. Grain cores host abundant Mg-spinel exsolutions. This implies that the original core composition was richer in Al and Mg than determined and must have formed in the 500-600˚ C temperature range (Sack and Ghioso, 1991).

Sample D8-2 magnetites are very similar to those found in the previous sample. The grains follow phlogopite and serpentine, replacing olivine, grain boundaries and have cores with abundant spinel exsolutions. No distinction in the composition between core and the rim can be made. A rather low aluminium content (0.07-0.08 wt% Al) compared to magnesium (0.15-0.25 wt% Mg) indicates that magnesium is present as magnetite-magnesioferrite ($MgFe_2O_4$) solid-solution. Formation of magnetite with 0.2-3.1 wt% Mg during hydration experiments of forsterite were described by Filippidis (1982). High magnesium content as a result of serpentinization has also been described in natural systems (Friersch, 1985). The grains rarely meet at the triple junctions, and if they do, they always have abundant spinel exsolutions. The rims often host inclusions of chlorite and serpentine. The core-rim boundary, in places resembling stylolite, is marked by rows of tiny serpentine inclusions, indicate episodic growth. Another feature of these magnetites is inclusions of phlogopite. Most phlogopites are at least partly replaced by Mg-rich chlorite. Magnetite released from phlogopite accumulates in larger grains

through Ostwald ripening. Phlogopite probably formed in a late stage. Large phlogopite grains often truncate calcite-pyrite veinlets.

In the tremolitic rock of sample D8-7 pyrrhotite was found. It has a network of fractures and host a few inclusions of olivine. The inclusions indicate sulphide formation during or shortly after the peak metamorphism. However, pyrrhotite is a low-temperature Fe-sulphide, suggesting that it formed as a replacement of pyrite. The transition of pyrite to pyrrhotite was determined over a wide range of temperatures in metasedimentary rocks: 375-575° C (Ferry, 1981) and 200-400° C (Pitcairn et al., 2010). These temperatures are lower than those implied for the reheating stage of VIOD (550° C), suggesting that pyrite-pyrrhotite transition took place before reheating or during the cooling stage. This explains the phlogopite-pyrrhotite intergrowths. Magnetite in the olivine lenses, at the boundary with tremolite rock, closely follows the boundaries of serpentine, replacing olivine. Magnetite shows no signs of triple junctions. Small rims formed around the larger grains due to dissolution-reprecipitation (Hu et al., 2014). Both rims and cores are rich in magnesium and slightly differ in their titanium and aluminium contents, thus it formed as a result of Mg-silicate replacement by serpentine. Inclusions of serpentine and magnesite support this observation. The presence of Ti-Mn-Fe oxides next to low-Ti magnetite and as inclusions in it further indicates magnetite formation at low temperatures. Further in the tremolitic rock, magnetite formation due to the oxidation of pyrrhotite can be seen. No indications that the rock has experienced the reheating step were observed.

Magnetite in the tremolitic rock (sample 982-9) is found only in the most brecciated parts. It is made up of large clusters of varying grain sizes. Magnetite is homogeneous, rich in magnesium, manganese and low in aluminium, titanium and vanadium. Orderly rows of monomineralic and composite inclusions suggest magnetite formation due to replacement of carbonates, during or after the peak metamorphism. Small inclusions of quartz and calcite in the chlorite-like fractures filling material support skarn formation due to the infiltration of silica-bearing fluids in carbonates. The absence of titanium and vanadium in magnetite supports its crystallization as a result of skarn replacement. Magnetite grains at the edge of the largest clusters experienced recrystallization, seen in other samples. However, recrystallization is not pervasive and full textural equilibrium was not attained. The ore is very brecciated in some places. Milling and brecciation of magnetite is a result of the different rheologies of the metamorphic minerals

(Gilligan and Marshall, 1987; Marshall et al., 2000; Vokes, 2000). It was followed by cementation by iddingsite and serpentine.

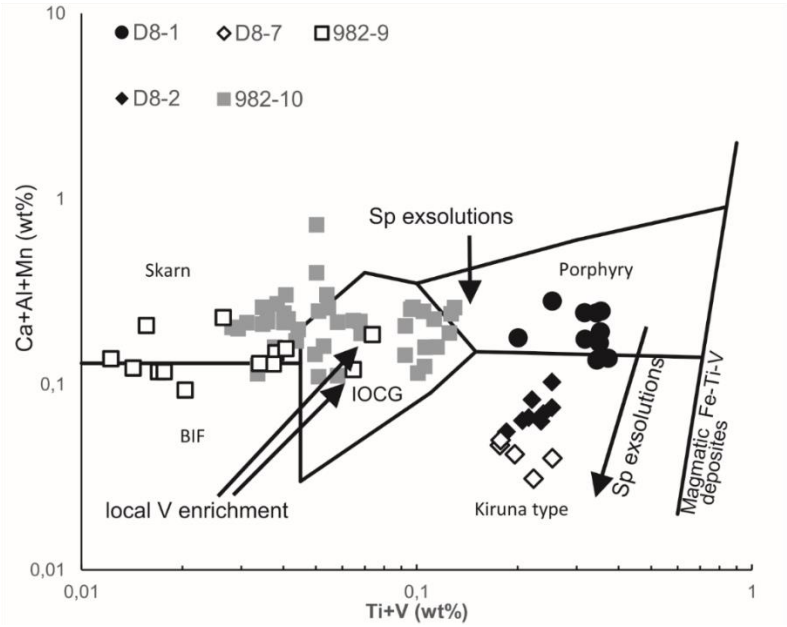

Fig. 21. Ti+V vs Ca+Al+Mn magnetite discrimination diagram (Dupuis and Beaudoin, 2011). Trends for spinel exsolution have been added. Most analyses of sample 982-9 magnetite plot near or in the skarn field, except for a few analyses that have vanadium above the detection limit of EMPA. BIF stands for banded iron formations and IOCG for Iron oxide-copper-gold deposit type.

In sample 982-10 magnetite is scattered throughout the rock in small clusters. They impregnate the serpentine, replacing olivine and are in close association with phlogopite. The largest clusters follow spinel and chlorite, replacing spinel boundaries. Grains here meet at triple junctions. Distinct cores with abundant spinel exsolution in some cases host inclusions of dolomite and spinel, indicating their crystallization during or after the formation of the peak assemblage. The cores are silica-free, rich in magnesium and aluminium. The triple junctions observed throughout the sample indicate that textural equilibrium (~550° C) was attained. The rim is impregnated with serpentine inclusions and show a typical dissolution-reprecipitation pattern

(Hu et al., 2014). It is enriched in silica compared to the cores and probably formed during olivine replacement by serpentine.

In magnetite discrimination diagram (Dupuis and Beaudoin, 2011) our samples form a continuum from the skarn field to porphyry to Kiruna type (Fig. 21). This, together with the observed microstructures, illustrates the effect of oxy-exsolution, dissolution-reprecipitation and recrystallization on the primary magnetite composition (Ciobanu and Cook, 2004; Hu et al., 2015). Slightly higher Ti and V contents in magnetite (samples D8-1, 2 and 7) can also be attributed to a carbonate-volcanic rock mixture, whereas low Ca and higher Mn contents reflect the varying partitioning behaviour of these elements in limestones and dolomites during skarn development (McQueen and Cross,1998). The ca. 1.5 Ga reheating and fluid release may have caused recrystallization in magnetite. The typical foam structure (Hu et al., 2015), intergrowths with olivine and spinel and relative immobility of Ti and V (Dupuis and Beaudoin, 2011; Ray and Webster, 2007; Ciobanu and Cook, 2004) in magnetite suggest that magnetite formed in stages. The elevated magnesium content indicates magnetite formation as a result of Fe-Mg-Si replacement. Magnetite with spinel exsolutions that follows major skarn silicate boundaries formed during the peak metamorphism or shortly after it. The minimal temperature implied from spinel exsolutions is 500-600˚ C (Sack and Ghioso, 1991). After the uplift, reheating took place in some parts of the deposit, causing recrystallization along the boundaries and formation of the triple junction in magnetite. During the reheating, or shortly after it, fluid infiltration remobilised some of the iron, causing dissolution-reprecipitation along the magnetite edges, formation of sulphide veinlets and flakes of magnetite in phlogopites, serpentines and other hydrous minerals. According to PT conditions implied and monazite dating in VIOD, iron mineralization must have taken place between 1.79 and 1.5 Ga.

6.4. Age and emplacement conditions of the granite veins

Most of the dated zircons have a prismatic shape and relicts of oscillatory zoning (sample D9-1083) indicating their magmatic origin (Connelly, 2000; Hoskin, 2000). Relicts of oscillatory zoning can be seen in domains 1 in sample D9-1083 (Fig. 17a-e). The uranium content in zircons, however, is much higher (405-7798 ppm) than in typical igneous zircons (100-500 ppm, Marsellos and Garver, 2010).

The Th/U ratio of zircons is generally greater than 0.1. In sample D9-1083 it varies from 0.04 to 1.02. Some of the lowest values are close to those of metamorphic zircon (Rubatto, 2017). However, no indications of metamorphism, or indeed growth of metamorphic zircon, were observed. This implies that the Th/U ratio in zircons has been altered (Belousova et al., 2002; Grimes et al., 2015). Tiny thorite grains are scattered throughout the sample and their simultaneous crystallization would have lowered the Th/U ratio in the melt. Th mobility in zircon also can be facilitated by low temperature hydrothermal alteration (Geisler et al., 2007). Domain 3, where the highest discordancy (-28.4 to -17.1) is observed, is distributed along fractures and growth planes in D9-1083 zircons and comprises most of the V987-387 zircons. They typically have low analytical totals and host inclusions of other phases (thorite, apatite, K-feldspar and quartz), indicative of dissolution-reprecipitation growth and alteration (Geisler et al., 2007; Rubatto, 2017). According to Geisler et al (2007), if during such zircon alteration high-U or -Th zircon is approaching eutectics with the fluid, new low-U or -Th zircon and U or Th-rich phase will form. Although no such newly formed zircon has been observed in our samples, thorite nucleation during zircon alteration would lower Th/U ratio significantly.

The time-integrated alpha dose-radiation damage D_α of Murakami et al (1991) for sample D9-1083 is in the range 0.24-0.998× 1016 α-decay events /mg and 0.775-5.45 × 1016 × 1016 α-decay events /mg for sample V987-387. It shows that D9-1083 zircons have experienced low to moderate damage, whereas V987-387 zircons are damaged very strongly. The latter can be interpreted as fully metamict (Murakami et al., 1991), if no annealing had occurred (Ewing et al., 2003). The D_α shows that due to the radiation damage, low density and higher molar volume amorphous zircon must have formed (Garver and Kamp, 2002; Murakami et al., 1991). This would have caused a heterogeneous expansion and opening of fluid pathways (Nasdala et al., 2009), enabling the alteration process described above.

Zircon from D9-1083 albite leucogranite yielded a Concordant age of 1497±7 Ma (Fig. 18a). The average Pb^{207}/Pb^{206} age of 1495±6 Ma (Fig. 18b) is within the errors of the concordant age and represents the timing of albite leucogranite emplacement in the crust. Zircons from sample V987-387 are very discordant and only two points plot close to the upper intercept of 1512 ±13 Ma (MSWD 2.0). The two near-concordant points have Pb^{207}/Pb^{206} ages of 1507±12 Ma and 1484±4 Ma. The rest data conform to the trendline that meets the Concordia at 541 ±21 Ma (Fig. 18c). The upper intercept is regarded

as the age of syenitic granite emplacement. The time-integrated alpha dose-radiation damage D_α of Murakami et al. (1991) values in sample V987-387 shows a correlation with discordance observed in the Tera-Wasserburg diagram (Table 8). Cherniak and Watson (2000) and Cherniak (2010) showed that lead mobility is much faster in radiation damaged zircon, causing discordancy (Nasdala et al., 1998; Xu et al., 2012; Cherniak and Watson, 2000; Cherniak, 2010). The highly damaged zircons from V987-387 syenitic granite have either experienced lead loss via amorphous or low crystallinity domains in response to geological events (Utsunomiya et al., 2004), or an episodic lead leaching during zircon interaction with aqueous fluid (Silver and Deutsch, 1963).

The emplacement time of both granites is very similar to the age of the AMCG Mazury complex in the south (Morgan et al., 2000; Dörr et al., 2002; Ruszkovski et al., 2018; Skridlaitė et al., 2003; Skridlaitė et al., 2008; Sundblad et al., 1994).

The dated albite leucogranite and syenitic granite both have a low temperature eutectic assemblage of quartz, albite and K-feldspar. In both rocks mafic minerals are very scarce. The felsic minerals often meet at triple junctions, indicating a low-temperature eutectic assemblage. Presence of high-U and/or -Th zircons in felsic magmas show that they were extremely fractionated, late stage liquids (Wang et al., 2016). The zircon saturation temperatures (Watson and Harrison, 1983) of 728˚ C (M 1.45) and 763˚ C in samples D9/1083 and V987/387, respectively, provides the minimum temperature at which the granitic melt could have segregated (Miller et al., 2003). Pressure conditions of less than 2.5 kbar can be assumed for D9/1083 granite (Gualda and Ghiorso, 2013). The pressure estimate based on the normative quartz, albite and K-feldspar content (Yang, 2017) showed that D9/1083 crystallized at a pressure of 1 kbar. This indicates granitic melt emplacement in the upper crust at shallow depths, where heat can be diffused rapidly. The studied iron ores are more than 200 m away from the granites; thus, the effect of lower temperatures is observed there. The same thermal reworking was reported previously, implied from hornblende $^{40}Ar/^{39}Ar$ cooling ages of 1.55-1.45 Ga (Bogdanova et al., 2001; Skridlaite et al., 2006).

6.5. Regional context

The age of emplacement of volcanic rocks from the Lz13 drilling is very similar to the estimated age of WLG domain to the west and its continuation

into Poland (Claesson, 1996; Krzeminska et al., 2005, 2007; Wiszniewska et al., 2007). A single zircon grain dating of metavolcanics rock from the D9 drilling (473 m depth) yielded a similar age of 1843±9 Ma. Igneous rocks have been dated in the vicinity, but they tend to be older. The ca. 1.86-1.84 Ga MLD (Bogdanova et al., 2015; Motuza, 2005; Motuza et al., 2008; Rimsa et al., 2001; Skridlaite et al., 2011, 2012, 2014, Vejelyte, 2011) and the ca. 1.89-1.87 Ga LEL (Mansfeld, 2001; Bogdanova et al, 2015; Šiliauskas et al., 2018) to the west and east, respectively. Rocks from MLD are of similar age, but they have active continental margin characteristics, whereas rocks from Lz13 have formed in an island arc tectonic setting and probably were deposited in a back-arc basin environment. The modelled REE and trace element patterns are very similar to those formed in primitive arcs and share similarities with the D9-473 metavolcanics of similar age. Sm-Nd isotopic composition of the rocks from Lz13 drilling indicates juvenile source (TDM 2.08 Ga, εNd(1.9 Ga) +1.8; Mansfeld, 1995). Metamorphic reworking at ca. 1.79-1.73 Ga is recorded in the rocks. A gabbro of similar age of ca. 1.79 Ga has intruded the country rocks at the time of the Sarmatia-Fennoscandia collision (Skridlaite et al, 2011; Bogdanova et al., 2015), followed by ca.1.71-1.66 Ga shearing and metamorphism (Bogdanova et al., 2001). A younger monazite age was recorded in ca. 1.89 Ga volcanic rocks (Šiliauskas et al., 2018) at 598.8 m depth: 1671±57 Ma (unpublished). A metamorphic overprint at ca.1.73-1.68 Ga has also been recorded in the WLG (Skridlaite et al., 2014).

The ca. 1.5 Ga event manifests itself in all the rocks studied. Monazite dating in Lz13/540 and V982-4 yielded metamorphic ages of 1473±30 (II) Ma and 1536±82 Ma (III), respectively, while the D9/1083 and 987/387 granite emplacement age, determined by zircon dating, is 1495±6 Ma and 1512 ±13 Ma (IV). Similar monazite overgrowth ages were recorded in ca. 1.89 Ga volcanic rocks (Šiliauskas et al., 2018) at 598.8 m depth: 1515±31 Ma (unpublished). The obtained age estimates are within the range (1.48-1.56 Ga) of the emplacement of the voluminous Mazury AMCG complex and Kabeliai granites (Morgan et al., 2000; Dörr et al., 2002; Skridlaitė et al., 2003; Skridlaitė et al., 2008; Sundblad et al., 1994). It was followed by local melting of the crust to the west of the Mazury complex that produced peraluminous S-type granite veins and pegmatites (Ruszkowski et al., 2018). Simultaneously, intracratonic extension and accretionary events took place further west (Bogdanova et al., 2008; Brander and Söderlund, 2007; Brander et al., 2012). A metamorphic overprint of the same age has been recorded in southern Lithuania and northern Poland by U-Pb zircon, monazite and $^{40}Ar/^{39}Ar$

hornblende dating (Bogdanova et al., 2001; Skridlaite et al., 2006, 2008, 2014).

6.6. Implications for ore sources for the Varėna Iron Ore deposit

The formation of the VIOD hosting rocks as was implied from zircon ages proceeded between ca. 1.89 Ga and ca. 1.83 Ga. Ore formation processes can be restricted to the time interval of ca. 1.79-1.5 Ga, as was recorded by metamorphic overprint of the host rocks and intrusions of granitic veins. However, the estimated amount of iron ore is so voluminous that and additional source of Fe was required. One of the possible sources can be thinly layered rocks with bands of magnetite, resembling BIF (banded iron formations) occurring just to the north of the VIOD, in the 410 drilling. Their age is unknown but given the formation of major tectonic units in Lithuania (Bogdanova et al., 2015), an age of 1.90-1.83 Ga can be implied. Though major BIF formation elsewhere took place at 2.5-1.9 Ga (James, 1983), occurrences of banded iron formations as young as 1.82-1.77 Ga have also been reported (Anderson and Silver, 1976; Bayley and James, 1973). Another possibility can be the ca. 1.79 Ga (Skridlaite et al, 2011; Bogdanova et al., 2015) Roduka gabbroic intrusions containing iron ore. Further south, the voluminous AMCG Mazury complex of ca. 1.5 Ga hosts magmatic Fe-Ti-V deposits, where occurrences of PGE and REE minerals in dispersed Fe-Cu-Co-Ni sulphide mineralization were reported (Wiszniewska et al., 2018; Wiszniewska et al., 2019). Similar sulphide associations were observed in the D8-7 sample. Some occurrences of REE mineralization in the VIOD were mentioned by Motuza and Kirkliauskaitė (2016). In places where the Mazury complex has experienced hydrothermal alteration due to the emplacement of late stage pegmatitic and aplitic granites of ca. 1.49-1.48 Ga, telluride minerals were reported (Wiszniewska et al., 2018; Wiszniewska et al., 2019). Occurrences of small bismuth and lead tellurides were recorded in the VIOD and neighbouring Lz13 rocks, though no PGE minerals were found. The thermal reworking and emplacement of late stage granites in the VIOD is contemporaneous with the formation of the Mazury AMCG complex. Its formation may be responsible for transportation and remobilization of iron in the VIOD vicinity.

7. CONCLUSIONS

The Lz13 volcanic complex was formed at ca. 1.83 Ga in an island arc and/or back-arc tectonic setting. It displays strong indications of hydrothermal alteration, such as the destruction of plagioclase and LREE-rich phases, leaching the rocks of Ca, Na, K and LREEs. The alteration must have happened prior to the metamorphism.

Both the Lz13 volcanic and VIOD volcanic-sedimentary complexes overlie ca. 1.89 Ga metaigneous rocks. A U-Pb zircon age of 1843±9 Ma from the VIOD metavolcanic rock (D9 drillcore, 473 m) overlaps with the Lz13 age of 1.83 Ga (Lz13/521.8). It seems that the VIOD and Lz13 complexes were formed in the ca. 1.83 Ga back-arcs along the ca. 1.86-1.84 Ga continental margin.

The Lz13 and VIOD rocks were subjected to upper amphibolite facies metamorphism at 1.73 Ga and 1.79 Ga and experienced a reheating event at 1.50 Ga as recorded by zircon and monazite ages.

In the VIOD, magnetite ore formation was complex, proceeded in several stages between 1.79 and 1.50 Ga.

The newly dated ca. 1.50 Ga granitoids in the VIOD indicate an extension of the 1.54 - 1.50 Ga AMCG Mazury complex further north. Those late stage granitoids in the VIOD may have been responsible for re-mobilization of iron and for the occurrences of sulphide mineralization, further increasing its economic potential.

The 1.79-1.73 Ga events may be related to the metamorphic overprint and deformation at 1.75-1.70 Ga that followed the collision of Fennoscandia and Sarmatia. The ca. 1.50 Ga reheating coincides with the emplacement of the AMCG Mazury complex and reheating of the host rocks.

ACKNOWLEDGMENTS

The research was partly funded by Nature Research Centre doctoral study funds. I am also thankful for the Open Access Centre facility, for granting me access to the scanning electron microscope Quanta 250.

Zircon dating was possible because of the SYNTHESYS 3 support (project SE-TAF-7040), the grant agreement number is 312253. I am very grateful to professor Martin Whitehouse for the opportunity to visit the NORDSIM facility, Swedish Museum of Natural History and for support during my studies. I also really appreciate the guidance and assistance of Lev Iliynsky, Kerstin Linden and the rest of the NORDSIM staff who made sure the samples were well prepared, introduced me to the SIMS dating technique and provided all the help needed to get representative data.

I am very grateful for the assistance and aid of professor Boguslaw Baginski, head of the Institute of Geochemistry, Mineralogy and Petrology at Warsaw University, who granted us access to the EPMA facilities. I also would like to thank to doctor Petras Jokubauskas and Lidia Jezak for all the help at the facility during monazite and magnetite analysis.

I am very grateful for the reviewers prof. Raymond Macdonald and prof. Janina Wiszniewska for their comments and suggestions that improved the quality of the thesis.

Most of all I would like to thank my supervisor doctor Gražina Skridlaitė for all the constructive criticism, advice and support through the years. I have learned a lot from you and am humbled by your patience.

Lastly, big thanks to my family and friends for their support and understanding.

REFERENCES

Anderson, C.A. and Silver, L.T., 1976. Yavapai Series – a greenstone belt. Ariz. Geol. Soc. Digest, 10, 13-25.

Anovitz, L.M. and Essene, E.J., 1987. Phase Equilibria in the System $CaCO_3$-$MgCO_3FeCO_3$*. Journal of Petrology, 28(2), 389-414.

Barker, S.J., Wilson, C.J.N., Baker, J.A., Millet, M.A., Rotella, M.D., Wright, I.C. and Wysocczanski, R.J., 2013. Geochemistry and petrogenesis of silicic magmas in the intra-oceanic Kermadec arc. Journal of Petrology, 54 (2), 351-391.

Bayley, R.W. and James, H.L., 1973. Precamrian iron-formations of the United States. Economical Geology, 68, 934-959.

Belousova, E., Griffin, W., O'Reilly, Y.Y., Fisher, N., 2002. Igneous zircon: trace element composition as an indicator of source rock type. Contributions to Mineralogy and Petrology, 143, 602-622.

Breiter, K., Lamarãu, C.N., Borges, R.M.K., Dall'Agnol, R., 2014. Chemical characteristics of zircon from A-type granites and comparison to zircon of S-type granites. Lithos, 192-195, 208-225.

Bogdanova, S.V., Bingen, B., Gorbatchev, R., Kheraskova, T.N., Kozlov, V.I., Puchkov, V.N., Volozh, Y.A., 2008. The east European Craton (Baltica) before and during the assembly of Rodinia. Precamgrian Research, 160(1-2), 23-45.

Bogdanova, S., Gorbatchev, R., Grad, M., Janik, T., Guterch, A., Kozlovskaya, E., Motuza, G., Skridlaite, G., Starostenko, V., Taran, L., & Eurobridge and Polonaise working groups., 2006. EUROBRIDGE: new insight into the geodynamic evolution of the East European Craton. European Lithosphere Dynamics. Eds: Gee, D.G. and Stephenson, R.A. Geological Society, London, Memoirs, 32, 599-625.

Bogdanova, S., Gorbatchev, R., Skridlaite, G., Soesoo, A., Taran, L., Kurlovich, D., 2015. Trans-Baltic Palaeoproterozoic correlations towards the reconstruction of supercontinent Columbia/Nuna. Precambrian Research, 259, 5-33.

Bogdanova, S., Page, L.M., Skridlaite, G., Taran, L.N., 2001. Proterozoic tectonothermal history in the western part of the East European Craton: $^{40}Ar/^{39}Ar$ geochronological constraints. Tectonophysics, 339, 39-66.

Brander, L., Söderlund, U., 2007. 1.47-1.44 Ga intra-continental magmatism in the Fenoscandian Shield – a manifestation of the Danopolonian Orogeny? In: Bleeker, W., Sylvester, P. (Eds.), The Pulse of the Earth &

Planetary Evolution: Rates and Rhythms: Cycles and Cataclysms, GAC NUNA Conference, Sudbury, 13-17 June, 2007, p. 18.

Brander, L., Appeluist, K., Cornell, D., Andersson, U.B., 2012. Igneous and metamorphic geochronologic evolution of granitoids in the central Eastern Segment, southern Sweden. International Geology Reviews, 54, 509-546.

de Capitani and C., Brown, T.H., 1987. The computation of chemical equilibrium in complex systems containing non-ideal solutions. Geochimica et Cosmochimica Acta 51, 2639-2652.

de Capitani, C., Petrakakis, K., 2010. The computation of equilibrium assemblage diagrams with Theriak/Domino software. American Minerologist, 95, 1006-1016.

Cherniak, D.J., 2010. Diffusion in accessory minerals: zircon, titanite, apatite, monazite and xenotime. Reviews in Mineralogy and Geochemistry, 72: 827-869.

Cherniak, D.J., Watson, E.B., 2000. Pb diffusion in zircon. Chemical Geology, 172: 5-24.

Ciobanu, C.L., Cook, N.J., 2004. Skarn textures and a case study: the Ocna de Fier-Dognecea orefield, Banat, Romania. Ore geology Reviews, 24, 315-370.

Claesson, S., 1996. U-Pb age determinations from the Precambrian of Lithuania and Poland. Fourth EUROBRIDGE Workshop. Lund University, Oskarshamn, Sweden, p. 11.

Claesson, S., Bogdanova, S.V, Bibikova, E.V., Gorbatschev, R., 2001. Isotopic evidence of Paleoproterozoic accretion in the basement of the East European Craton. Tectonophysics, 339, 1-18.

Connelly, J.N., 2000. Degree of preservation of igneous zonation in zircon as a signpost for concordancy in U/Pb geochronology. Chemical Geology 172: 25-39.

Dörr, W., Belka, Z., Marheine, D., Schastok, J., Valverde-Vaquero, P., Wiszniewska, J., 2002. U-Pb and Ar-Ar geochronology of anorogenic granite magmatism of the Mazury Complex, NE Poland. Precambrian research, 119: 101-120.

Dupuis, C., Beaudoin, G., 2011. Discriminant diagrams for iron oxide trace element fingerprinting of mineral deposit types. Mineral Deposita, 46, 319-335.

EUROBRIDGE Seismic Working Group., 1999. Fenoscandia-Sarmatia suture of the East Seismic velocity structure across the European Craton

beneath the EUROBRIDGE profile through Lithuania and Belarus. Tectonophysics, 314. 193-217.

Ewing, R.C., Meldrum, A., Wang, L., Weber, W.J., Corrales, L.R., 2003. Radiation effects in zircon. In: Hanchar, J.M., Hoskin, P.W.O. (eds.), Zircon. Reviews in Mineralogy and Geochemistry, 53: 378-420.

Filippidis, A., 1982. Experimental study on the serpentinization of Mg-Fe-Ni olivine in the presence of sulfur. University of Uppsala, Department of Mineralogy and Petrology, research report 27, 1-2.

Frietsch, R., 1985. Formation of Mg-bearing magnetite and serpentine in skarn iron ores in northern Sweden. GFF, 3, 219-230.

Gailius, R., 1985. Marcinkonių ploto granitinių uolienų genezė ir koreliacija. LTSR aukšt. M-lų mokslo darbai. Geologija, 6, 3-15 (Resume).

Gailius, R., Grigelis, A., Jankauskas, T., Juodkazis, V., Juozapavičius, G., Kadūnas, V., Katinas, V., Klimas, A.A., Kondratas, A., Kondratienė, O., Linčius, A., Mikalauskas, V., Narbutas, V., Paškevičius, J., Sakalauskas, K., Suveizdis, P., Tarvydas, R. and Vonsavičius, V., 1994. Lietuvos Geologija. Monography. Vilnius, Lithuania, 20-35; 303-307 (in Lithuanian).

Gale, A., Dalton, C.A., Langmuir, C.H., Su, Y., Schilling, J.G., 2013. The mean composition of ocean ridge basalts. Geochemistry, Geophysics, Geosystems 14, 489-518.

Garver, J.I. and Kamp, P.J.J., 2002. Integration of zircon color and zircon fission-track zonation patterns in orogenic belts: application to the Southern Alps, New Zealand. Tectonophysics, 349: 203-219.

Geisler, T., Schaltegger, U., Tomaschek, F., 2007. Re-equilibration of zircon in aqueous fluids and melts. Elements, 3: 41-50.

Genna, D., Gaboury, D. and Roy, G., 2014. Evolution of a volcanogenic hydrothermal system recorded by the behaviour of LREE and Eu: case study of the key tuffite at Bracemac-McLeod deposit, Matagami, Canada. Ore Reviews, 63, 160-177.

Gilligan, L.B., Marshall, B., 1987. Textural evidence of remobilization in metamorphic environments. Ore Geology Reviews 2, 205-230.

Grambling, J. A., 1990. Internally consistent geothermometry and H_2O barometry in metamorphic rocks: the example garnet-chlorite-quartz. Contributions to Mineralogy and Petrology, 105, 617-628.

Gorton, M.P. and Schandl, E.S., 2000. From continents to island arcs: a geochemical index of tectonic setting for arc-related and within-plate felsic to intermediate volcanic rocks. Canadian Mineralogist 38, 1065-1073.

Grimes, C.B., Wooden, J.L., Cheadle, M.J., John, B.E., 2015. “Fingerprinting” tectono-magmatic provenance using trace elements in igneous zircon. Conrtibutions to Mineralogy and Petrology, 170, 1-26.

Gualda, A.R. and Ghiorso, M.S., 2013. Low-Pressure Origin of High-Silica Rhyolites and Granites. The Journal of Geology, 121, 537-545.

James, H.L., 1983. Distribution of Banded Iron-Formation in Space and Time. Developments in Precambrian Geology, 471-490.

Hajash, A., Chandler, G.W., 1981. An experimental investigation of high-temperature interactions between seawater and rhyolite, andesite, basalt and peridotite. Contributions to Mineralogy and Petrology 78: 240-254.

Hikov, A., 2013. Geochemistry of hydrothermally altered rocks from the Asarel porphyry copper deposit, Central Srednogorie. Geologica Balcanica 42; 1-3.

Holland, T.J.B., Baker, J.M., Powell, R., 1998. Mixing properties and activity- composition relationships of chlorites in the system MgO-FeO-Al2O3-SiO2-H2O. European Journal of Mineralogy 10, 395-406.

Holland, T.J.B., Powell, R., 1998. An internally consistent thermodynamic dataset for phases of petrological interest. Journal of Metamorphic Geology 16, 309-343.

Holland, T.J.B., Powell, R., 2003. Activity-composition relations for phases in petrological calculations: an asymmetric multicomponent formulation. Contributions to Mineralogy and Petrology 145, 492-501.

Holdaway, M.J., 2000: Application of new experimental and garnet Margules data to the garnet-biotite geothermometer. American Mineralogist 85, 881-892.

Holland, T.J.B. and Powell, R., 1998: An internally consistent thermodynamic dataset for phases of petrological interest. Journal of Metamorphic Geology 16, 309-343.

Hoskin, P.W.O., 2000. Patterns of chaos: fractal statistics and the oscillatory chemistry of zircons. Geochimica et Cosmochimica Acta 64: 1905-1923.

Hu, H., Lentz, D., Li, J.W., McCarron, T., Zhao, X.F., and Hall, D., 2015, Reequilibration processes in magnetite from Iron Skarn deposits, Economic Geology v. 110, p. 1-8.

Hu, H., Li, J.L., Lentz, D., Ren, Z., Zhao, X.F., Deng, X.D., Hall, D., 2014, Dissolution-reprecipitation process of magnetite from Chengchao iron deposit: Insights into ore genesis and implication for in-situ chemical analysis of magnetite, Ore Geology Reviews, v.57, p. 393-405.

Hughes, R.D. (PhD thesis), 1999. The timescale of andesite generation at Mount Ruapehu, New Zeland. The Open University, 253-255.

Kepežinskas, K., Šliaupa, S., 1994. Varėna iron ore deposit – the part of layered magmatic chamber. In: Kadūnas, V.(ed.), Problems of bedrock research, utilization and protection in Lithuania. Geologijos institutas, Vilnius, 58-59 [In Lithuanian].

Клейн, В.М., Пуура, В.А., Биркис, А.П., Копелмаа, Х.Ю., Мотуза, Г.Б., Скридлайте, Г.В., 1990. Метаморфизм докембрийских комплексов Прибалтики. Кн. Геоло-гия и геохронология докембрияВосточно-Европей-ской платформы,Сборник научных трудов, Наука, Ленинградское отд-ние, 146–154.

Kirkliauskaite, V., Motuza, G., Skipityte, R., 2016. Varėna Suite in the Crystalline Crust of the Southern Lithuania: Implications to the Genesis and Mineralization. Geophysical Research Abstract in EGU General Assembly 2016. EGU2016-17891.

Kohn, M. J. and Malloy, M.A., 2003. Formation of monazite via prograde metamorphic reactions among silicates: implications for age determinations. Geochimica et Cosmochimica Acta, 68, 101-133.

Krzeminska, E., Lukawska, A., Baginski, B., 2019. U-Pb zircon geochronology of high-grade charnockites – exploration of pre-Mesoproterozoic crust in the Mazury Complex area. Acta Geologica Polonica, 69. DOI: 10.24425/agp.2019.126445

Krzeminska, E., Williams, I., Wiszniewska, J., 2005. A Late Paleoproterozoic (1.80 Ga) subduction-related mafic igneous suite from Lomza, NE Poland. Terra Nova, 17(5), 442-449.

Krzeminska, E., Wiszniewska, J., Skridlaite, G., Williams, I.S., 2009. Late Svecofenian sedimentary basin in the crystalline basement of NE Poland and adjacent area of Lithuania: ages, major sources of detritus and correlations. Geological Quarterly, 53, 255-272.

Krzeminska, E., Wiszniewska, J., Williams, I.S., Dörr, W., 2007. Late Paleoproterozoic arc-related granites from the Mazowsze domain, NE Poland In: Kozlowski, W., Wiszniewska, J. (Eds.), Granitoids in Poland, AM Monograph No. 1. Warsaw, Poland, 41-56.

Leake, B., Woolley, A.R., Arps, C.E.S., Birch, W., Gilbert, M.C., Grice, J.D., Hawthorne, F.C., Kato, A., Kisch, H.J., Krivovichev, V.G., Linthout, K., Laird, J., Mandarino, J.A., Maresch, W., Nickel, E.H., Rock, N.M.S., Schumacher., J.C., Smith, D.C., Stephenson, N.C.N., Ungaretti, L., Whittaker, E.J.W., Youzhi, G., 1997. Nomenclature of amphiboles: report of the

subcommittee on amphiboles of the international mineralogical association, commission on new minerals and mineral names. Canadian mineralogist 35, 219-246.

Lentz, D.R., 1999. Petrology, geochemistry, and oxygen isotope interpretation of felsic volcanic and related host rocks hosting the Bruncwick 6 and 12 massive sulfide deposits (Brunswick belt), Bathurst mining camp, New Brunswick, Canada. Economical Geology 94, 57-86.

Ludwig, K.R., 2012: Isoplot 3.75. A Geochronological toolkit for Microsoft Excel. Berkeley Geochronology Center, Spec. Pub. 5, http://dx.doi.org/10.1016/S0016-7037(98)00059-3

Mansfeld, J., (PhD thesis) 1995. Crustal evolution in the southeastern part of the Fenoscandian Shield. Stockholm University, Stockholm, Sweden, 128 pp.

Mansfeld, J. 2001., Age and εNd constrains on the Paleoproterozoic tectonic evolution in the Baltic-Sea region. Tectonophysics, 339, 135-155.

Marfin, S.S., Zvykas, A.B., Korabliova, L.A., 1988. Otchet o rezultatakh geologo-geophyzycheskih rabot s cek'yu ocenki prognoznykh resursov severo-zapadnogo sklona Belorusko-Mazurskoy anteklizi na teritoriyi Litovskoy SSR na zheleznye rudy, provedennykh v 1982-1988 g. g. (Varenskaya ploschad'), Geolfond, GGSL, Vilnius.

Marfinas, S., 1996. Report of the Varena Iron Ore deposit investigations for exploration purposes. Geology of the Varena ore-bearing area and iron ore deposit. V 2, Vilnius, Archive of the Lithuanian geological Survey [In Lithuanian].

Marfinas, S., 1998. Report of additional investigations in south Lithuania at scale of 1:200 000 in 1990-1992 (Dzūkija area). V 1, Vilnius, Archive of the Lithuanian Geological Survey [In Lithuanian].

Marsellos, A.E., Garver, J.I., 2010. Radiation damage and uranium concentration in zircon as assessed by Raman spectroscopy and neutron irradiation. American Mineralogist, 95: 1192-1201.

McDonough, W.F., Sun, S.S., 1995. The composition of the Earth. Chemical Geology, 120, 223-253.

Marshall, B., Vokes, F.M., Larocque, A.C.L., 2000. Regional metamorphic remobilization: upgrading and formation of ore deposits. In Spry, P.G., Marshall, B., Vokes, F.M. (Eds.), Metamorphosed and Metamorphogenic Ore Deposits. Reviews in Economic Geology, 11, 19-38.

Mathieu, L., 2019. Origin of the Vanadiferous Serpentine-Magnetite Rocks of the Mt. Sorcerer Area, Lac Doré Layered Intrusion, Chibougamau, Québec. Geosciences, 9, 110.

McDonough, W.F., Sun, S.S., 1995. The composition of the Earth. Chemical Geology, 67(5), 1050-1056.

McQueen, K.G. and Cross, A.J., 1998. Magnetite as a geochemical sampling medium: application to skarn deposits. The State of Regolith, Geological Society of Australia Special Publication 20, 194-199.

Miller, C.F., Meshter McDowell, S., Mapes, R.W., 2003. Hot and cold granites? Implications of zircon saturation temperatures and preservation of inheritance. Geology, 31(6), 529-532.

Montel, J., Foret, S., Veschambre, M., Nicollet, C., Provost, A., 1996. Electron microprobe dating of monazite. Chemical Geology, 131, 37-53.

Morgan, J.W., Stein, H.J., Hannah, J.L., Markey, R.J., Wiszniewska, J., 2000. Re-Os study of Fe-Ti-V oxide and Fe-Cu-Ni sulphide deposits, Suwalki Anorthosite Massif, Northeast Poland. Mineralium Deposita, 5: 391-401.

[a]Motuza, G., 2004. Viršutinės plutos sandarac ir raida. Lietuvos Žemės gelmių raid air ištekliai. 11-17.

[b]Motuza, G., 2004. Evolution of the structure and composition of the Earth Crust and crystalline basement. In: Evolution of Earth Crust and its Resources inLithuania (V. Baltrunas, ed.), Publ. J. Lithosphere, 11-40.

Motuza, G., 2005. Structure and formation of the crystalline crust in Lithuania. Mineralogical Society of Poland, Special paper, 26, 69-79.

Motuza, G., Čečys, A., Kotov, A., Salinkova, E.B., 2006. The Žemaičių Naumiestis granitoids: new evidences fro Mesoproterozoic magmatism in western Lithuania. GFF, 128: 243-254.

Motuza, G., Gailius, R., Gasiūnienė, V., and others, 1976. Varėnos geležies rūdos plotas Lietuvos Pietuose. BTSR geologijos ir rūdinių naudingųjų iškasenų paieškų klausimai. Minskas, 27-35 (in Russian).

Motuza, G. Kirkliauskaite, V., 2016. Ultramafic Varėna Suite in the crystalline basement of the southern Lithuania – implications for the origin. Baltica, 29(2), 93-106.

Motuza, G., Motuza, V., Salnikova, E., Kotov. A., 2008. Extensive charnokitic-granitic magmatism in the crystalline crust of West Lithuania. Geologija, 1(61), 1-16.

Мотуза, Г.Б., Пап, А.М., Пашкявичене, Л.Т., Пискун, Л.В., Шкуратов, В.И., 1986. Протерозой. Геологи-ческая карта СССР. Лист N-(34), (35), Вильнюс. Ленинград, 14–25

Motuza, G., Skripkina, T., 1981. Vario-molibdeno rūnigumo charakteristika Marcinkonių granitiniame masyve (pietų Lietuva). Lietuvos TSR geologijos pasiekimai ir tyrimų uždaviniai. 82-83 (In Russian).

Murakami, T., Chakoumakos, B.C., Ewing, R.C., Lumpkin, G.R., Weber, W.J., 1991. Alpha-decay event damage in zircon. American Mineralogist, 76: 1510-1532.

Nakamura, N., 1974. Determination of REE, Ba, Fe, Mg, Na and K in Carbonaceous and Ordinary Chondrites. Geochimica et Cosmoshimica Acta, 38, 757-775.

Nasdala, L., Hanchar, J.M., Rhede, D., Kennedy, A.K., Váczi, T., 2009. Retention of uranium in complexly altered zircon: An example from Bancroft, Ontario. Chemical geology, 3-4: 290-300.

Nasdala, L., Pidgeon, R.T., Wolf, D., Irmer, G., 1998. Metamictisation and U-Pb isotopic discordance in single zircons: a combined Raman microprobe and SHRIMP ion probe study. Mineralogy and Petrology, 62: 1-27.

Nasdala, L., Wenzel, M., Vavra, G., Irmer, G., Wenzel, T and Kober, B., 2001. Metamictisation of natural zircon: accumulation versus thermal annealing of radioactivity-induced damage. Contributions to Mineralogy and Petrolgy, 141, 125-144.

Pearce, J.A., 1983. Role of the sub-continental lithosphere in magma genesis at active continental margins. *In* C.J. Hawkesworth and M.J. Norry, (eds.): Continental Basalts and Mantle Xenoliths. Shiva Natwich, 230-249.

Pearce, J., Harris, N., Tindle, A.G., 1984. Trace Element Discrimination Diagrams for Tectonic Interpretation of Granitic Rocks. Journal of Petrology, 25, 956-983.

Peck, W.H. and Smith, M.S., 2005. Cordierite-gedrite rocks from the central metasedimentary belt boundary thrust zone (Greenville Province, Ontario): Mesoproterozoic metavolcanics rocks with the affinities to the composite arc belt. Canadian Journal of Earth Science 42: 1815-1828.

Powell, R., Holland, T.J.B. & Worley, B., 1998: Calculating phase diagrams involving solid solutions via non-linear equations with examples using THERMOCALC. Journal of Metamorphic Geology 6, 173-204.

Pyle, J.M. and Spear, F.S., 1999. Yttrium zoning in garnet: coupling of major and accessory phases during metamorphic reactions. Geological Material Research, 1, 1-49.

Ray, G.E., Webster, I.C.L., 2007. Geology and chemistry of the low-Ti magnetite-bearing Heff Cu-Au Skarn and its associated plutonic rocks, Heffley Lake, south-central British Columbia. Exploration and Mining

Geology, 16 (3-4), 159-167. Canadian Institute of Mining, Metallurgy and Petroleum.

Rubatto, D., 2017. Zircon: The Metamorphic Mineral. *In* Petrochronology: Methods and Applications. *Eds.:* Swainson, I. Reviews in Mineralogy and Geochemistry 83: 261-289.

Ruszkowski, M., Wiszniewska, J., Krzemińska, E., Bagiński, B., 2018. Geochronological calendar of A-type granites from NE Poland. Geophysical Research Abstract in EGU General Assembly 2018. Vol. 20, EGU2018-18648.

Sack, R.O., Ghioso, M.S., 1991. Chromian spinel as Petrogenetic indicators: thermodynamics and petrological indications. American Minerologist 76, 827-847.

Salin, E., Sundblad, K., Woodard, J., O'Brien, H., 2019. The extension of the Transscandinavian Igneous Belt into the Baltic Sea region. Precambrian Research, 328, 287-308.

Schneiderma, J.S. and Tracy, R.J., 1991. Petrology of orthoamphibole-cordierite gneisses from the Orijärvi area, southwest Finlad. American Mineralogist, 76, 942-955.

Šiliauskas, L., Skridlaitė, G., Whitehouse, M., Soesoo, A., 2018. A ca. 1.89 Ga magmatic complex in eastern Lithuania: a link connecting with the domains in Estonia and the Bergslagen terrane in Sweden. Geophysical Research Abstract in EGU General Assembly 2018. Vol 20, EGU2018-3050.

Silver, L.T., Deutsch, S., 1963. Uranium-lead isotopic variation in zircons: a case study. Journal of Geology, 7: 721-758.

Shiraki, R., Sakai, H., Endoh, M., Kishima, N., 1987. Experimental studies on rhyolite- and andesite-seawater interactions at 300 °C and 1000 bars. Geochemical Journal 21, 139-148.

[a]Skridlaite, G., 1993. Metasomatism in the Varena Iron Ore Zone, southern Lithuania. Ph. D. Thesis, Geological Institute and University of Vilnius (1993).

[b]Skridlaite, G., 1993. Geochemical peculiarities of metasomatic rocks from Varesnky Iron-ore zone on southern Lithuania. Zapiski Vserossiyskogo Mineralogicheskogo Obshchestva, 1, 81-88 [In Russian].

Skridlaitė, G., Baginski, B., Whitehouse, M., 2008. Significance of ~1.5 Ga zircon and monazite ages from charnockites in southern Lithuania and NE Poland. Gondwana Research, 14: 662-674.

Skridlaite, G., Bogdanova, S., Taran, L., Baginski, B., 2014. Recurrent high grade metamorphism recording a 300 Ma long Paleoproterozoic crustal

evolution in the western part of the East European Craton. Gondwana Research, 25, 649-667.

Skridlaite, G., Motuza, G., 2001. Precambrian domains in Lithuania: evidence of the terrane tectonics. Tectonophysics, 339(1-2), 113-133.

Skridlaite, G., Whitehouse, M., Bogdanova, S., Taran, L., 2011. The 1.86-1.84 Ga magmatism in the Western East European Craton (Lithuania): implications for a convergent continental margin. Int. Goldshimdt Conference, Prague Goldshimdt Cnference Abstract 75(3), 1890.

Skridlaitė, G., Whitehouse, M., Rimša, A., 2007. Evidence for a pulse of 1.45 Ga anorthosite-mangerite-charnokite-granite (AMCG) plutonism in Lithuania: implications for the Mezoproterozoic evolution of the East European Craton. Terra Nova, 19: 294-301.

Skridlaitė, G., Wiszniewska, J., Duchesne, J-C., 2003. Ferro-potassic A-type granites and related rocks in NE Poland and S Lithuania: west of the East European Craton. Precambrian research, 124: 305-326.

Smith, I.E.M., Worthington, T.J., Price, R.C., Gamble, J.A., 1997. Primitive magmas in arc-type volcanic associations: examples from the southwest Pacific. The Canadian Mineralogist, 35, 257-273.

Spear, F.S., 1980. The gedrite-anthophyllite solvus and the composition limits of orthoamphibole from the Post Pond Volcanics, Vermont. American Mineralogist, 65, 1103-1118.

Sun, S.S., McDonough, W.F., 1989. Chemical and isotopic systematics of oceanic basalts: implications for mantle compositions and processes. Geological Society, London, Special Publications, 42, 313-345.

Sundblad, K., Msfeld, J., Motuza, G., Ahl, M., Claesson, S., 1994. Geology, geochemistry and age of a CuMo-bearing granite at Kabeliai, southern Lithuania. Mineralogy and Petrology, 50: 43-57.

Stacey, J.S. and Kramers, J.D., 1975: Approximation of terrestrial lead isotope evolution by a two-stage model. Earth Planet Science Letters 26, 207–221.

Stripeika, A., 1975. Vakarų Lietuvos vulkanogeninės uolienos ir jų ryšys su Baltijos sineklizės grimzdimo etapais. *In* Pabaltijo kristalinio pamato ir nusėdinės dangos geologija, Ryga, Zinante. 41-57.

Tracy, R.J. and Frost, R.R., 1991. Phase equilibria and thermobarometry of calcareous, ultramafic and mafic rocks, and iron formations. Pp. 207-90 in: *Contact Metamorphism* (D.M. Kerrich, ed.). Reviews in Mineralogy, 26. Mineralogical Society of America, Washington, D.C.

Utsunomiya, S., Palenik, C.S., Valley, J.W., Cavosie, A.J., Wilde, S.A., Ewing, R.C., 2004. Nanoscale occurrence of Pb in an Archean zircon. Geochmimica et Cosmochimica Acta, 68: 4679-4686.

Vasiljievas, V., Gailius, R., Motuza, G., 1976. Pietinio Pabaltijo kristalinio pamato uolienos ir jų stratigrafinis suskirstymas. Pabaltijo stratigrafijos duomenys. 10-11 (In Russian).

Vokes, F.M., 2000. Ores and metamorphism: introduction and historical perspective. In Spry, P.G., Marshall, B., Vokes, F.M. (Eds.), Metamorphosed and Metamorphogenic Ore Deposits. Reviews in Economic Geology, 11, 1-18.

Wang, X., Chen, J., Ren, M., 2016. Hydrothermal zircon geochronology: Age constrain on Nanling Range tungsten mineralization (Southeast China). Ore Geology Reviews, 74: 63-75.

Watson, E.B., Harrison, T.M., 1983. Zircon saturation revised: Temperature and composition effects in a variety of crustal magma types. Earth Planetary Science Letters, 64, 295-304.

White, R.W., Powell, R., Holland, T.J.B., 2007. Progress relating to calculation of partial melting equilibria for metapelites. Journal of Metamorphic Geology 25, 511-527.

Whitehouse, M.J. and Kamber, B.S., 2005: Assigning dates to thin gneissic veins in high-grade metamorphic terranes: a cautionary tale from Akilia, Southwest Greenland. Journal of Petrology 46, 291–318.

Whitehouse, M.J., Kamber, B.S. and Moorbath, S., 1999: Age significance of U–Th–Pb zircon data from early Archaean rocks of west Greenland – a reassessment based on combined ion-microprobe and imaging studies. Chemical Geology 160, 201–224.

Wiedenbeck, M., Allé, P., Corfu, F., Griffin, W.L., Meier, M., Oberli, F., Quadt, A.V., Roddick, J.C. and Spiegel, W., 1995: Three natural zircon standards for U–Th–Pb, Lu–Hf, trace element and REE analyses. Geostandards Newsletter 19, 1–23.

Williams, M.L., Jercinovic, M.J., Hetherington, C.J., 2007. Microprobe monazite geochronology: understanding geologic processes by integrating composition and chronology. The Annual Review of Earth and Planetary Sciences, 35, 137-175.

Wiszniewska, J., Krzeminska, E., Dörr, W., 2007. Evidence of arc-related Svecofenian magmatic activity in the southwestern margin of the East European Craton in Poland. Gondwana Research, 12(3), 268-278.

Wiszniewska, J., Krzeminska, E., Rosowiecka, O., Petecki, Z., Ruszkowski, M., Salwa, S., 2018. New results of polymetallic, PGE and REE mineralization research in the Suwalki anorthosite massif (NE Poland). Biuletyn Panstwowego Instytutu Geologicznego, 472, 271-284.

Wiszniewska, J., Petecki, Z., Rosowiecka, O., Krseminska, E., Ruszkowski, M., Grabarczyk, A., 2019. The Fe-Ti-V ore deposits – new insight from the geophysical-geological modelling of the Suwalki Anorthosite Massif (NE Poland). Geophysical Research Abstracy, EGU General Assembly, EGU2019-5086, Vol. 21.

Xu, X.S., Zhang, M., Zhu, K.Y., Chen, X.M., He, Z.Y., 2012. Reverse age zonation of zircon formed by metamictisation and hydrothermal fluid leaching. Lithos 150: 256-267.

Yang, X.-M., 2017. Estimation of crystallization pressure of granite intrusions. Lithos, 286-287, 324-329.

Yliniemi, T., Tiira, T., Luosto, U., Komminaho, K., Geise, R., Motuza, G., Nasedkin, V., Jacyna, J., Seckus, R., Grad, M., Czuba, W., Janik, T., Guterch, A., Lund, C-E., Doody, J.J., EUROBRIDGE'95 seismic working group, 2001. EUROBRIDGE'95: deep seismic profilin within the East European Craton. Tectonophysics, 339, 153-175.

Zhu, X.K. and O'Nions, R.K., 1999. Monazite chemical composition; some implications for monazite geochronology. Contributions to Mineralogy and Petrology, 137, 351-363.

APPENDIX

1. Tables

Table A1. Representative garnet analyses from the studied samples. Fe^{3+}apfu was calculated assuming full occupancies

	Core		Rim		Homogeneous garnet		Porphyroblast (homogeneous)	
ID	521.8-core-9	521.8-core-5	521.8-rim-16	521.8-rim-2	521.8-matrix-6	521.8-matrix-7	540-2	540-12
SiO_2	37.46	37.17	36.40	37.05	36.78	36.89	36.66	36.30
TiO_2	0.00	0.00	0.00	0.00	0.00	0.00	0.00	0.00
Al_2O_3	20.50	20.53	20.54	20.60	20.39	20.46	20.32	20.11
FeO	33.15	33.86	35.60	35.38	35.32	35.14	38.81	39.30
MnO	1.75	1.78	1.52	1.56	1.06	1.03	0.41	0.42
MgO	3.26	3.39	3.53	3.38	4.13	4.08	3.14	3.00
CaO	3.33	3.21	1.84	1.96	2.17	2.05	1.39	1.05
Total	99.44	99.94	99.43	99.94	99.85	99.65	100.72	100.18
				12 oxygen per formula unit				
Si	3.019	2.983	2.944	2.983	2.950	2.965	2.945	2.939
Ti	0.000	0.000	0.000	0.000	0.000	0.000	0.000	0.000
Al	1.947	1.942	1.958	1.954	1.928	1.938	1.924	1.919
Fe^{3+}	0.014	0.092	0.153	0.080	0.171	0.132	0.186	0.204
Fe^{2+}	2.221	2.180	2.255	2.302	2.198	2.229	2.422	2.457
Mn	0.119	0.121	0.104	0.106	0.072	0.070	0.028	0.029
Mg	0.392	0.406	0.426	0.406	0.494	0.489	0.376	0.362
Ca	0.288	0.276	0.159	0.169	0.187	0.177	0.120	0.091
Total	8.000	8.000	8.000	8.000	8.000	8.000	8.000	8.000
$Mg^{\#}$	0.150	0.157	0.159	0.150	0.183	0.180	0.134	0.128
X_{alm}	0.735	0.731	0.766	0.772	0.745	0.752	0.822	0.836
X_{sps}	0.040	0.041	0.035	0.036	0.024	0.024	0.009	0.010
X_{prp}	0.130	0.136	0.145	0.136	0.167	0.165	0.128	0.123
X_{Grs}	0.095	0.088	0.050	0.054	0.058	0.056	0.037	0.028
X_{and}	0.001	0.004	0.004	0.002	0.005	0.004	0.004	0.003

Table A2 Representative biotite analyses from the studied samples. The water content (OH) calculations are after Tindle and Webb (1990)

	Porphyroblast			Matrix	
ID	Bt-512-14	Bt-521.8-6	Bt-540-13	Bt-521.8-6	Bt-540-1
SiO2	36.51	36.78	34.58	36.48	34.32
TiO2	1.08	1.32	1.38	1.55	1.75
Al2O3	17.19	17.29	18.21	16.03	19.17
FeO	20.83	20.44	23.98	21.64	23.12
MnO	0.00	0.00	0.00	0.00	0.00
MgO	11.54	11.45	8.62	11.55	8.46
CaO	0.00	0.00	0.00	0.00	0.00
Na2O	0.30	0.37	0.33	0.26	0.31
K2O	8.47	8.27	8.94	8.98	8.78
Cl	0.17	0.14	0.19	0.00	0.17
H2O*	3.92	3.94	3.83	3.95	3.85
Total	99.97	99.97	100.02	100.44	99.90
			22 oxygen per formula unit		
Si	5.526	5.546	5.344	5.538	5.280
Al^{iv}	2.474	2.454	2.656	2.462	2.720
Al^{vi}	0.593	0.618	0.661	0.406	0.755
Ti	0.123	0.150	0.160	0.177	0.202
Fe	2.637	2.577	3.099	2.747	2.974
Mn	0.000	0.000	0.000	0.000	0.000
Mg	2.604	2.574	1.986	2.614	1.940
Na	0.088	0.108	0.099	0.077	0.092
K	1.635	1.590	1.762	1.739	1.723
OH	3.956	3.964	3.950	4.000	3.956
Cl	0.044	0.036	0.050	0.000	0.044
Fe/Fe+Mg	0.503	0.500	0.609	0.512	0.605

Table A3 Representative analyses of amphiboles from this study.

ID	512-Ged-13	512-Ged-16	521.8-Ged2	521.8-Ged-11	521.8-Ath-1	521.8-Ath-2	512-Ath-5	512-Ath-7
SiO2	45.28	45.28	43.15	45.09	50.35	52.55	50.19	50.27
TiO2	0.00	0.00	0.00	0.00	0.00	0.00	0.00	0.00
Al2O3	14.18	14.18	16.96	14.50	4.56	2.61	1.95	1.64
FeO	24.46	24.46	25.46	25.40	26.20	26.05	29.24	29.00
MnO	0.75	0.75	0.30	0.42	0.25	0.22	0.41	0.50
MgO	10.78	10.78	9.69	10.41	14.82	15.99	15.35	15.40
CaO	0.33	0.33	0.44	0.38	0.21	0.16	0.34	0.33
Na2O	1.35	1.35	1.58	1.34	0.24	0.26	0.00	0.00
K2O	0.00	0.00	0.00	0.00	0.00	0.00	0.00	0.00
Total	97.13	97.13	97.58	97.54	96.63	97.84	97.48	97.14
				23 oxygen per formula unit				
Si	6.743	6.743	6.433	6.706	7.540	7.750	7.488	7.526
Al^{iv}	1.257	1.257	1.567	1.294	0.460	0.250	0.343	0.289
Al^{vi}	1.231	1.231	1.413	1.248	0.345	0.204	0.000	0.000
Ti	0.000	0.000	0.000	0.000	0.000	0.000	0.000	0.000
Fe^{3+}	0.000	0.000	0.000	0.000	0.045	0.000	0.680	0.658
Fe^{2+}	3.046	3.046	3.174	3.159	3.236	3.213	2.968	2.973
Mn	0.095	0.095	0.038	0.053	0.032	0.027	0.052	0.063
Mg	2.393	2.393	2.154	2.308	3.309	3.516	3.414	3.437
Ca	0.053	0.053	0.070	0.061	0.034	0.025	0.000	0.000
Na	0.390	0.390	0.457	0.386	0.070	0.074	0.054	0.053
K	0.000	0.000	0.000	0.000	0.000	0.000	0.000	0.000
OH	2.000	2.000	2.000	2.000	2.000	2.000	2.000	2.000
Total	17.208	17.208	17.305	17.216	17.070	17.060	17.000	17.000
(Ca+Na) (B)	0.259	0.259	0.251	0.256	0.038	0.040	0.054	0.053
Na (B)	0.206	0.206	0.181	0.195	0.005	0.014	0.000	0.000
(Na+K) (A)	0.184	0.184	0.276	0.191	0.065	0.060	0.000	0.000
Mg#	0.440	0.440	0.404	0.422	0.506	0.522	0.535	0.536

Table A4 Representative plagioclase analyses from the Lz13 felsic volcanic rocks

ID	512-Pl-5	512-Pl-10	521.8-Pl-10	521.8-Pl-8	521.8-Pl-1	540-Pl-38	540-Pl-39
SiO2	48.10	67.63	59.73	59.02	57.16	58.43	60.31
TiO2	0.00	0.00	0.00	0.00	0.00	0.00	0.00
Al2O3	33.80	20.00	25.75	26.23	26.88	25.79	24.69
FeO	0.00	0.39	0.16	0.00	0.20	0.00	0.00
MnO	0.00	0.00	0.00	0.00	0.00	0.00	0.00
MgO	0.00	0.00	0.00	0.00	0.00	0.00	0.00
CaO	16.76	1.43	7.42	8.08	9.14	7.07	6.55
Na2O	1.48	9.71	7.60	7.54	6.82	8.00	8.34
K2O	0.00	0.32	0.15	0.00	0.00	0.00	0.00
sum	100.14	99.16	100.81	100.87	100.20	99.29	99.89
			8 oxygen per formula unit				
Si	2.194	2.971	2.647	2.618	2.563	2.629	2.690
Al	1.818	1.036	1.345	1.371	1.421	1.368	1.298
Ti	0.000	0.000	0.000	0.000	0.000	0.000	0.000
Fe	0.000	0.014	0.006	0.000	0.007	0.000	0.000
Mn	0.000	0.000	0.000	0.000	0.000	0.000	0.000
Mg	0.000	0.000	0.000	0.000	0.000	0.000	0.000
Ca	0.819	0.067	0.352	0.384	0.439	0.341	0.313
Na	0.131	0.827	0.653	0.648	0.593	0.698	0.721
K	0.000	0.018	0.008	0.000	0.000	0.000	0.000
Total	4.962	4.934	5.011	5.021	5.023	5.036	5.022
			Endmembers				
Or	0.000	1.965	0.836	0.000	0.000	0.000	0.000
Ab	13.778	90.657	64.412	62.807	57.452	67.188	69.735
An	86.222	7.378	34.751	37.193	42.548	32.812	30.265

Table A5. Representative cordierite analyses from the Lz13 felsic volcanic rocks

	Matrix						Crd hosting St	
ID	512-Crd-1	512-Crd-3	521.8-Crd-1	521.8-Crd-4	540-Crd-15	540-Crd-17	540-Crd-2	540-Crd-5
SiO2	48.31	48.49	48.88	48.95	48.11	47.95	49.52	49.97
TiO2	0.00	0.00	0.00	0.00	0.00	0.00	0.00	0.00
Al2O3	32.88	32.50	32.30	32.41	32.00	32.00	31.59	32.00
FeO	8.29	8.11	7.87	8.05	10.06	9.95	8.44	8.72
MnO	0.00	0.00	0.00	0.00	0.00	0.00	0.00	0.00
MgO	8.91	8.74	8.78	8.76	7.54	7.65	7.64	7.73
CaO	0.00	0.00	0.00	0.00	0.09	0.00	0.00	0.00
Na2O	0.13	0.11	0.12	0.00	0.16	0.19	0.31	0.24
K2O	0.00	0.00	0.00	0.00	0.00	0.00	0.00	0.00
Total	98.52	97.95	97.95	98.17	97.97	97.74	97.49	98.66
	18 oxygen per formula unit							
Si	4.967	4.985	5.038	5.045	4.955	4.939	5.154	5.201
Ti	0.000	0.000	0.000	0.000	0.000	0.000	0.000	0.000
Al	3.984	3.938	3.923	3.937	3.884	3.884	3.875	3.925
Fe	0.713	0.697	0.678	0.694	0.866	0.857	0.734	0.759
Mn	0.000	0.000	0.000	0.000	0.000	0.000	0.000	0.000
Mg	1.366	1.340	1.349	1.346	1.158	1.175	1.185	1.199
Ca	0.000	0.000	0.000	0.000	0.010	0.000	0.000	0.000
Na	0.026	0.022	0.024	0.000	0.032	0.038	0.063	0.048
K	0.000	0.000	0.000	0.000	0.000	0.000	0.000	0.000
Total	11.054	10.981	11.012	11.022	10.905	10.892	11.011	11.132
Mg#	0.657	0.658	0.665	0.660	0.572	0.578	0.617	0.612

Table A6. Representative staurolite analyses from the Lz13 felsic volcanic rocks

	St in Grt core		St in Grt rim		St in matrix and in Crd	
ID	540-St-12	540-St-13	540-St-1	540-St-2	540-St-5	540-St-8
SiO2	26.46	26.45	29.01	28.90	27.00	26.91
TiO2	0.31	0.51	0.40	0.41	0.25	0.26
Al2O3	53.87	53.69	52.87	53.21	52.51	53.45
FeO	15.01	15.19	11.67	11.77	14.61	14.30
MnO	0.00	0.00	0.00	0.00	0.00	0.00
MgO	1.44	1.57	1.40	1.36	1.31	1.25
CaO	0.00	0.00	0.00	0.00	0.00	0.00
Na2O	0.00	0.00	0.00	0.00	0.24	0.34
K2O	0.00	0.00	0.00	0.00	0.00	0.00
ZnO	0.93	0.86	2.81	2.95	2.24	2.25
Total	98.02	98.27	98.15	98.60	98.15	98.76
			23 oxygen per formula unit			
Si	3.711	3.704	4.019	3.991	3.804	3.762
Ti	0.033	0.054	0.042	0.043	0.026	0.027
Al	8.904	8.860	8.633	8.661	8.718	8.807
Fe	1.760	1.779	1.352	1.359	1.721	1.672
Mn	0.000	0.000	0.000	0.000	0.000	0.000
Mg	0.301	0.328	0.289	0.280	0.275	0.261
Ca	0.000	0.000	0.000	0.000	0.000	0.000
Na	0.000	0.000	0.000	0.000	0.066	0.092
K	0.000	0.000	0.000	0.000	0.000	0.000
Zn	0.096	0.089	0.287	0.301	0.233	0.232
Total	14.805	14.813	14.623	14.635	14.843	14.853
Mg#	0.146	0.156	0.176	0.171	0.138	0.135
X_{Fe}	0.816	0.810	0.701	0.701	0.772	0.772
X_{Mg}	0.140	0.149	0.150	0.144	0.123	0.120
X_{Zn}	0.045	0.040	0.149	0.155	0.105	0.107

Table A7. Representative analyses of magnetite from sample D8-1 in wt%.

D8-1	1	2	3	4	5	6	7	8	9	10
Mg	0,41	0,32	0,38	0,33	0,33	0,36	0,39	0,36	0,34	0,34
Al	0,24	0,19	0,17	0,14	0,14	0,18	0,25	0,28	0,18	0,24
Ti	0,25	0,22	0,23	0,27	0,25	0,23	0,25	0,25	0,20	0,23
V	0,09	0,14	0,12	0,10	0,09	0,09	0,11	0,00	0,00	0,09
Cr	0,00	0,00	0,00	0,00	0,00	0,00	0,00	0,00	0,00	0,00
Mn	0,00	0,00	0,00	0,00	0,00	0,00	0,00	0,00	0,00	0,00
Cu	0,00	0,00	0,00	0,00	0,00	0,00	0,00	0,00	0,00	0,00
Zn	0,05	0,00	0,00	0,00	0,00	0,00	0,00	0,00	0,00	0,00
Si	0,00	0,00	0,00	0,03	0,00	0,00	0,00	0,00	0,00	0,00
Fe	70,93	71,75	71,52	71,48	71,96	71,44	70,72	71,31	71,56	71,41
Ca	0,00	0,00	0,00	0,00	0,00	0,00	0,00	0,00	0,00	0,00
O	28,94	28,98	28,94	28,73	28,86	28,81	28,85	28,90	28,64	28,95
Total	100,91	101,59	101,36	101,08	101,63	101,09	100,56	101,10	100,93	101,27

Table A8. Representative analyses of magnetite from sample D8-2 in wt%.

D8-2	2	3	4	5	11	12	13	14	15	16	17
Mg	0,00	0,00	0,15	0,17	0,00	0,00	0,00	0,25	0,25	0,25	0,24
Al	0,00	0,00	0,06	0,06	0,00	0,00	0,00	0,06	0,07	0,08	0,07
Ti	0,00	0,00	0,21	0,19	0,00	0,00	0,00	0,23	0,24	0,22	0,22
V	0,00	0,00	0,00	0,00	0,00	0,00	0,00	0,00	0,00	0,00	0,00
Mn	0,00	0,00	0,00	0,00	0,00	0,00	0,00	0,00	0,00	0,00	0,00
Cu	0,00	0,00	0,00	0,00	0,00	0,00	0,00	0,00	0,00	0,00	0,00
Zn	0,00	0,00	0,00	0,00	0,75	1,08	0,94	0,00	0,00	0,00	0,00
Si	0,12	0,09	0,00	0,03	0,00	0,12	0,03	0,00	0,00	0,00	0,00
Fe	68,62	69,31	71,01	71,19	68,47	67,84	68,59	71,10	71,19	70,98	71,72
Ca	0,00	0,00	0,00	0,00	0,00	0,00	0,00	0,00	0,00	0,00	0,00
O	26,30	26,53	27,74	27,83	26,37	26,35	26,51	28,00	28,06	28,00	28,20
Total	95,05	95,93	99,18	99,46	95,59	95,39	96,08	99,65	99,81	99,54	100,44

Table A9. Representative analyses of magnetite from sample D8-7 in wt%.

D8-7	70 /1	71 /1	76 / 1	77 /1	80 / 1	99 / 1	100 / 1	102 / 1	103 / 1	104 / 1	105 / 1
Mg	0,35	0,47	0,19	0,19	0,19	0,24	0,24	0,26	0,26	0,23	0,24
Al	0,00	0,00	0,05	0,05	0,04	0,00	0,00	0,00	0,00	0,04	0,03
Ti	0,00	0,00	0,18	0,18	0,20	0,26	0,25	0,25	0,26	0,25	0,22
V	0,00	0,00	0,00	0,00	0,00	0,00	0,00	0,00	0,00	0,00	0,00
Cr	0,00	0,00	0,00	0,00	0,00	0,00	0,00	0,00	0,00	0,00	0,00
Mn	0,00	0,00	0,00	0,00	0,00	0,00	0,00	0,10	0,00	0,00	0,00
Cu	0,00	0,80	0,00	0,00	0,00	0,00	0,00	0,00	0,00	0,00	0,00
Zn	0,00	0,00	0,00	0,00	0,00	0,00	0,00	0,00	0,00	0,00	0,00
Si	0,32	0,20	0,00	0,00	0,00	0,05	0,00	0,00	0,00	0,00	0,00
Fe	70,80	68,24	71,89	70,99	71,97	70,70	70,67	70,89	70,66	71,47	71,08
Ca	0,04	0,04	0,00	0,00	0,00	0,00	0,08	0,00	0,00	0,00	0,00
O	28,06	27,46	28,02	27,68	28,04	27,65	27,69	27,83	27,70	28,06	27,88
Total	99,57	97,21	100,32	99,09	100,43	98,90	98,92	99,35	98,88	100,05	99,45

Table A10. Representative analyses of magnetite from sample 982-10 and 982-9 in wt%.

Sample	982-10						982-9				
ID	137/1.	140/1.	148/1.	151/1.	8/1.	15/1.	20/1.	24/1.	30/1.	56/1.	68/1.
SiO_2	0,00	0,05	0,00	0,00	0,00	0,57	0,00	0,00	0,00	0,00	0,00
TiO_2	0,09	0,09	0,07	0,07	0,00	0,00	0,12	0,00	0,00	0,11	0,00
Al_2O_3	0,36	0,49	0,46	0,41	0,34	0,00	0,10	0,09	0,05	0,14	0,03
Cr_2O_3	0,00	0,00	0,00	0,00	0,03	0,00	0,00	0,00	0,00	0,00	0,02
V_2O_3	0,10	0,11	0,00	0,00	0,00	0,00	0,00	0,00	0,06	0,00	0,00
FeO	93,02	92,19	92,52	92,59	92,59	92,79	92,68	93,55	93,24	93,15	92,81
MnO	0,00	0,00	0,00	0,11	0,08	0,14	0,17	0,19	0,15	0,06	0,12
MgO	0,50	0,62	0,56	0,63	0,46	0,08	0,21	0,18	0,24	0,34	0,10
CaO	0,00	0,00	0,00	0,00	0,00	0,00	0,00	0,00	0,00	0,00	0,00
ZnO	0,00	0,00	0,00	0,00	0,00	0,00	0,00	0,00	0,18	0,00	0,00
NiO	0,19	0,00	0,17	0,00	0,12	0,00	0,08	0,07	0,00	0,00	0,00
SnO_2	0,21	0,17	0,16	0,15	0,22	0,17	0,20	0,20	0,17	0,22	0,22
Total	94,46	93,73	93,93	93,95	93,86	93,75	93,55	94,27	94,10	94,01	93,29

PAPERS

Papers based on the data obtained during the study period of 2016-2019 are listed below. They are referred in the text by their Roman numerals:

Paper **I**: Prusinskiene, S., **Siliauskas, L**., Skridlaite, G. 2017. Varieties and chemical composition of magnetite in the Varena Iron Ore Deposit. Chemija, 28(1), 39-57.

Paper **II**: **Siliauskas, L**., Skridlaite, G., Baginski, B., Whitehouse, M., Prusinskiene, S. 2018. What the ca. 1.83 Ga gedrite-cordierite schists in the crystalline basement of Lithuania tell us about the late Paleoproterozoic accretion of the East European Craton. GFF, 140(4), 332-344.

Paper **III**: Skridlaite, G., **Siliauskas, L**., Prusinskiene, S., Baginski, B. 2019. Petrography and mineral chemistry of the Varena Iron Ore deposit, southeastern Lithuania: implications for the evolution of carbonate and silicate rocks and ore mineralization. Baltica, 32(1), 107-126.

Paper **IV**: **Siliauskas, L**., Skridlaite, G., Whitehouse, M. 2019. Microtextures in the radiation-damaged zircons and their dating: a case study of the ca. 1.50 Ga granitoid veins crosscutting skarn bodies in south-eastern Lithuania. Geological Quarterly. SUBMITED.

NOTES

Vilniaus universiteto leidykla
Saulėtekio al. 9, LT-10222 Vilnius
El. p. info@leidykla.vu.lt,
www.leidykla.vu.lt
Tiražas 9 egz.